TECHNISCHE
UNIVERSITÄT
WIEN

DISSERTATION

Optimal Wave Fields in Complex Scattering Environments

Ausgeführt zum Zwecke der Erlangung des akademischen Grades eines
Doktors der technischen Wissenschaften

unter der Leitung von
Univ.-Prof. Dipl.-Ing. Dr. techn. Stefan Rotter
Institut für Theoretische Physik, E136

eingereicht an der
Technischen Universität Wien
Fakultät für Physik

von
Dipl.-Ing. Matthias Kühmayer
Matr.-Nr. 0825988
[redacted]

Ort, Datum

Unterschrift

In loving memory of Sonja.

Erklärung zur Verfassung der Arbeit

Dipl.-Ing. Matthias Kühmayer
Klein-Mariazell 78, 2571 Altenmarkt

Hiermit erkläre ich, dass ich diese Arbeit selbständig verfasst habe, dass ich die verwendeten Quellen und Hilfsmittel vollständig angegeben habe und, dass ich die Stellen der Arbeit - einschließlich Tabellen, Karten und Abbildungen -, die anderen Werken oder dem Internet im Wortlaut oder dem Sinn nach entnommen sind, auf jeden Fall unter Angabe der Quelle als Entlehnung kenntlich gemacht habe.

Ort, Datum

Unterschrift Dipl.-Ing. Matthias Kühmayer

Abstract in German - Deutsche Kurzfassung

Die Streuung von Wellen ist in der Natur allgegenwärtig und für Anwendungen oft nachteilig, da sie verhindert, dass eine Welle ihre Form und Ausbreitungsrichtung beibehält. Mit den rasanten technologischen Fortschritten des letzten Jahrzehnts und der Entwicklung so genannter räumlicher Lichtmodulatoren ist jedoch eine Vielzahl neuer Möglichkeiten zur Steuerung von Licht und damit ein ganz neues Forschungsgebiet entstanden. Die Möglichkeit, die einfallende Wellenfront in Phase und Amplitude präzise zu steuern und gleichzeitig die ausgehende gestreute Welle zu messen, hat die Bestimmung einer der zentralen Größen der Streutheorie ermöglicht: die Streumatrix.

In dieser Arbeit nutzen wir die in der experimentell zugänglichen Streumatrix gespeicherte Information, um optimale Wellenfronten für bestimmte Aufgaben zu erzeugen, die die typischerweise nachteiligen Effekte, die durch das Vorhandensein einer komplexen Streuumgebung verursacht werden, überwinden. Durch die Verallgemeinerung des bekannten Konzepts der *Eisenbud-Wigner-Smith-Zeitverzögerung*, das in der Kernstreutheorie entwickelt wurde, zeigen wir, dass ein entsprechender verallgemeinerter Wigner-Smith-Operator Wellenzustände liefert, die optimal für die Mikromanipulation geeignet sind. Genauer gesagt zeigen wir, dass die Verwendung verschiedener parametrischer Ableitungen der Streumatrix im verallgemeinerten Operator zu Wellenfronten führt, die eine wohldefinierte Kraft, ein Drehmoment oder einen radialen Druck auf ein Zielobjekt ausüben oder sogar eine wohldefinierte Menge an Intensität in ihm speichern. Das in dieser Arbeit vorgestellte Konzept basiert auf einem einfachen Eigenwertproblem und funktioniert für beliebig komplex geformte Ziele, die sogar tief in ein ungeordnetes Medium eingebettet sein können. Darüber hinaus stützt es sich ausschließlich auf die Kenntnis der in der Streumatrix kodierten Fernfeldinformationen und benötigt keine lokalen Informationen in der Umgebung des Zielobjekts. Zur Untermauerung unseres Konzepts führen wir außerdem Experimente in einem Mikrowellen-Wellenleiter durch, die unsere theoretischen Erkenntnisse bestätigen.

Durch Nutzung der in der Streumatrix gespeicherten Informationen zeigen wir außerdem, wie die Auswirkungen der Streuung überwunden werden können, indem wir Lichtzustände finden, die bei der Ausbreitung durch ein stark streuendes Medium das gleiche Ausgangsfeld (bis auf eine globale Amplitude und Phase) erzeugen wie bei der Ausbreitung durch Luft. Wir bezeichnen solche Zustände als streuungs-

invariante Moden und zeigen, dass – obwohl diese Zustände intuitiv sehr selten zu sein scheinen – eine ganze Menge von ihnen aus einem einfachen verallgemeinerten Eigenwertproblem gewonnen werden kann. Darüber hinaus ist das Konzept der streuungsinvarianten Moden nicht auf die Ausbreitung durch ein stark streuendes Medium und Luft beschränkt, sondern kann auf zwei beliebige Arten von Medien angewendet werden. Zusätzlich zu numerischen Simulationen untermauern wir das untersuchte Konzept auch mit experimentellen Messungen im optischen Bereich. Wir zeigen auch numerisch, dass diese streuungsinvarianten Moden einen gewissen Grad an Korrelation mit ballistischem Licht innerhalb ungeordneter Medien beibehalten und somit auch zur Verbesserung aktueller Bildgebungsverfahren verwendet werden können.

Für einige Anwendungen ist die Streuung nicht nachteilig, sondern sogar unerlässlich. Ein Beispiel dafür sind Strukturen, die sich die Absorption von Licht zunutze machen, wie etwa Solarzellen, bei denen das Hauptziel darin besteht, die Absorption zu maximieren, indem die Verweildauer des Lichts in der Struktur maximiert wird. Obwohl es eine spezifische Wellenfront mit einer maximalen Verweildauer in einem gegebenen Medium gibt, wurde auf dem Gebiet der stochastischen Random Walks gezeigt, dass die mittlere Zeit oder Weglänge von Trajektorien für isotrope Beleuchtung unabhängig von allen Random-Walk-Parametern ist, die den Diffusionsprozess charakterisieren, und nur von der Geometrie des Systems abhängt. Unter Verwendung des Konzepts der Eisenbud-Wigner-Smith-Zeitverzögerung wurde theoretisch gezeigt, dass diese bemerkenswerte Invarianzeigenschaft auch für Wellen im ballistischen und diffusiven sowie im lokalisierten Regime gilt. In dieser Arbeit gehen wir einen Schritt weiter und verifizieren diese Invarianzeigenschaft experimentell in allen Transportregimen der Unordnungsstreuung. Unter Verwendung eines Mikrowellen-Wellenleiters zeigen wir sowohl experimentell als auch numerisch, dass diese Invarianzeigenschaft sogar in Bandlückenstrukturen wie photonischen Kristallen gilt, in denen die interferierende Natur der Welle zu einer totalen Unterdrückung der Transmission in einem bestimmten Frequenzbereich führt. Außerdem untersuchen wir den Einfluss von Dissipation auf die mittlere Weglänge sowohl im schwachen als auch im starken Absorptionsregime.

Zuletzt führen wir ein lokalisiertes absorbierendes Element in einem stark streuenden System ein und zeigen, dass wir die in der Streumatrix gespeicherte Amplituden- und Phaseninformation nutzen können, um eine andere spezielle Art von optimalem Zustand zu erzeugen. Konkret zeigen wir, dass wir eine einfallende Wellenfront erzeugen können, die an einem lokalisierten Absorber in einem ungeordneten Medium perfekt absorbiert wird, indem wir die Form und die Frequenz der einfallenden Wellenfront sowie die Absorptionsstärke des verlustbehafteten Elements genau anpassen. Basierend auf dem Effekt der *kohärenten perfekten Absorption*, der in einfachen eindimensionalen Systemen eingeführt wurde, demonstrieren wir diesen Effekt numerisch in zweidimensionalen komplexen Streuumgebungen und realisieren ihn zum ersten Mal experimentell im Mikrowellenbereich.

TU Bibliothek WIEN Your knowledge hub
Die approbierte gedruckte Originalversion dieser Dissertation ist an der TU Wien Bibliothek verfügbar.
The approved original version of this doctoral thesis is available in print at TU Wien Bibliothek.

Abstract

The scattering of waves is ubiquitous in nature and often detrimental to applications, as it prevents a wave from maintaining its shape and direction of propagation. With the fast-paced technological advances in the last decade and the development of so-called spatial light modulators, a plethora of new possibilities to control light and thus a whole new area of research emerged. Being able to precisely control the incident wavefront in phase and amplitude while measuring the outgoing scattered wave has further enabled the acquisition of one of the central quantities in scattering theory: the scattering matrix.

In this thesis, we exploit the information stored in the experimentally accessible scattering matrix to create optimal wavefronts for specific tasks that overcome the typically detrimental effects induced by the presence of a complex scattering environment. Generalizing the well-known concept of *Eisenbud-Wigner-Smith time-delay*, which was developed in nuclear scattering theory, we demonstrate that a corresponding generalized Wigner-Smith operator yields wave states that are optimally suited for micromanipulation. More specifically, we show that using different parametric derivatives of the scattering matrix in the generalized operator leads to wavefronts that apply a well-defined force, torque or radial pressure to a target or even store a well-defined amount of intensity inside it. Most notably, the concept introduced in this thesis is based on a simple eigenvalue problem and works for arbitrarily complex-shaped targets which can even be buried deeply inside a disordered medium. Beyond that, it exclusively relies on the knowledge of the scattered far field information encoded in the scattering matrix and does not require any local information around the target. To substantiate our concept, we further conduct experiments in a microwave setup which confirm our theoretical findings.

Moreover, by utilizing the information stored in the scattering matrix, we demonstrate how to overcome the effects of scattering by finding states of light that create the same output field (up to a global amplitude and phase) when propagating through a strongly scattering medium as when propagating through air. We call such states scattering invariant modes and show that, while intuitively these states seem to be very rare, a whole set of them can be obtained from a simple generalized eigenvalue problem. Furthermore, the concept of scattering invariant modes is not restricted to the propagation through a strongly scattering medium and air, but can rather be applied to any two types of media. In addition to numerical simulations, we also corroborate the concept under study with experimental measurements in the optical domain. Moreover, we numerically show that these scattering invariant

modes maintain a certain degree of correlation with ballistic light inside scattering samples and can thus also be used to improve current imaging techniques.

For some applications, scattering is not only disadvantageous, but even essential. One example are structures which harness the absorption of light such as solar cells, in which the main goal is to maximize the absorption by maximizing the light's dwell time inside the structure. Even though there exists a specific wavefront with a maximum dwell time in a given medium, it was shown in the field of stochastic random walks that the mean time or path length of trajectories for isotropic illumination is independent of all random walk parameters that characterize the diffusion process and only depends on the system's geometry. By utilizing the concept of Eisenbud-Wigner-Smith time-delay, this striking invariance property has theoretically been shown to also hold for waves in the ballistic and diffusive as well as in the localized regime. In this thesis, we go one step further and experimentally verify this invariance property in all transport regimes of disorder scattering. Using a microwave waveguide setup, we show experimentally as well as numerically that this invariance property even applies in band-gap structures like photonic crystals in which the interfering nature of waves gives rise to a total suppression of transmission in a certain frequency range. Moreover, we investigate the effect of dissipation on the mean path length in the weak as well as in the strong absorption regime.

Ultimately, we introduce localized loss in a strongly scattering system and demonstrate that we can utilize the amplitude and phase information stored in the scattering matrix to create another special type of optimal state. Specifically, we show that we can create an incident wavefront which gets perfectly absorbed at a localized loss element inside a disordered medium by precisely adjusting the shape and the frequency of the incident wavefront as well as the absorption strength of the lossy element. Based on the effect of *coherent perfect absorption* which was introduced in simple one-dimensional systems, we numerically demonstrate this effect in two-dimensional complex scattering environments and experimentally realize it for the first time in the microwave regime.

Contents

Abstract in German - Deutsche Kurzfassung v

Abstract vii

Introduction 1

Part I Methods 5

1 Theoretical framework 7
- 1.1 Scattering formalism . . . 7
- 1.2 The Wigner-Smith time-delay operator . . . 10
- 1.3 Waveguide geometries and eigenmodes . . . 14

2 Numerical framework 23
- 2.1 Stationary scattering in 2D waveguides . . . 24
- 2.2 Stationary scattering in 3D waveguides . . . 33

Part II Applications and results 41

3 Optimal wave fields for micromanipulation 43
- 3.1 The generalized Wigner-Smith operator . . . 43
- 3.2 Optimal focusing compared to the field matrix method . . . 53
- 3.3 Incomplete access to the scattering matrix . . . 55
- 3.4 Conclusion . . . 58

4 Scattering invariant modes 61
- 4.1 Scattering invariance in a strongly scattering medium and air . . . 63
- 4.2 Scatterer avoidance in sparse scattering layers . . . 65
- 4.3 Application to improve scanning fluorescence imaging . . . 69
- 4.4 Conclusion . . . 72

5 Mean path length invariance beyond the diffusive regime 75
- 5.1 Disordered systems . . . 82
- 5.2 Photonic crystal . . . 84

5.3 Influence of absorption 86
5.4 Conclusion 93

6 Random anti-lasing through coherent perfect absorption **95**
6.1 Experimental realization in a microwave setup 98
6.2 Conclusion 107

Summary and outlook **109**

Appendix **113**
A Derivation of wave equations 113
B Relation between line source and excitation amplitudes 115
C Generalized Wigner-Smith operator for non-regular matrices 116
D Determination of mean free paths 118
E Time-averaged Poynting vector 119

Bibliography **121**

Acknowledgments **135**

List of Publications **137**

Curriculum vitae **139**

Introduction

The scattering of electromagnetic waves has a profound impact on contemporary society as it is an integral part of applications in our daily life and it typically leads to a deterioration in performance of the considered application. Over the past decades, the emerging field of wavefront shaping has enabled the precise modulation of the spatial shape of waves in order to overcome such detrimental effects which has proven to be a very fertile ground with realizations in many areas of wave scattering ranging from sound [1–3] and water waves [4, 5] to electromagnetic waves in the microwave [6–8] as well as in the optical domain [9–11]. The latter has been triggered by the advent of so-called spatial light modulators (SLMs) [12, 13] that are nowadays offering coherent control over up to a few million spatial degrees of freedoms, i.e., pixels [14–16]. In conjunction with digital image sensors that offer a correspondingly large number of degrees of freedom, this brings the complete characterization of a scattering process via the experimental measurement of the optical scattering matrix within reach. In fact, subparts like the optical monochromatic transmission matrix are already experimentally accessible [17–19], giving rise to impressive applications like focusing [20, 21] and transmission enhancement [22] behind a strongly scattering medium, image transmission through an opaque medium [23, 24], non-invasive imaging inside complex samples [25] as well as guidestar-assisted focusing into biological tissue [26]. In addition to targeting only the spatial degrees of freedom of light, SLMs have also enabled the control of light in the temporal domain allowing for spatio-temporal focusing behind strongly scattering layers [27–32] or to focus onto moving targets through [33] and within scattering samples [34].

With all these recent advances, also the implementation of all possible concepts derived from the scattering matrix is within reach today. One prominent example is the intriguing concept of *Eisenbud-Wigner-Smith time-delay* that was theoretically introduced in the realm of nuclear scattering [35–37]. Being exclusively based on the far-field information of a linear scattering process, this concept enables to assign specific delay times caused by the presence of a potential to the scattered waves, making it one of the few widely-known concepts of such kind [38, 39]. These delay times are encoded in the eigenvalues of the corresponding Wigner-Smith time-delay operator, where its eigenstates also feature a remarkable property that has been first recognized almost half a century later in the context of optical multi-mode fibers: Aiming for wave states whose output patterns are spectrally stable to first order, the so-called principal modes were introduced as eigenstates of the group-delay operator [40] which shares an intimate relation with the time-delay operator. A first experimental realization of these modes succeeded only very recently [41] and their properties have further been investigated in the strong mode coupling regime [42] as well as in the transition from weak to strong mode coupling [43]. Based on these insights, the time-delay concept was put forward and so-called *super-* and *anti-principal modes* were introduced which further enhance or drastically reduce the frequency stability of the output wavefronts [44]. The concept of time-delay also enabled to identify a special kind of wave states that features highly collimated beam-like wave function patterns during the entire propagation [45]. This defining feature caused the term particle-like states whose existence has already been verified experimentally in various types of systems [46, 47]. Apart from that, its connection to the so-called dwell time [48] has led to highly interesting applications in terms of optimal energy storage inside scattering media [49, 50], where its connection to the density of states [51, 52] was also exploited very recently [53, 54].

This thesis builds upon all these recent theoretical and experimental advances and aims to expand the horizon of the Wigner-Smith framework to design novel classes of wave states that perform at an optimal level. The thesis is divided into two parts, where the first part is split into Chapter 1 and 2. Chapter 1 provides a review of scattering theory giving a brief overview over the definition of the scattering matrix and its symmetries. Furthermore, we also introduce the concept of time-delay and its connection to group-delay and put it in context with the so-called dwell time and the density of states. We also review the complete and orthogonal set of transverse electric and transverse magnetic waveguide modes which will serve as the basis in which we represent the scattering matrices.

Despite the very exciting developments in wavefront shaping, experimental techniques typically do not allow access to the local behavior of waves inside scattering systems. Thus we proceed in Chapter 2 with the development of a flexible and accurate numerical tool for solving the time-harmonic Maxwell equations. Utilizing the framework of the finite element method, we first lay out the solution strategy for stationary scattering problems in two dimensions. More precisely, we solve the scalar Helmholtz equation in two-dimensional waveguide-like geometries and use the obtained solutions to calculate the scattering amplitudes to set up the entire scattering matrix. Since a scalar description only covers the transverse part of the electric field, we then continue with full-vectorial stationary scattering problems in three dimensions, where we solve the vector Helmholtz equation in order to capture all the physics contained in Maxwell's equations.

The second part of this thesis is devoted to the applications and results, where Chapter 3 presents a generalization of the concept of Wigner-Smith time-delay to a much broader class of novel operators. As the time-delay operator allows for the creation of wave states with a well-defined time-delay, the eigenstates of these *generalized Wigner-Smith* operators enable the application of well-defined forces, pressures or torques to a target as well as to optimally focus inside of it, where

TU Bibliothek WIEN Your knowledge hub
Die approbierte gedruckte Originalversion dieser Dissertation ist an der TU Wien Bibliothek verfügbar.
The approved original version of this doctoral thesis is available in print at TU Wien Bibliothek.

the target can even be embedded in a strongly scattering environment. We further show that the linear, radial or angular momentum transferred to the target and the stored intensity inside that target are encoded in the eigenvalues of the corresponding operator for which we derive analytical expressions. Furthermore, we present experimental measurements obtained in collaboration with the group of Ulrich Kuhl from the Université Côte d'Azur together with corresponding numerical simulations that corroborate the analytical findings [55]. In addition, we also investigate the presented concept in case where only a subpart of the scattering matrix is available [56].

In Chapter 4 we introduce another novel class of wave states that generalizes the principal modes' property of spectral stability to first order. In analogy to their output patterns which remain unchanged if the frequency of the incident wave is altered, we create waves whose output profiles do not "feel" the presence of a complex scattering environment and propagate through the latter as through a homogeneous material. To verify the existence of these so-called *scattering invariant modes*, we again perform numerical simulations which are supported by experimental measurements in an optical setup conducted in the group of Allard Mosk from Utrecht University [57]. We then continue with sparse scattering samples and show that these modes preferentially propagate through scatterer-free areas thus embodying one of the defining features of ballistic light. Since the latter is essential for imaging, we also present a first theoretical demonstration of their application to improve current imaging techniques in two as well as in three dimensions.

Going back to the roots and revisiting the concept of time-delay, we exploit its close connection to the density of states in Chapter 5. Although the concept of time-delay allows for the creation of optimal states that propagate fastest or slowest through a specific scattering system, we show that the average time-delay of waves in scattering media is invariant with respect to its scattering properties and only depends on its geometry. Specifically, we extend the results in Refs. [53, 54] and verify in collaboration with Matthieu Davy from the Université de Rennes 1 experimentally, that the so-called *mean path length invariance* holds in all transport regimes of disorder scattering [58]. Even more surprisingly, we also show that this invariance property further extends to periodic materials like photonic crystals that feature band gaps that fully suppress transmission in a certain frequency interval. To further substantiate the experimental findings, we perform numerical simulations of the experimentally used microwave cavity in the absence as well as in the presence of weak global dissipation to mimic the experimental setup as closely as possible. In addition, we theoretically investigate the influence of strong absorption on different time-delay operators, where we analytically encounter the convergence towards the most direct path in transmission and reflection of the corresponding eigenchannels.

Finally, Chapter 6 is devoted to the search for wave states that get optimally, i.e., perfectly absorbed at a localized loss element inside a disordered environment. By utilizing the effect of *coherent perfect absorption*, which was introduced in simple one-dimensional systems [59], we demonstrate that precisely adjusting the absorption strength as well as the frequency and the shape of the incident wave allows for perfect absorption, even in strongly scattering media. Together with the group of Ulrich Kuhl, we report the first experimental demonstration of this effect in a two-dimensional waveguide setup and underpin the obtained measurement results with numerical simulations [60]. To set the results apart from the effect of coherent enhancement of absorption [61], we utilize the numerically obtained solutions to investigate the full intensity and Poynting vector distributions inside the scattering system of the corresponding wave states.

Part I.

Methods

Chapter 1

Theoretical framework

1.1 Scattering formalism

A generic scattering system can be subdivided into two domains: an asymptotic region in which waves can freely propagate and a scattering region in which the actual scattering process takes place. A sketch of such a system is shown in Fig. 1.1. To ensure free propagation, the asymptotic regions feature a uniform refractive index distribution $n(\vec{r}) = \text{const.}$ with $\vec{r}$ being the position vector. The scattering region can be of arbitrary shape and can contain structured or disordered media with or without gain and loss. Mathematically, a disordered medium is described by a non-uniform refractive index $n(\vec{r})$ which becomes a complex quantity in the presence of gain and loss. If an incident wavefront impinges onto the scattering region, the inhomogeneity of the refractive index landscape causes a redistribution of the flux carried by the respective channels. After the scattering process, the wave is again leaving the scattering region into the asymptotic regions. Due to the absence of mode-mixing in these asymptotic regions, the incident and outgoing waves can be decomposed in a suitable and complete set of orthogonal basis states, where the corresponding expansion coefficients are contained in the vectors $\vec{u}$ and $\vec{v}$, respectively. The redistribution of the flux due to the scattering in the scattering region can then conveniently be described by the so-called scattering matrix S which allows for the book-keeping between in- and outgoing flux-carrying channels via

$$\vec{v} = S\vec{u}\,, \tag{1.1}$$

thus containing all the information about the scattering process. Moreover, the technological advances in the last decade have made it possible to experimentally measure the scattering matrix (or parts of it) in various types of systems, e.g., in microwave resonators [7], in disordered media illuminated with optical waves [17–19, 62], in optical multi-mode fibers [42, 63], for sound waves [64–66] or in elastic slabs [67].

In the absence of gain and loss, flux is conserved which manifests itself in a unitary scattering matrix, i.e.,

$$S^\dagger S = SS^\dagger = \mathbb{1}\,. \tag{1.2}$$

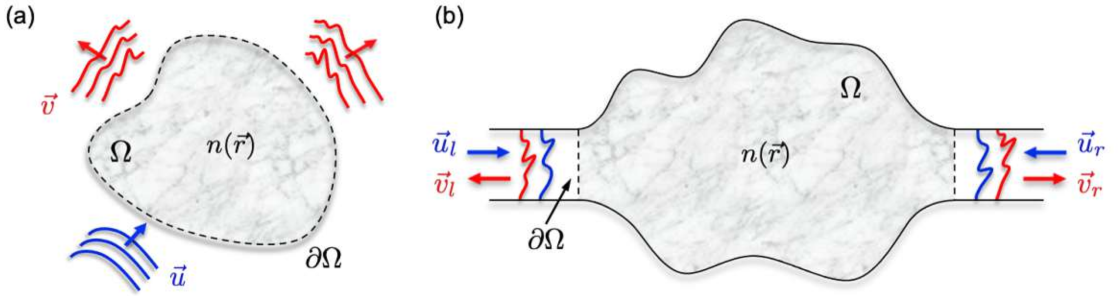

Figure 1.1: (a) Generic open scattering system featuring a non-uniform refractive index distribution $n(\vec{r})$ (structured gray area) and a uniform asymptotic region $n(\vec{r}) = \text{const.}$ (surrounding white area). An incident wavefront (blue) described by a coefficient vector $\vec{u}$ is impinging onto the scattering region Ω and gets scattered into outgoing waves (red) described by the coefficient vector $\vec{v}$. (b) Generic two-port scattering system, in which the non-uniform refractive index distribution is surrounded by hard walls (solid black lines) and connected to ports/leads on both sides. The latter serve as asymptotic regions through which the waves enter and exit the scattering region. Waves incident from the left and right lead (blue) are described by the coefficient vectors $\vec{u}_l$ and $\vec{u}_r$, respectively, whereas the outgoing scattered waves (red) are described by $\vec{v}_l$ and $\vec{v}_r$. Here, the subscript l (r) stands for the input from the left (right) waveguide port. In both cases, the scattering matrix is evaluated at $\partial\Omega$ (indicated by dashed black lines).

Assuming normalized input coefficients, i.e., $\vec{u}^\dagger\vec{u} = 1$, unitarity translates into the conservation of the norm of the coefficient vector since $\vec{v}^\dagger\vec{v} = \vec{u}^\dagger S^\dagger S\vec{u} = \vec{u}^\dagger\vec{u} = 1$. However, in the presence of gain or loss, $S^\dagger S \neq \mathbb{1}$.

In this thesis, we mostly consider two-port systems, where an example of such is shown in Fig. 1.1(b). Here, the coefficient vectors describing incoming and outgoing flux-normalized channels (see Chapter 2 for details about the flux normalization) are given by

$$\vec{u} = \begin{pmatrix} \vec{u}_l \\ \vec{u}_r \end{pmatrix}, \quad \vec{v} = \begin{pmatrix} \vec{v}_l \\ \vec{v}_r \end{pmatrix}, \tag{1.3}$$

where the subscript l (r) denotes an input from the left (right) waveguide port. In such a system, the scattering matrix can be written in the following block-partitioned form

$$S = \begin{pmatrix} r & t' \\ t & r' \end{pmatrix}. \tag{1.4}$$

Here, r and t are the reflection and transmission matrix for an input from the left waveguide port, respectively, and the primed quantities are the corresponding matrices for an input from the right waveguide port. More specifically, the elements of the sub-matrices $t_{mn}^{(\prime)}$ and $r_{mn}^{(\prime)}$ describe the transmission and reflection amplitudes from the n-th incident mode into the m-th outgoing mode, where $|t_{mn}^{(\prime)}|^2$ and $|r_{mn}^{(\prime)}|^2$ are the corresponding scattered intensities. The total transmission and reflection of a certain mode n incident from the left waveguide port is thus given by the sum over all outgoing propagating modes, i.e., $T_n = \sum_{m=1}^{M} |t_{mn}|^2$ and $R_n = \sum_{m=1}^{N} |R_{mn}|^2$, respectively, with M (N) being the number of outgoing modes in the right (left) lead. Provided that one uses flux-normalized input states, a flux-conserving scattering process with a unitary scattering matrix fulfills $T_n + R_n = 1$, where the same holds true for an input from the right waveguide port, i.e., $T'_n + R'_n = 1$. In turn, the total scattered output intensity is then equal to the number of flux-carrying input channels, i.e., $\sum_{n=1}^{N} T_n + R_n = N$ and $\sum_{n=1}^{M} T'_n + R'_n = M$. In this case, the reflection matrices r and r' are quadratic with dimensions $N \times N$ and $M \times M$, respectively, whereas t and t' are rectangular $M \times N$ and $N \times M$ matrices. Together, this yields a quadratic scattering matrix of size $(M+N) \times (M+N)$. For simplicity, we will consider the case of equally sized-waveguide ports in the following and thus $M = N$ yielding transmission and reflection matrices of size $N \times N$ and a scattering matrix of size $2N \times 2N$.

Using the block-matrix form Eq. (1.4), the first unitarity condition in Eq. (1.2), i.e., $S^\dagger S = \mathbb{1}$, translates into

$$t^\dagger t + r^\dagger r = t'^\dagger t' + r'^\dagger r' = \mathbb{1}\,, \tag{1.5}$$

$$r^\dagger t' + t^\dagger r' = t'^\dagger r + r'^\dagger t = 0\,, \tag{1.6}$$

while the second condition, i.e., $SS^\dagger = \mathbb{1}$, yields

$$tt^\dagger + r'r'^\dagger = t't'^\dagger + rr^\dagger = \mathbb{1}\,, \tag{1.7}$$

$$rt^\dagger + t'r'^\dagger = tr^\dagger + r't'^\dagger = 0\,. \tag{1.8}$$

These relations will be used in Chapter 5 since they relate the eigenvalues and eigenvectors of the matrices $t^{(\prime)\dagger}t^{(\prime)}$ and $r^{(\prime)\dagger}r^{(\prime)}$ as well as the ones of $t^{(\prime)}t^{(\prime)\dagger}$ and $r^{(\prime)}r^{(\prime)\dagger}$.

Apart from unitarity, the scattering matrix is also subject to reciprocity as it fulfills the so-called reciprocity (or Onsager) relations. These relations state that scattering from a mode n into another mode m and its reverse process, i.e., scattering from mode m into mode n, happen with the same amplitude. In terms of transmission and reflection amplitudes, this can be expressed as $t_{mn} = t'_{nm}$, $r_{mn} = r_{nm}$ and $r'_{mn} = r'_{nm}$. In matrix notation, the latter read as $t = t'^T$, $r = r^T$ and $r' = r'^T$, which can be summarized by a transposition symmetric scattering matrix

$$S = S^T\,. \tag{1.9}$$

It is important to note that reciprocity should not be confused with time-reversal symmetry, as the latter implies reciprocity, but not vice versa. For example, absorption breaks time-reversal symmetry, but not reciprocity. To break reciprocity, a time-varying refractive index distribution, a magnetic field or non-linear effects are required [10]. Both Eqs. (1.2) and (1.9) are important symmetries that will be used to confirm the numerically calculated scattering matrices in Chapter 2.

On an operator-based level, the scattering matrix can also be written in the *effective Hamiltonian* framework [68, 69] as

$$S = -\mathbb{1} + 2iV^{\dagger}GV \,, \tag{1.10}$$

where V contains the couplings between the channels in the asymptotic leads and the resonances (eigenfunctions) of the scattering region and G is the Green's function serving as the propagator inside the scattering region. The latter is given by $G = \mathcal{L}^{-1} = (G_0^{-1} + iVV^{\dagger})^{-1}$ with $G_0 = \mathcal{L}_0^{-1}$, where $\mathcal{L}_0$ is the differential operator of the closed cavity system and the second term $iVV^{\dagger}$ provides the coupling to the asymptotic regions thus opening the system making it non-Hermitian. For the scalar Helmholtz equation, the differential operator of the closed system reads $\mathcal{L}_0 = \Delta + n^2(\vec{r})k^2$, while $\mathcal{L}_0 = \vec{\nabla}\times\vec{\nabla}\times - n^2(\vec{r})k^2$ for the vector Helmholtz equation (see Appendix A). Thus, Eq. (1.10) describes the incoupling into the scattering region, the propagation therein and the final outcoupling into the asymptotic regions, where the negative unit matrix $-\mathbb{1}$ is necessary to correctly describe the reflection process[1]. Equation (1.10) is very useful as it does not require any basis representation of the scattering matrix, which makes it essential for the derivation of the main result of Chapter 3.

Having introduced the scattering matrix, which contains all the information about a scattering process, we proceed in the following section with the introduction of an operator that is based solely on this quantity.

1.2 The Wigner-Smith time-delay operator

In the following we introduce an operator whose eigenstates are optimal in the sense that they feature a well-defined propagation time through a given scattering system. The latter might be simple to determine in case of classical trajectories, however, the interfering nature of waves together with the ill-defined entrance and exit time of a wave packet or a time-harmonic plane wave makes this task all but trivial. The groundwork for the solution to this problem was laid more than 70 years ago by the PhD student of Eugene Wigner, Leonard Eisenbud, who theoretically investigated the properties of nuclear collision processes [35]. Eisenbud and Wigner showed in the field of nuclear scattering theory that the retardation of a wave due to the scattering at a potential can be extracted from the energy derivative of the scattering phase [36]. A few years later, Felix Smith generalized this result to multi-channel transport and introduced the lifetime matrix [37], which nowadays is known as the Wigner-Smith (or Eisenbud-Wigner-Smith) operator. Despite the complex nature of scattering processes, it takes the surprisingly simple form

---

[1] The $-\mathbb{1}$ is a result from the separation of the total field into incoming and scattered components, i.e., the reflected field at a specific port is given by the total field minus the incident mode one injects for calculating the reflection matrix elements in a certain column. The projection on the outgoing modes together with their orthonormality then gives rise to the negative unit matrix [see also, e.g., Eq. (2.31)]

$$Q_\omega^{(S)} = -iS^\dagger \frac{dS}{d\omega} \tag{1.11}$$

and is solely based on the multi-channel scattering matrix S introduced in the previous section. Here, the subscript denotes the quantity with respect to which the derivative of the scattering matrix is taken and the superscript indicates the matrix used for the construction of the operator. In the absence of gain and loss, the scattering matrix is unitary, i.e., $S^{-1} = S^\dagger$, giving rise to a Hermitian time-delay operator. This can be easily shown by using $S^\dagger(\omega)S(\omega) = \mathbb{1}$, which results in $\frac{d}{d\omega}\, i\big[S^\dagger(\omega)S(\omega)\big] = 0$. Evaluating and rearranging the latter directly gives

$$Q_\omega^{(S)} = -iS^\dagger \frac{dS}{d\omega} = i\frac{dS^\dagger}{d\omega}S = Q_\omega^{(S)\dagger}\,. \tag{1.12}$$

The Hermiticity of $Q_\omega^{(S)}$ implies real-valued eigenvalues τ_ω, which can be interpreted as proper physical time-delays of the scattered waves. Moreover, it gives rise to a complete and orthonormal set of eigenstates making them optimal in a temporal sense, e.g., the eigenstate corresponding to the shortest time-delay propagates fastest through a given scattering system. Just like in the single-channel case, the time-delays in the multi-channel case are also given by the frequency derivative of the global scattering phase of the corresponding output vector. More precisely, if $\vec{v} = S\vec{u} = \hat{v}|\vec{v}|e^{i\phi}$ is the corresponding output vector (with $\hat{v}$ being the unit vector of $\vec{v}$ specifying the direction in the modal coefficient space) for a time-delay eigenstate input vector $\vec{u}$, the corresponding eigenvalue is given by $\tau_\omega = d\phi/d\omega$ (see below).

With an entirely different motivation in mind, the time-delay operator was independently re-derived many years later in the field of multi-mode fiber physics. There, Shanhui Fan and Joseph Kahn introduced so-called principal modes which do not suffer from modal dispersion to first order [40]. In particular, for a fixed input wavefront, the corresponding output wavefront – typically given by a speckle – is independent of a small frequency change to first order (apart from a global change in brightness in case of a non-unitary scattering or transmission matrix). To demonstrate the derivation of the time-delay operator based on the demanded disperionlessness to first order, we consider a fiber transmission matrix $t(\omega)$ connecting an input coefficient vector $\vec{u}_l$ of modal amplitudes with the corresponding vector of outgoing coefficients $\vec{v}_r(\omega)$ via $\vec{v}_r(\omega) = t(\omega)\vec{u}_l$. Here, the input vector is independent of frequency, whereas the output vector is frequency-dependent due to the frequency-dependence of the transmission matrix. Performing a Taylor expansion of the output coefficient vector around ω_0 for a small change in frequency $\Delta\omega$

yields

$$\begin{aligned}\vec{v}_r(\omega_0+\Delta\omega) &= \vec{v}_r(\omega_0) + \left.\frac{d\vec{v}_r(\omega)}{d\omega}\right|_{\omega_0} \Delta\omega + \mathcal{O}(\Delta\omega^2) \\ &\approx t(\omega_0)\vec{u}_l + \left.\frac{dt(\omega)}{d\omega}\right|_{\omega_0} \vec{u}_l\,\Delta\omega\,.\end{aligned} \tag{1.13}$$

In the last line, we have neglected terms of order $\Delta\omega^2$, where we have also used the frequency-independence of the input vector $\vec{u}_l$. To obtain the desired dispersionlessness to first order, we now demand that the change in the output vector, i.e., the second term in the above Taylor-expansion, has to be parallel to the output vector itself at ω_0. More precisely, these two terms can only differ by a global amplitude and phase described by a complex number $z \in \mathbb{C}$, i.e.,

$$t(\omega_0)\vec{u}_l = z \left.\frac{dt(\omega)}{d\omega}\right|_{\omega_0} \vec{u}_l\,\Delta\omega\,. \tag{1.14}$$

Multiplying the above equation with $-i$ and rearranging it gives

$$\left(\frac{-i}{z\Delta\omega}\right)\vec{u}_l = \left(-it^{-1}(\omega_0)\left.\frac{dt(\omega)}{d\omega}\right|_{\omega_0}\right)\vec{u}_l\,. \tag{1.15}$$

The expression inside the brackets on the right-hand side can then be identified as the so-called group-delay operator

$$q_\omega^{(t)} \equiv -it^{-1}(\omega_0)\left.\frac{dt(\omega)}{d\omega}\right|_{\omega_0}\,, \tag{1.16}$$

which slightly differs from Eq. (1.11) due to the inverse transmission matrix being used instead of its Hermitian conjugate. The corresponding group-delay eigenvalue is given by the bracketed expression on the left-hand side, i.e., $\tau_\omega = (iz\Delta\omega)^{-1}$. To shed more light onto the analytical structure of the time-delay eigenvalue, we multiply Eq. (1.15) with t from the left and use $\partial\vec{u}_l/\partial\omega = 0$ to get

$$\tau_\omega\vec{v}_r = -i\left.\frac{d\vec{v}_r}{d\omega}\right|_{\omega_0}\,. \tag{1.17}$$

We now decompose the output vector as $\vec{v}_r = \hat{v}_r|\vec{v}_r|e^{i\phi}$, where $\hat{v}_r$ is the unit vector pointing in the corresponding direction in the high-dimensional modal coefficient space, $|\vec{v}_r|$ is its magnitude and ϕ is the global scattering phase. Using this decomposition, Eq. (1.17) becomes

$$\tau_\omega\hat{v}_r|\vec{v}_r|e^{i\phi} = \hat{v}_r|\vec{v}_r|\left.\frac{d\phi}{d\omega}\right|_{\omega_0} e^{i\phi} - i\hat{v}_r\left.\frac{d|\vec{v}_r|}{d\omega}\right|_{\omega_0} e^{i\phi}\,, \tag{1.18}$$

where we have used that $d\hat{v}_r/d\omega = 0$ due to the demanded frequency-independence to first order. Finally, the group-delay eigenvalue reads [40]

$$\tau_\omega = \left.\frac{d\phi}{d\omega}\right|_{\omega_0} - i\,\left.\frac{d\ln|\vec{v}_r|}{d\omega}\right|_{\omega_0} . \tag{1.19}$$

Equation (1.19) now shows, that the real part of the group-delay eigenvalue is given by the frequency derivative of the global phase of the output vector and can thus be interpreted as the time-delay of the corresponding wave [36]. Moreover, the imaginary part is a measure for the change of the transmitted intensity in case of a frequency detuning. At this stage, one might wonder about the appearance of an imaginary part in Eq. (1.19), however, $q_\omega^{(t)}$ and $Q_\omega^{(S)}$ are not exactly the same as the former only contains the transmission matrix, whereas the latter contains the full unitary scattering matrix. Since a unitary scattering matrix captures all the outgoing flux, which is equal to the incident flux, $d\ln|\vec{v}_r|/d\omega = d\ln|\vec{u}_l|/d\omega = 0$ leaves us with purely real-valued eigenvalues. The imaginary part of the eigenvalues of q_ω thus stems from the sub-unitarity of the transmission (or scattering) matrix which is typically weakly pronounced in fiber systems due to the lack of back-reflections (bending losses are dominant instead). However, since we are interested in strongly scattering systems, the computation of the inverse of $t(\omega)$ can be difficult as the latter can be singular. In this case, a pseudo-inverse can be calculated via the projection onto the non-singular subspace (see Appendix C).

The above derivation can of course also be carried out with the full scattering matrix (rather than only the transmission matrix) in which case the time-delay operator reads

$$q_\omega^{(S)} = -iS^{-1}\frac{dS}{d\omega} . \tag{1.20}$$

This expression is now identical to Eq. (1.11) if the scattering matrix is unitary ($S^{-1} = S^\dagger$). Non-unitarity, e.g., due to the presence of gain or loss or by not being able to measure all the outgoing flux-carrying channels, causes these two operator definitions to give very different results since they are related via

$$Q_\omega^{(S)} = S^\dagger S\, q_\omega^{(S)} . \tag{1.21}$$

Loosely speaking, $q_\omega^{(S)}$ encodes the phase delays, i.e., the frequency derivative of the scattering phases, whereas $Q_\omega^{(S)}$ additionally contains a weighting by the outgoing intensities in the respective channels. Also note that dispersionlessness to first order is by construction only a property of the eigenstates of q_ω and does not apply to the eigenstates of Q_ω in the non-unitary case.

To complete the picture of possible quantities measuring the duration of a scattering process, there also exists the concept of *dwell time* [38, 39, 70]. In its definition, the latter is entirely different from the frequency derivative of the scattering phases, however, a close relation to the concept of time-delay exists in case of flux-conserving scattering processes. For a stationary scalar scattering state $\psi(\vec{x})$, the dwell time is defined as [71]

$$\tau_d = \frac{U_\Omega}{S^{(\mathrm{in})}_{\partial\Omega}} = \frac{2k}{ic} \frac{\int_\Omega \psi^*(\vec{x}) n^2(\vec{x}) \psi(\vec{x})\, dV}{\int_{\partial\Omega} [\psi(\vec{x}) \vec{\nabla} \psi^*(\vec{x}) + \mathrm{c.c.}] \cdot d\vec{A}}\,, \tag{1.22}$$

where U_Ω is the time-averaged stored intensity inside the scattering region Ω and $S^{(\mathrm{in})}_{\partial\Omega}$ is the incoming power flux (for the corresponding expressions we refer to Ref. [71]). Most interestingly, the corresponding dwell time operator Q_d can be related to the time-delay operator by [48, 49]

$$Q_d = Q^{(S)}_\omega + Q^{(e)}_\omega + Q^{(i)}_\omega\,. \tag{1.23}$$

Here, $Q^{(e)}_\omega$ describes contributions from evanescent modes which can typically be neglected (except at the onset of a new propagating mode) and $Q^{(i)}_\omega$ describes self-interferences, i.e., interferences of the incident and scattered field, which only become important in strongly reflecting systems [49]. In the effective Hamiltonian framework [see Eq. (1.10)], $Q^{(i)}_\omega$ can also be traced back to the energy dependence of the coupling matrix V which typically gets neglected [48]. Apart from that, the average dwell time also shares a close relation with the density of optical states (DOS) in the scattering system $\rho(\omega)$ [72]

$$\langle \tau_d(\omega) \rangle = \frac{2\pi}{N_{\mathrm{in}}(\omega)} \rho(\omega)\,, \tag{1.24}$$

where $N_{\mathrm{in}}(\omega)$ is the total number of incoming scattering channels. Assuming that $Q_d \approx Q^{(S)}_\omega$, we can thus also relate the average time-delay of all scattering channels $\langle Q^{(S)}_\omega \rangle = \mathrm{Tr}(Q^{(S)}_\omega)/N_{\mathrm{in}}$ with the density of states.

The introduction of Wigner-Smith time-delay has sparked an entire field of research and we extend and generalize this concept in the remaining parts of this thesis. However, before doing so, we specify our system of choice and the corresponding set of basis states in which we represent the scattering matrix in the following section.

1.3 Waveguide geometries and eigenmodes

In this section, we specify the two-port geometry that we will focus on and its corresponding eigenmodes which serve as a basis in which we represent a scattering matrix. Throughout most of this thesis, we consider rectangular, metallic, straight two-port waveguides of width W, height h and length L [see Fig. 1.2(a)]. To induce scattering, we usually add a non-uniform refractive index distribution – either in

Die approbierte gedruckte Originalversion dieser Dissertation ist an der TU Wien Bibliothek verfügbar.
The approved original version of this doctoral thesis is available in print at TU Wien Bibliothek.
TU Bibliothek, WIEN Your knowledge hub

form of a continuous distribution $n(\vec{r})$ [depicted as dark spots in Fig. 1.2(a)] or by placing obstacles with a certain refractive index – in its interior. However, the asymptotic regions, i.e., the waveguide ports, feature a uniform refractive index making it possible to decompose any incident or scattered wave into the complete and orthonormal set of eigenstates of the clean waveguide cross section. In general, there are two sets of modes, namely the transverse electric (TE) and transverse magnetic (TM) modes, whose electric and magnetic field only features components transverse to the direction of propagation, respectively.

To obtain an analytical expression of the TE modes, we first write their electric field as a transverse profile ($E_x = 0$) with a plane-wave propagation in the longitudinal direction, i.e.,

$$\vec{E}^{\,\mathrm{TE}}(\vec{r},t) = \begin{pmatrix} 0 \\ E_y^{\mathrm{TE}}(y,z) \\ E_z^{\mathrm{TE}}(y,z) \end{pmatrix} e^{i(k_x x - \omega t)} \,. \tag{1.25}$$

Here, $\omega = kc$ is the frequency with $k = 2\pi/\lambda$ being the free space wave vector and c being the speed of light in vacuum. Next, the perfectly electric conductor (PEC) boundary conditions impose that the tangential electric field at the waveguide boundaries vanishes, i.e.,

$$E_y^{\mathrm{TE}}(y,0) = E_y^{\mathrm{TE}}(y,h) = E_z^{\mathrm{TE}}(0,z) = E_z^{\mathrm{TE}}(W,z) = 0\,. \tag{1.26}$$

To calculate $E_y^{\mathrm{TE}}(y,z)$ and $E_z^{\mathrm{TE}}(y,z)$, we insert Eq. (1.25) into Maxwell's equations. Thereby, the uniform refractive index in the waveguide ports together with the time-harmonic excitation in Eq. (1.25) causes Maxwell's equations to reduce to the scalar Helmholtz equation (see Appendix A) for all vector components. For $n(\vec{r}) = 1$ in the leads, we thus get

$$\left(\Delta_t + k^2 - k_x^2\right) E_y^{\mathrm{TE}}(y,z) = 0\,, \tag{1.27}$$

$$\left(\Delta_t + k^2 - k_x^2\right) E_z^{\mathrm{TE}}(y,z) = 0\,, \tag{1.28}$$

where $\Delta_t = \partial_y^2 + \partial_z^2$ is the transverse Laplacian. Due to the geometrical independence of the y- and z-component in the waveguide cross section, we can make a separation ansatz $E_y(y,z) = f_y(y)g_y(z)$ and $E_z(y,z) = f_z(y)g_z(z)$. Imposing now Eq. (1.26) determines $g_y(z)$ and $f_z(y)$, where $f_y(y)$ and $g_z(z)$ get fixed by the Maxwell equation $\vec{\nabla}\cdot\vec{D} = 0$ with $\varepsilon_r = n^2 = 1$ in the leads. Putting everything together, the electric field of the TE modes is given by

$$\vec{E}_{mn}^{\,\mathrm{TE}}(\vec{r},t) = \mathcal{N}_E^{\mathrm{TE}} \begin{pmatrix} 0 \\ -k_{z,n}\cos(k_{y,m}y)\sin(k_{z,n}z) \\ k_{y,m}\sin(k_{y,m}y)\cos(k_{z,n}z) \end{pmatrix} e^{i(k_{x,mn}x - \omega t)}\,, \tag{1.29}$$

where $k_{x,mn} = \sqrt{k^2 - k_{y,m}^2 - k_{z,n}^2}$ is the longitudinal propagation constant of the mode and its transverse wave vectors are given by $k_{y,m} = m\pi/W$ and $k_{z,n} = n\pi/h$.

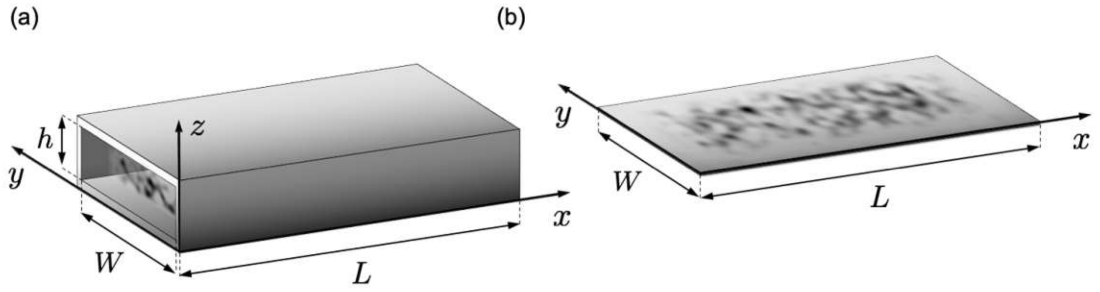

Figure 1.2: (a) Rectangular, metallic two-port waveguide of length L, width W and height h featuring an inhomogeneous refractive index distribution in its interior (dark spots). (b) For $h \ll W$ and a refractive index distribution $n = n(x, y)$ independent of z, the 3D waveguide geometry from (a) can be mapped to an equivalent 2D waveguide in which only TE_{m0} modes propagate.

Moreover, $\mathcal{N}_E^{\mathrm{TE}}$ is a normalization factor which ensures that $\iint_{\mathrm{port}} |\vec{E}_{mn}^{\mathrm{TE}}|^2 \, dy \, dz = 1$. From Eq. (1.29) one can see that these modes only exist if $m > 0$ or/and $n > 0$, i.e., there is no solution for both $m = n = 0$. The corresponding magnetic $\vec{H}$-field of the TE mode can then be calculated via the Maxwell equation

$$\vec{\nabla} \times \vec{E}(\vec{r}, t) = -\frac{\partial \vec{B}(\vec{r}, t)}{\partial t} = i\omega\mu_0\mu_r \vec{H}(\vec{r}, t) \,, \tag{1.30}$$

with $\mu_r = 1$ and gives

$$\vec{H}_{mn}^{\mathrm{TE}}(\vec{r}, t) = \mathcal{N}_H^{\mathrm{TE}} \begin{pmatrix} -i(k_{y,m}^2 + k_{z,n}^2) \cos(k_{y,m} y) \cos(k_{z,n} z) \\ -k_{x,mn} k_{y,m} \sin(k_{y,m} y) \cos(k_{z,n} z) \\ -k_{x,mn} k_{z,n} \cos(k_{y,m} y) \sin(k_{z,n} z) \end{pmatrix} e^{i(k_{x,mn} x - \omega t)} \,. \tag{1.31}$$

Here, $\mathcal{N}_H^{\mathrm{TE}}$ is the corresponding normalization factor for the $\vec{H}$-field ensuring that $\iint_{\mathrm{port}} |\vec{H}_{mn}^{\mathrm{TE}}|^2 \, dy \, dz = 1$.

The second set of modes are the TM modes which feature a purely transverse magnetic field, i.e., $H_x = 0$. To obtain an analytical expression, we can write their $\vec{H}$-field as

$$\vec{H}^{\,\mathrm{TM}}(\vec{r}, t) = \begin{pmatrix} 0 \\ H_y^{\mathrm{TM}}(y, z) \\ H_z^{\mathrm{TM}}(y, z) \end{pmatrix} e^{i(k_x x - \omega t)} \,. \tag{1.32}$$

The PEC boundary condition imposes that the $\vec{H}$-field should be tangential at the waveguide walls, i.e,

$$H_y^{\mathrm{TM}}(0, z) = H_y^{\mathrm{TM}}(W, z) = H_z^{\mathrm{TM}}(y, 0) = H_z^{\mathrm{TM}}(y, h) = 0 \,. \tag{1.33}$$

Following the derivation above, one can make a similar separation ansatz, impose the boundary conditions in Eq. (1.33) and use $\vec{\nabla}\cdot B = 0$ to determine all unknowns which yields

$$\vec{H}^{\mathrm{TM}}_{mn}(\vec{r},t) = \mathcal{N}^{\mathrm{TM}}_{H}\begin{pmatrix} 0 \\ k_{z,n}\sin(k_{y,m}y)\cos(k_{z,n}z) \\ -k_{y,m}\cos(k_{y,m}y)\sin(k_{z,n}z)\end{pmatrix} e^{i(k_{x,mn}x-\omega t)}\,. \tag{1.34}$$

In contrast to the TE modes, Eq. (1.34) shows that TM modes only exist if both $m > 0$ and $n > 0$. Using the Maxwell equation

$$\vec{\nabla}\times\vec{H}(\vec{r},t) = \frac{\partial\vec{D}(\vec{r},t)}{\partial t} = -i\omega\varepsilon_0\varepsilon_r\vec{E}(\vec{r},t) \tag{1.35}$$

with $\varepsilon_r = 1$ in the leads lets us derive the $\vec{E}$-field of the TM modes

$$\vec{E}^{\mathrm{TM}}_{mn}(\vec{r},t) = \mathcal{N}^{\mathrm{TM}}_{E}\begin{pmatrix} i(k^2_{y,m}+k^2_{z,n})\sin(k_{y,m}y)\sin(k_{z,n}z) \\ -k_{x,mn}k_{y,m}\cos(k_{y,m}y)\sin(k_{z,n}z) \\ -k_{x,mn}k_{z,n}\sin(k_{y,m}y)\cos(k_{z,n}z)\end{pmatrix} e^{i(k_{x,mn}x-\omega t)}\,. \tag{1.36}$$

Alternatively, the analytical expression of the TM modes can also be derived via the longitudinal field $E_x(y,z)$ which can be obtained by solving the corresponding scalar Helmholtz equation subject to the PEC boundary conditions [73]. The transverse components of the electric field are then fully determined by its longitudinal component, where the full $\vec{H}$-field can be calculated using Maxwell's equation (1.30).

Both sets of basis states are required for a full description of a scattering process in a waveguide. Most importantly, TE_{mn} and TM_{mn} are degenerate in terms of their $k_{y,m}$ and $k_{z,n}$ wave vectors which makes a scattering-induced transition between these two sets of basis states very likely. Thus, both sets of modes have to be taken into account when determining the scattering matrix as otherwise the latter is not unitary (see Section 2.2). The $\vec{E}$-field intensities of TE and TM modes are now depicted in Fig. 1.3 and the corresponding $\vec{H}$-field intensities are shown in Fig. 1.4.

If the height of the considered waveguide in z-direction is small (such that the TE_{mn} or TM_{mn} modes with $n > 0$ in this direction cannot be excited) and the refractive index distribution $n(\vec{r}) = n(x,y)$ does not depend on z, the vectorial 3D problem can be reduced to a scalar 2D problem in the xy-plane (see Appendix A). In this case, TM modes do not exist, and the remaining set of TE_{m0} modes can be simplified to the only non-zero polarization component of these modes, i.e., the z-component. The latter are then used as basis functions in a scalar description and read

$$\chi_m(\vec{r},t) \equiv E^{\mathrm{TE}}_{z,m0}(\vec{r},t) = \sqrt{\frac{2}{W}}\sin(k_{y,m}y)e^{i(k_{x,m}x-\omega t)} \tag{1.37}$$

Die approbierte gedruckte Originalversion dieser Dissertation ist an der TU Wien Bibliothek verfügbar.
The approved original version of this doctoral thesis is available in print at TU Wien Bibliothek.
TU Bibliothek WIEN Your knowledge hub

with $\vec{r} = (x, y)$ and $k_{x,m} \equiv k_{x,m0} = \sqrt{k^2 - k_{y,m}^2}$. Note that modes with transverse wave vectors smaller than k are propagating as their longitudinal propagation constants $k_{x,m}$ are purely real, whereas modes with transverse wave vectors larger than k have purely imaginary k_x-values. The latter then gives rise to exponentially decaying waves called evanescent modes which do not contribute to the calculation of the scattering matrix as they carry no flux (even though they do contribute locally in a scattering process).

Since the scattering matrix's unitarity reflects flux conservation, the above mentioned basis states also have to be normalized to unit flux (in addition to the already applied intensity normalization). In other words, to treat all modes equally despite their different longitudinal flux

$$j_x = \mathrm{Re}\left[e^{-ik_{x,m}x}(-i\partial_x)e^{ik_{x,m}x}\right] = k_{x,m}\,, \tag{1.38}$$

we have to normalize their transverse profiles by $1/\sqrt{k_{x,m}}$ which is essential in order to obtain a unitary scattering matrix. In the following, we denote flux-normalized wave functions by a tilde, e.g., $\tilde{\chi}_m = \chi_m/\sqrt{k_{x,m}}$ (the same normalization applies in 3D in which case $k_{x,m} \to k_{x,mn}$). The expressions for the scattering matrix elements for non-flux-normalized input states are also given in Section 2.1 and 2.2.

Considering now two-port devices with one port at $x = 0$ and the second port at $x = L$, using the longitudinal plane wave propagation factor in the above definitions of the TE and TM modes at both ports results in a propagation phase relative to the phase acquired during propagation in free space (since the basis functions at the second port contain the factor $e^{ik_{x,m}L}$). However, typical measurements in microwave setups yield the absolute acquired phase. To also numerically obtain the absolute phase, e.g., $k_{x,m}L$ for a propagation in an empty waveguide section of length L, we thus use shifted basis functions with $x \to (x - L)$ at the second waveguide port at $x = L$ which makes the exponential factor of the modes vanish at both ports (the harmonic time-dependence has already been separated out in the derivation of the vector or scalar Helmholtz equation).

Last, we want to point out that the choice of basis states is arbitrary, i.e., any complete and orthogonal set of basis states can be used in the calculation of the scattering matrix. Apart from the waveguide modes derived above, another possible choice of basis states are the eigenstates of the transverse position operator. Each of its eigenstates is located around a certain spatial position given by the corresponding eigenvalues and thus they closely resemble the spatially resolved "pixel basis" of SLMs in optics. To obtain these eigenstates, the transverse position operator y in 2D is represented in the basis of waveguide modes, where the corresponding matrix elements read

$$y_{mn}^{\{m\}} = \int_0^W \chi_m^*(y)\, y\, \chi_n(y)\, dy\,. \tag{1.39}$$

Diagonalizing this operator then gives a matrix $Y = (\vec{y}^{\,(1)}, \ldots, \vec{y}^{\,(N)})$ which contains the modal coefficients of the position eigenstates column-wise. The transformation of, e.g., the transmission matrix from the mode basis to the basis of position eigenstates can then be performed via $t^{\{y\}} = Y^\dagger t^{\{m\}} Y$. The resulting matrix elements $t^{\{y\}}_{mn}$ then describe the scattering from the n-th spatial position at the first port to the m-th spatial position at the second port of the waveguide. This set of basis states will, e.g., be used in Chapter 4. For completeness, we also mention another popular choice of basis states often used in optics which is given by the angular basis in which each input state features a single well-defined angle. To numerically obtain such states, we represent the transverse momentum operator $k_y = -i\partial_y$ in the modal basis

$$k^{\{m\}}_{y,mn} = \int_0^W \chi^*_m(y)\,(-i\partial_y)\,\chi_n(y)\,dy\,. \tag{1.40}$$

In analogy to the position operator, diagonalizing $k^{\{m\}}_y$ yields a matrix K_y which contains the modal coefficients of the transverse momentum eigenstates columnwise, where their transverse momentum is given by their corresponding eigenvalue. Again, transforming the transmission matrix to this basis can be done via $t^{\{k_y\}} = K^\dagger_y t^{\{m\}} K_y$.

Having introduced multiple sets of complete and orthonormal basis states in which we can represent a scattering matrix, we now proceed in the following chapter to the numerical solution of the scattering problem in the specified waveguide systems, where we focus on the solution of the time-harmonic Maxwell's equations. Specifically, Section 2.1 is devoted to numerically solving the two-dimensional scalar Helmholtz equation, whereas Section 2.2 describes the solution strategy for the full-vectorial problem in three dimensions.

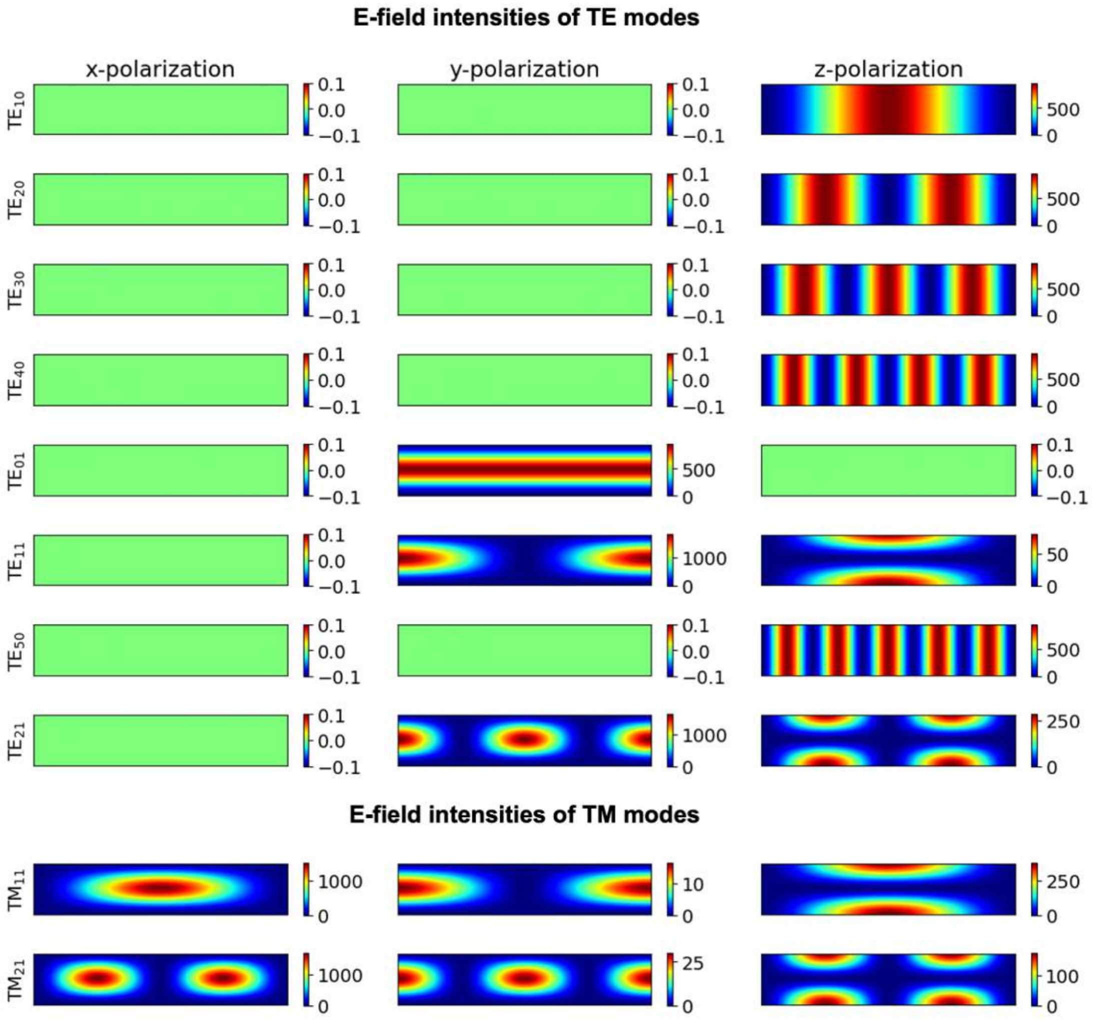

Figure 1.3: Transverse electric field intensities of TE (top) and TM (bottom) modes for the waveguide cross section of the system shown in Fig. 2.5. This set of basis states is also used in the calculation of the scattering matrix in Fig. 2.6. The TE modes only feature a transverse electric field, while the TM modes also feature a longitudinal electric field component.

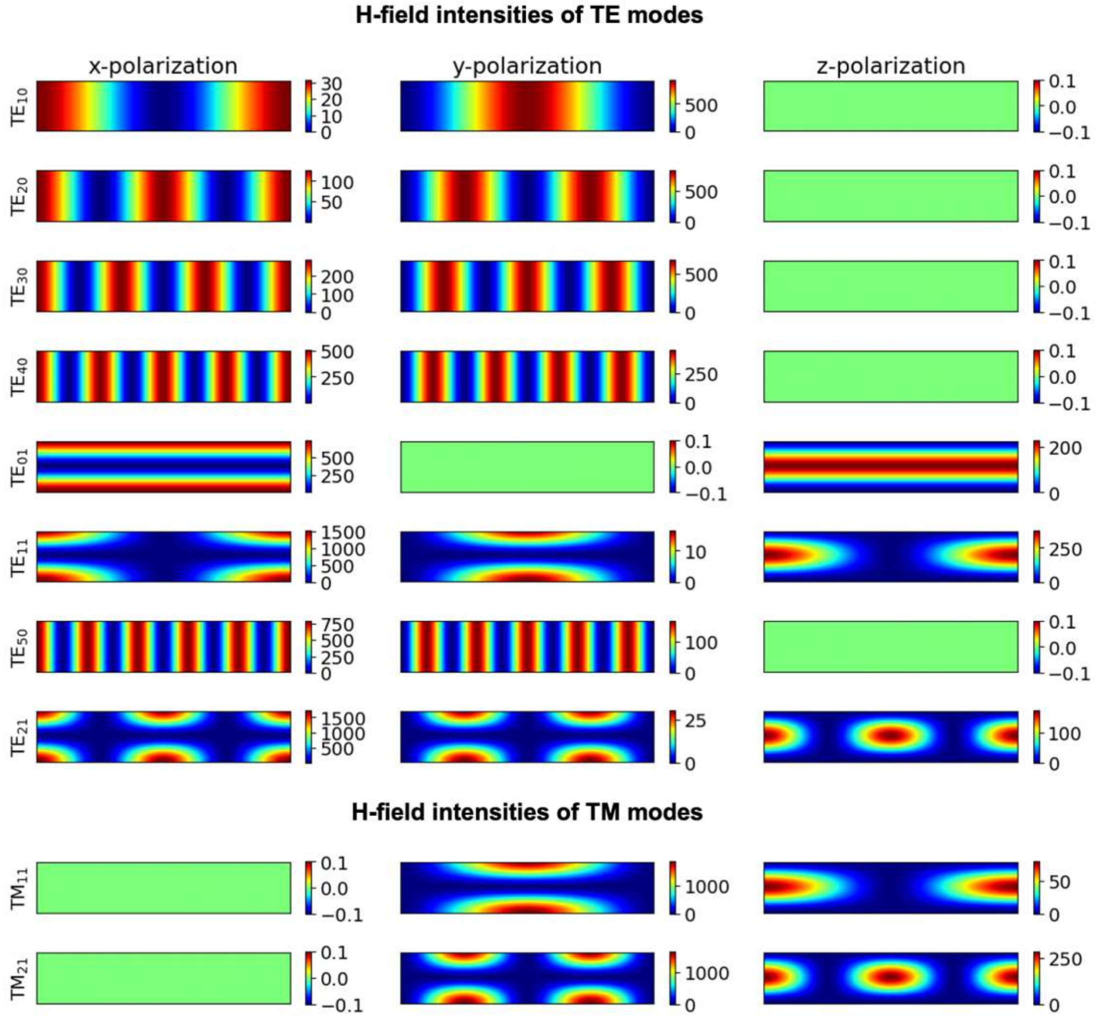

Figure 1.4: Transverse magnetic field intensities of TE (top) and TM (bottom) modes for the waveguide cross section of the system shown in Fig. 2.5. Just like for the $\vec{E}$-field of the TE modes, the $\vec{H}$-field of the TM modes is exclusively transverse.

Chapter 2

Numerical framework

To numerically solve an electromagnetic scattering problem and thus obtain the scattering matrix, we have to solve the underlying differential equations, namely Maxwell's equations. The most popular choices for full-wave solvers are finite difference methods like, e.g., the finite difference time-domain method and the finite element method (FEM). Note that full-wave solvers are required in the strongly scattering regime mainly considered in this thesis whereas, in other cases, approximations like, e.g., the paraxial approximation widely used in so-called beam propagation methods can be applied, reducing the complexity of the underlying differential equations. While finite difference methods are relatively simple to implement due to their orthogonal grids, this also leads to one of the major drawbacks of these methods – an inefficiency in modeling complex shapes. Thus, our method of choice is the FEM, which enables a straightforward treatment of complex geometries and material discontinuities using irregular grids. Moreover, it also brings the advantage of being able to easily use higher order basis functions as well as curvilinear elements for a more precise approximation of curved boundaries. For the numerical implementation, we use the open-source finite element package *NGSolve* [74, 75] (https://ngsolve.org) developed by Joachim Schöberl and his group at TU Wien which provides a very general framework for solving partial differential equations on unstructured meshes. Based on this framework, we develop an accurate and flexible numerical tool for solving two- and three-dimensional electromagnetic scattering problems in waveguide-like geometries. Specifically, we discuss the FEM solution strategy for the two-dimensional scalar Helmholtz equation and the three-dimensional vector Helmholtz equation as well as the calculation of the scattering parameters in the subsequent sections. Fore a more detailed description of the FEM including comparisons to other popular methods, we refer to Ref. [76], a very thorough description of the FEM can be found in Ref. [77].

The FEM is very well suited for solving partial differential equations subject to certain boundary conditions and its name stems from the geometric decomposition of the computational domain into small elements. In their simplest form, these elements are given by line elements in 1D, triangular elements in 2D and tetrahedral elements in 3D. The core idea of the FEM is the representation of a solution in terms of locally-supported, piecewise basis functions with known shapes but unknown amplitudes on all the elements. Thus, in contrast to finite difference methods in which each grid point is associated with a single value, the discretized solution in a FEM yields amplitudes representing the coefficients of the corresponding basis functions on each element (in dimensions higher than 1, one cannot only choose the shape of the basis functions, but also the shape of the elements). In other words, the FEM approximates the solution of a partial differential equation instead of approximating the differential operators like in finite difference methods. Since we deal with partial differential equations, the basis functions have to be differentiable and thus they are typically chosen to be polynomials. Moreover, their element-wise definition allows the calculation on a reference element which is then mapped to the actual element in the mesh. Together, this leads to a discretized differential operator whose matrix elements are non-zero only in close proximity of each individual element in the mesh. Furthermore, these non-vanishing matrix elements are fairly easy to calculate. This in turn yields sparse matrices whose inversion can be performed very efficiently. The FEM comes in two formulations: The first one is the so-called *Ritz variational method* which is based on the variational problem of a functional whose minimum yields the discretized solution of the partial differential equation. The second one is the *Galerkin weighted residual (error) method* in which the weighted difference of the left- and right-hand side of a differential equation is minimized in an average sense (not point-wise). Both methods typically yield the same results, but since it might be difficult in some cases to find a corresponding functional, we stick with the Galerkin weighted residual approach in the following. Also note that boundary conditions must be explicitly imposed as we will show in the following.

2.1 Stationary scattering in 2D waveguides

Throughout most of this thesis, we will consider time-harmonic, scalar scattering problems in two dimensions which are governed by the scalar Helmholtz equation (details about its derivation can be found in the Appendix A). In its most general form together with (possibly mixed) boundary conditions, it reads

$$\begin{aligned} \left[\Delta + n(\vec{r})^2 k^2\right] \psi(\vec{r}) &= -f(\vec{r}) \quad \text{in } \Omega\,, && (2.1)\\ \psi(\vec{r}) &= g_D(\vec{r}) \quad \text{on } \Gamma_D\,, && (2.2)\\ \partial_n \psi(\vec{r}) &= g_N(\vec{r}) \quad \text{on } \Gamma_N\,, && (2.3) \end{aligned}$$

where $\psi(\vec{r}) = E_z(\vec{r})$ is the unknown transverse z-component of the electric field, $\vec{r} = (x, y)^T$ is the position vector, Δ is the Laplace operator in two dimensions and $n(\vec{r})$ is the refractive index distribution. Moreover, $k = 2\pi/\lambda$ is the free space wave vector and $f(\vec{r})$ is a source (or driving) term. The Helmholtz equation itself is

Die approbierte gedruckte Originalversion dieser Dissertation ist an der TU Wien Bibliothek verfügbar.
The approved original version of this doctoral thesis is available in print at TU Wien Bibliothek.
TU Bibliothek WIEN Your knowledge hub

defined on the whole domain Ω, whereas the boundary conditions are only applied on the Dirichlet and Neumann boundaries Γ_D and Γ_N, respectively. There also exists a third type of boundary condition usually referred to as mixed or Robin boundary condition[2]

$$\partial_n\psi(\vec{r}\,) + \eta\,\psi(\vec{r}\,) = g_R(\vec{r}\,) \quad \text{on } \Gamma_R \tag{2.4}$$

with constant η that reduces to a Neumann boundary condition for $\eta = 0$. For $\eta > 0$, Eq. (2.4) can be implemented as a Neumann boundary, where $\psi(\vec{r}\,)$ on Γ_R must be introduced as an additional unknown.

We now follow Ref. [78] and multiply the differential equation with a so-called *test function* (or weighting function) v and integrate it over the whole domain Ω

$$\int_\Omega (\Delta\psi)\, v\, d\Omega + \int_\Omega n^2k^2\, \psi\, v\, d\Omega = -\int_\Omega f\, v\, d\Omega\,. \tag{2.5}$$

Note that we omitted all spatial dependencies for the sake of clarity. Next, we use Green's first identity

$$\begin{aligned}\int_\Omega (\Delta\psi)\, v\, d\Omega + \int_\Omega \vec{\nabla}\psi\cdot\vec{\nabla}v\, d\Omega &= \int_\Gamma (\partial_n\psi)\, v\, d\Gamma \\ &= \int_{\Gamma_D} (\partial_n\psi)\, v\, d\Gamma + \int_{\Gamma_N} (\partial_n\psi)\, v\, d\Gamma\end{aligned} \tag{2.6}$$

in order to “shift” one derivative to the test function. This reduces the maximum order of spatial derivatives acting on the target function ψ, which has caused the term *weak form of the differential equation*. Thus, we arrive at

$$\int_\Omega \vec{\nabla}\psi\cdot\vec{\nabla}v\, d\Omega - \int_\Omega n^2k^2\, \psi\, v\, d\Omega = \int_\Omega f\, v\, d\Omega + \int_{\Gamma_N} g_N\, v\, d\Gamma + \int_{\Gamma_D} (\partial_n\psi)\, v\, d\Gamma\,, \tag{2.7}$$

where we already inserted the Neumann boundary condition from Eq. (2.3). Since we do not know the value of $\partial_n\psi$ on the Dirichlet boundary Γ_D, we impose that $v = 0$ on Γ_D. The latter is not to be confused with the Dirichlet boundary condition for ψ which we have not applied yet. Since the Neumann boundary condition already appears inside the formulation Eq. (2.7), it is usually called a *natural boundary condition*, whereas the Dirichlet boundary condition is called an *essential boundary condition* and has to be imposed explicitly on the solution (see below). Thus, the resulting weak form of the scalar Helmholtz equation reads

$$\int_\Omega \vec{\nabla}\psi\cdot\vec{\nabla}v\, d\Omega - \int_\Omega n^2k^2\, \psi\, v\, d\Omega = \int_\Omega f\, v\, d\Omega + \int_{\Gamma_N} g_N\, v\, d\Gamma\,. \tag{2.8}$$

---

[2] One prominent example is the Sommerfeld radiation condition which reads (in two dimensions) $\lim_{r\to\infty} r^{1/2}\left[\frac{\partial\psi(\vec{r}\,)}{\partial r} - i\omega\psi(\vec{r}\,)\right] = 0$ with $r = |\vec{r}\,|$.

Note that ψ is also typically referred to as *trial function*[3]. In a next step, we have to discretize the above equation by expanding the solution ψ in a suitable set of basis functions. Since the solution corresponds to the transverse part of the electric field, which has to be continuous according to Eq. (A.7), we use basis functions that belong to the gradient-conforming Sobolev space $H^1(\Omega)$. This function space is spanned by those square-integrable continuous functions whose gradients are square integrable as well, i.e., [79]

$$H^1(\Omega) = H(\mathrm{grad};\Omega) = \{\psi \in L_2(\Omega) : \vec{\nabla}\psi \in [L_2(\Omega)]^2\}\,. \tag{2.9}$$

In the discretized formulation of the FEM, the necessity of ψ being differentiable can be relaxed to being piecewise differentiable. In the simplest form, one typically chooses piecewise polynomial functions, where a suitable basis of the resulting function space is given by the so-called nodal basis functions φ_i satisfying

$$\varphi_i(\vec{p}_j) = \delta_{ij} \tag{2.10}$$

with δ_{ij} being the Kronecker delta, i.e., they are 1 on their corresponding node $\vec{p}_i$ and 0 on all the other nodes $\vec{p}_j$ with $j \neq i$. In general, the number of nodes is larger than the number of mesh vertices, which comes from the fact that introducing higher-order nodal basis functions requires additional supporting points (nodes) between mesh vertices [78]. Only for the lowest, i.e., first order polynomial basis functions, the number of vertices is equal to the number of nodes. In that case, the basis functions can be defined on the reference triangle with vertices $\vec{p}_1 = (0,0)$, $\vec{p}_2 = (1,0)$ and $\vec{p}_3 = (0,1)$ as

$$\varphi_1(x,y) = 1 - x - y\,, \tag{2.11}$$

$$\varphi_2(x,y) = x\,, \tag{2.12}$$

$$\varphi_3(x,y) = y\,, \tag{2.13}$$

which are shown in Fig. 2.1. Using the property in Eq. (2.10), we can discretize the unknown solution by expanding it into such nodal basis functions

$$\begin{aligned}\psi_h &= \sum_{j\,\in\,\Omega} c_j\,\varphi_j \\ &= \sum_{j\,\in\,\Omega_F} c_{F,j}\,\varphi_j + \sum_{j\,\in\,\Gamma_D} g_{D,j}\,\varphi_j\,,\end{aligned} \tag{2.14}$$

where ψ_h denotes the discretized solution and $c_j = \psi_h(\vec{p}_j)$ are the expansion coefficients. We have also split the solution in a part defined on the free degrees of

---

[3] This term comes from putting a given alleged solution ψ “on trial”, i.e., one would substitute it into Eq. (2.8) and check the equality of the left- and right-hand side of Eq. (2.8) for all test functions v.

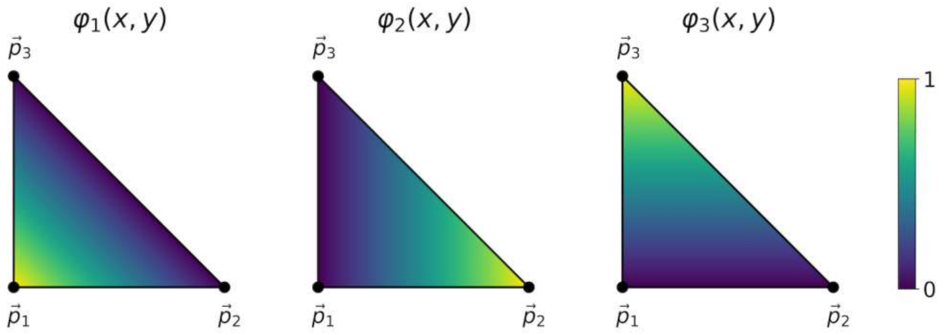

Figure 2.1: Nodal basis functions Eqs. (2.11)-(2.13) on the reference triangle whose vertices are marked by black dots. The colors represent the values of the basis functions which fulfill Eq. (2.10).

freedom $\Omega_F = \Omega \setminus \Gamma_D$ (denoted by the subscript F) and another part which contains only the prescribed data in order to explicitly enforce the Dirichlet boundary condition. For the latter, we have already inserted the Dirichlet data, i.e., $c_j = g_{D,j}$ for $j \in \Gamma_D$. Following the *Galerkin method*, we choose the basis functions φ_i as discretized test functions $v_{h,i}$. Replacing ψ and v in Eq. (2.8) with their discretized versions then yields

$$\begin{aligned}\sum_{j\,\in\,\Omega_F}\left(\int_\Omega \vec{\nabla}\varphi_j\cdot\vec{\nabla}\varphi_i\,d\Omega - \int_\Omega n^2k^2\,\varphi_j\,\varphi_i\,d\Omega\right)c_{F,j} &= \int_\Omega f\,\varphi_i\,d\Omega \\ &+ \int_{\Gamma_N} g_N\,\varphi_i\,d\Gamma - \sum_{j\,\in\,\Gamma_D}\left(\int_\Omega \vec{\nabla}\varphi_j\cdot\vec{\nabla}\varphi_i\,d\Omega - \int_\Omega n^2k^2\,\varphi_j\,\varphi_i\,d\Omega\right)g_{D,j}\end{aligned} \tag{2.15}$$

for all indices $i \in \Omega_F$. This set of equations can be written in matrix form by defining the so-called *stiffness matrix* K and *(modified) mass matrix*[4] M whose elements are given by

$$K_{ij} = \int_\Omega \vec{\nabla}\varphi_j\cdot\vec{\nabla}\varphi_i\,d\Omega\,, \tag{2.16}$$

$$M_{ij} = -\int_\Omega n^2k^2\,\varphi_j\,\varphi_i\,d\Omega\,, \tag{2.17}$$

respectively. The right-hand side of Eq. (2.15) only contains known quantities and the first two integrals can be written as a vector $\vec{b}$ with elements

$$b_i = \int_\Omega f\,\varphi_i\,d\Omega + \int_{\Gamma_N} g_N\,\varphi_i\,d\Gamma\,. \tag{2.18}$$

---

[4] The terminology "stiffnesss" and "mass" matrix stems from mechanical engineering.

The assembly of the quantities in Eq. (2.16)-(2.18) is provided by NGSolve[5] and defining the matrix $A = K + M$ allows us to write Eq. (2.15) in the following form

$$\sum_{j\,\in\,\Omega_F} A_{ij}\, c_{F,j} = b_i - \sum_{j\,\in\,\Gamma_D} A_{ij}\, g_{D,j}\,. \tag{2.19}$$

To solve this square system of linear equations, the boundary data g_D has to be interpolated onto the Dirichlet nodes and extended to zero on all elements in Ω which have no overlap with Γ_D resulting in the coefficient vector $\vec{c}_D$. Thus, Eq. (2.19) becomes

$$A\vec{c}_F = \vec{b} - A\vec{c}_D\,, \tag{2.20}$$

which can also be written as[6]

$$\begin{pmatrix} A_{FF} & A_{FD} \\ A_{DF} & A_{DD} \end{pmatrix} \begin{pmatrix} \vec{c}_{F,F} \\ \vec{0} \end{pmatrix} = \begin{pmatrix} \vec{b}_F \\ \vec{b}_D \end{pmatrix} - \begin{pmatrix} A_{FF} & A_{FD} \\ A_{DF} & A_{DD} \end{pmatrix} \begin{pmatrix} \vec{c}_{D,F} \\ \vec{c}_{D,D} \end{pmatrix}. \tag{2.21}$$

Note that $\vec{c}_D$ also contributes to the free degrees of freedom which is a result from the above mentioned extension of the Dirichlet boundary data into the domain Ω. The first line of Eq. (2.21) then reads

$$\begin{aligned} A_{FF}\vec{c}_{F,F} &= \vec{b}_F - (A_{FF}\vec{c}_{D,F} + A_{FD}\vec{c}_{D,D}) \\ &= \vec{b}_F - (A\vec{c}_D)_F\,. \end{aligned} \tag{2.22}$$

The solution of this equation can be obtained by utilizing the methods for inverting the matrix A_{FF} on the free degrees of freedom provided by NGSolve. This inversion can be performed very efficiently since K and M display a great sparsity character due their element-wise definition of the basis functions and their property Eq. (2.10). The full solution coefficient vector is given by the solution on the free degrees of freedom to which the prescribed Dirichlet data has to be added:

$$\vec{c} = \begin{pmatrix} A_{FF}^{-1} & 0 \\ 0 & 0 \end{pmatrix} (\vec{b} - A\vec{c}_D) + \vec{c}_D\,. \tag{2.23}$$

To finally obtain the full discretized solution, these coefficients have to be inserted back into $\psi_h = \sum_j c_j\, \varphi_j$.

Having derived the solution strategy for the scalar Helmholtz equation in a very general setting, we now apply it to the two-dimensional, two-port waveguide with metallic boundaries that has been introduced in the preceding section. An example mesh of such a system can be seen in Fig. 2.2, where we typically use three vertices

---

[5] Since the discretization is performed internally in NGSolve, its syntax allows to set up these quantities via their corresponding continuous expressions [see Eq. (2.8)].

[6] See also the NGSolve documentation at https://docu.ngsolve.org.

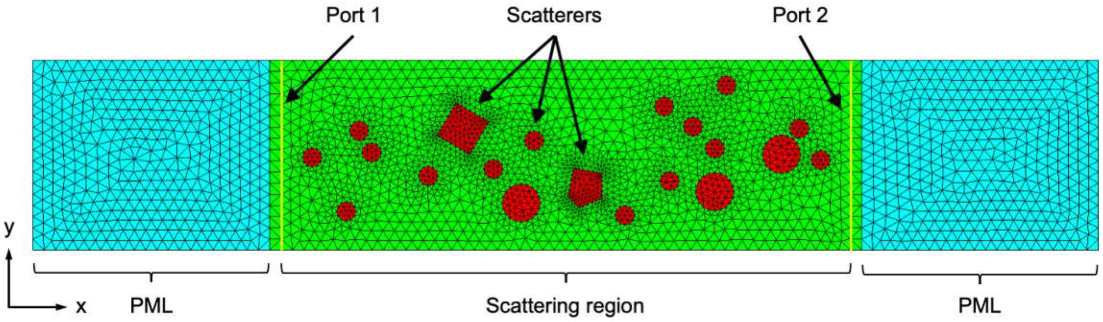

Figure 2.2: Mesh of a generic 2D waveguide system consisting of a scattering region (green), which is attached to perfectly matched layers (PMLs, cyan) on both ends which absorb all outgoing waves. Moreover, the scattering region is filled with scatterers (red) of different shapes and sizes whose mesh is finer due a refinement based on their refractive index which we chose here to be 2. Metallic scatterers are cut out of the mesh (not shown) since they are modeled via homogeneous Dirichlet boundary conditions on their surface making internal degrees of freedom unnecessary. Also note that the boundaries of the scatterers are curved due to the usage of third order curvilinear elements. The left and right interfaces next to the PML interface are the waveguide ports, on which source terms [Eqs. (2.28) and (2.29)] are defined. Homogeneous Dirichlet boundary conditions [Eq. (2.24)] are further imposed on the outer rectangular boundary.

per half wavelength, a polynomial order[7] of $n_p = 5$ and curvilinear elements of order $n_c = 3$. The metallic boundaries are modeled by a PEC boundary condition which demands a vanishing tangential component of the vectorial electric field in the stationary 3D case. Since in 2D the scalar field is transversely polarized in the z-direction, the PEC boundary condition translates into a homogeneous Dirichlet boundary condition at the borders of the waveguide, i.e.,

$$\psi = 0 \quad \text{on } \Gamma_D = \partial\Omega \,. \tag{2.24}$$

These are easily implementable since Eq. (2.23) has to be solved with $\vec{c}_D = 0$, i.e., only A_{FF} has to be inverted on the free degrees of freedom. Moreover, Neumann boundaries are absent in our system, further simplifying Eq. (2.18). Note that setting no boundary conditions in the FEM is equivalent to using homogeneous natural boundary conditions since not including a Neumann term in Eq. (2.18) is equivalent to setting $g_N = 0$.

---

[7] Please note that NGSolve does not use only nodal basis functions for $n_p > 1$. Instead, it uses a combination of standard first-order polynomials as vertex basis functions and the hierarchical basis of integrated Legendre and Jacobi polynomials as edge and cell basis functions, respectively [75]. The vertex functions are 1 in the defining vertex and 0 on all the other vertices, where the edge and cell functions vanish at the mesh vertices and edges, respectively, thus only being greater zero on the edges between two vertices or inside a triangle. These hierarchical bases have the advantage that the basis functions of order n_p can be obtained via an integration of the basis functions of order $n_p - 1$ thus being computationally very efficient. It is also worth noting that the basis functions within each set of vertex, edge or cell functions are orthogonal, but functions from different sets are not.

Since we are interested in waveguides with semi-infinite leads (rather than closed cavities), the latter have to be terminated and an absorbing layer has to be introduced to prevent the wave from being scattered back into the system. For this purpose, we use specially tailored materials called *perfectly matched layers (PMLs)*, which exponentially attenuate the outgoing waves without introducing any reflections. PMLs can be realized via a complex permittivity $\varepsilon(\vec{r}\,)$ and permeability $\mu(\vec{r}\,)$ in Maxwell's equations, where an equivalent and more elegant way of implementing them is given by a complex coordinate stretching of the form [80]

$$x \;\rightarrow\; \tilde{x} = x + \frac{i}{\omega}\int_0^x \sigma(x')\,dx'\,, \tag{2.25}$$

$$\frac{\partial}{\partial x} \;\rightarrow\; \frac{\partial}{\partial \tilde{x}} = \frac{1}{1+\frac{i}{\omega}\sigma(x)}\frac{\partial}{\partial x}\,. \tag{2.26}$$

Here, $\sigma(x)$ is the chosen PML absorption profile which is greater than zero only in the PML region. Considering a transverse waveguide mode propagating inside the PML along the longitudinal x-direction with

$$e^{ik_x\tilde{x}} = e^{ik_x x}e^{-c(k_x/k)\int_0^x \sigma(x')\,dx'} \tag{2.27}$$

and $\omega = kc$, we see that Eq. (2.25) causes the desired exponential damping inside the PML. Outside the PML, $\sigma(x) = 0$ and thus the solution remains unchanged causing no reflections at the PML interface[8]. For plane waves in 1D, the division by ω in Eq. (2.25) gives rise to a frequency-independent attenuation in homogeneous materials (neglecting material dispersion), whereas in higher dimensions the different propagation angles of waveguide modes characterized by the ratio k_x/k causes an angle- and thus mode-dependent absorption. This effect becomes especially important at mode openings at which the longitudinal propagation constant k_x of the new mode is very small and its absorption thus very inefficient. Therefore, an automatic scaling of the PML length slightly above mode-openings has been implemented. A similar scaling has also been applied slightly below mode openings in order to ensure a sufficient decay of evanescent modes that can be excited at scatterers close to the PML. It's worth noting, that the complex scaling in Eq. (2.25) adds an oscillating part to evanescent waves, but does not increase their decay rate [80]. Also note that if the wave is fully absorbed before reaching the end of the PML, the choice of the boundary condition is irrelevant such that we can impose homogeneous Dirichlet boundary conditions [Eq. (2.24)] at the PML ends. PMLs for stationary problems are already provided by NGSolve and their default implementation corresponds to an additional complex transformation of the form $\xi \to \xi + \alpha_{\mathrm{PML}}\xi$, which is applied to all elements in the PML region. Here, ξ is the generalized distance to the beginning of the PML and α_{PML} is the complex parameter of the linear scaling which we typically set to $\alpha_{\mathrm{PML}} = 2i$.

---

[8] This is only true analytically since the discretization together with the finite truncation in the numerical simulations again introduce reflections. However, these are usually very small and therefore negligible.

Last, we inject waves into the system by utilizing the source term in Eq. (2.1). Here it is important to note that the amplitude of the source differs from the amplitude of the actual excitation in the waveguide (an exact analytical expression of their relation is derived in Appendix B). Summarizing, for injecting a certain superposition of flux-normalized waveguide modes characterized by the coefficient vector $\vec{a}$ into the system, the corresponding source terms read

$$f_{\text{port 1}} = \sum_{n=1}^{N} -2ik_{x,n}\, a_n\, \tilde{\chi}_n(y)\,, \tag{2.28}$$

$$f_{\text{port 2}} = \sum_{n=1}^{N} -2ik_{x,n}\, a_n\, \tilde{\chi}_n^*(y)\,. \tag{2.29}$$

Here, N is the total number of propagating modes, $k_{x,n} = \sqrt{k^2 - k_{y,n}^2}$ are their longitudinal propagation constants and $\tilde{\chi}_n(y) = \chi_n(y)/\sqrt{k_{x,n}}$ are the flux-normalized transverse profiles of the TE modes Eq. (1.37). Note that these transverse profiles do not contain longitudinal phase factors $e^{ik_{x,n}x_p}$, where x_p is the longitudinal position of the respective port, since the use of shifted basis functions makes them vanish (see Section 1.3). Such source terms are then defined on the waveguide ports in order to excite waves with amplitudes a_n incident from the left and/or right. Note that the complex conjugation in the source term at port 2 is not relevant in the considered waveguide case as the basis functions are purely real. However, we also implemented the periodic boundary conditions provided by NGSolve for which the basis functions are plane waves, i.e., complex-valued exponentials. In this case, left-traveling waves have to be complex conjugated, which also has to be considered in the calculation of the transmission and reflection matrix elements below.

Now that we have all the ingredients to solve the Helmholtz equation numerically, we aim to calculate the scattering matrix. For this purpose, we inject the individual flux normalized modes $\tilde{\chi}_n$ at port 1 and calculate the corresponding solution in the whole waveguide $\tilde{\psi}_n$. Next, we project the transmitted part of the solution, i.e., $\tilde{\psi}_n$ at port 2 ($x = L$), and the reflected part, i.e., $\tilde{\psi}_n - \tilde{\chi}_n$ at port 1 ($x = 0$), onto all modes and normalize each overlap integral by the intensity of the mode onto which we project. The resulting transmission and reflection matrix elements thus read[9]

$$\begin{aligned} t_{mn} &= \frac{\int_{\text{port 2}} \tilde{\chi}_m^* \, \tilde{\psi}_n \, dy}{\int_{\text{port 2}} |\tilde{\chi}_m|^2 \, dy} \\ &= \sqrt{\frac{k_{x,m}}{k_{x,n}}} \int_{\text{port 2}} \chi_m^* \, \psi_n \, dy \, , \end{aligned} \tag{2.30}$$

$$\begin{aligned} r_{mn} &= \frac{\int_{\text{port 1}} \tilde{\chi}_m \, (\tilde{\psi}_n - \tilde{\chi}_n) \, dy}{\int_{\text{port 1}} |\tilde{\chi}_m|^2 \, dy} \\ &= \sqrt{\frac{k_{x,m}}{k_{x,n}}} \int_{\text{port 1}} \chi_m \, (\psi_n - \chi_n) \, dy \, , \end{aligned} \tag{2.31}$$

respectively. Here, the second equal sign was obtained by pulling the flux-factors of all flux-normalized quantities (denoted by a tilde) in front of the integral. Moreover, we have used the imposed intensity normalization $\int_{\text{port}} |\chi_m(y)|^2 \, dy = 1$ leaving us with expressions valid for non-flux-normalized input states[10] $\tilde{\chi}_n(y) \to \chi_n(y)$ in Eqs. (2.28) and (2.29). In analogy to Eqs. (2.30) and (2.31), one can define the transmission and reflection matrix elements for an input from port 2 as

$$\begin{aligned} t'_{mn} &= \frac{\int_{\text{port 1}} \tilde{\chi}_m \, \tilde{\psi}_n \, dy}{\int_{\text{port 1}} |\tilde{\chi}_m|^2 \, dy} \\ &= \sqrt{\frac{k_{x,m}}{k_{x,n}}} \int_{\text{port 1}} \chi_m \, \psi_n \, dy \, , \end{aligned} \tag{2.32}$$

$$\begin{aligned} r'_{mn} &= \frac{\int_{\text{port 2}} \tilde{\chi}_m^* \, (\tilde{\psi}_n - \tilde{\chi}_n^*) \, dy}{\int_{\text{port 2}} |\tilde{\chi}_m|^2 \, dy} \\ &= \sqrt{\frac{k_{x,m}}{k_{x,n}}} \int_{\text{port 2}} \chi_m^* \, (\psi_n - \chi_n^*) \, dy \, . \end{aligned} \tag{2.33}$$

Finally, the scattering matrix is given by Eq. (1.4). Last, we check the numerically calculated scattering matrix by verifying its required symmetries Eqs. (1.2) and (1.9) as illustrated in Fig. 2.3.

Since scalar scattering in 2D cannot always capture all the physics contained in Maxwell's equations, we therefore continue in the following section with the numerical solution of the full 3D problem.

---

[9] These expressions are similar to the Fisher-Lee relations derived for the Schrödinger equation [81, 82]. However, here we do not have direct access to the Green's function, but only to the full solution which is given by the integral of the input state times the Green's function.

[10] In this case, the flux normalization has to be applied manually via the prefactor in front of the integrals in Eqs. (2.30) and (2.31), which is very similar to quantum mechanical scattering theory, where the scattering problem gets often solved without flux normalization.

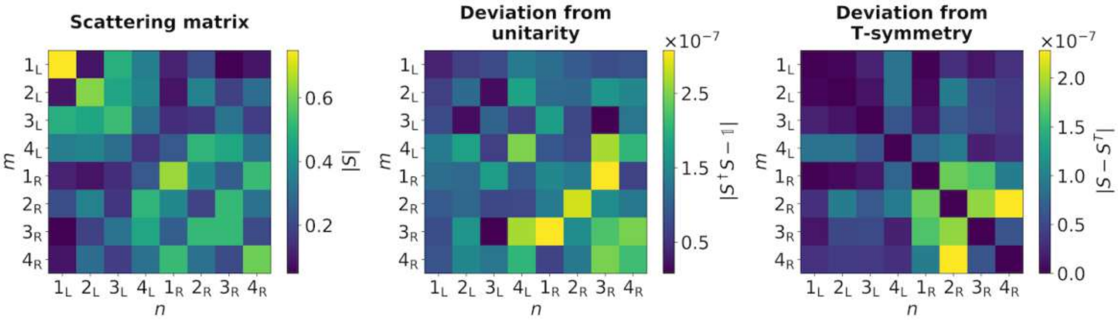

Figure 2.3: Numerically calculated scattering matrix of the system shown in Fig. 2.2 for 4 propagating TE_{m0} modes. The left plot shows the absolute value of the scattering matrix elements while the middle and right plot shows the deviation of the scattering matrix from unitarity and transposition symmetry, respectively. The subscripts L/R indicate the input from the left/right waveguide port 1/port 2.

2.2 Stationary scattering in 3D waveguides

While in many cases a scalar 2D description of a scattering process might be sufficient, a refractive index distribution depending on all three spatial dimensions together with strong scattering will inevitably lead to polarization mixing which cannot be described by the scalar Helmholtz equation. In the following, we therefore present the numerical solution of the full-vectorial 3D problem. As in the scalar 2D case, we are interested in time-harmonic problems, in which case Maxwell's equations can be reduced to the so-called vector Helmholtz equation which reads ($\mu_r = 1$, see Appendix A for details about its derivation), together with corresponding boundary conditions, as follows:

$$\vec{\nabla} \times \vec{\nabla} \times \vec{E}(\vec{r}) - n^2(\vec{r})k^2\vec{E}(\vec{r}) = \vec{f}(\vec{r}) \quad \text{in } \Omega\,, \tag{2.34}$$

$$\vec{E}(\vec{r}) \times \vec{n} = \vec{g}_D(\vec{r}) \quad \text{on } \Gamma_D\,, \tag{2.35}$$

$$\left[\vec{\nabla} \times \vec{E}(\vec{r})\right] \times \vec{n} = \vec{g}_N(\vec{r}) \quad \text{on } \Gamma_N\,. \tag{2.36}$$

Here, $\vec{E}(\vec{r})$ is the unknown vectorial electric field, $\vec{r} = (x, y, z)^T$ is the position vector, $\vec{f}(\vec{r})$ is the vectorial source term and $\vec{n}$ is the outer normal vector. The essential boundary condition corresponds to the tangential component of the electric field, whereas the natural boundary condition (naturally appearing in the weak form below) is related to a 90 degree rotation of the magnetic field since $\vec{\nabla} \times \vec{E} \propto \vec{H}$. The mixed or Robin boundary condition can be written as

$$\left[\vec{\nabla} \times \vec{E}(\vec{r})\right] \times \vec{n} + \eta\,\vec{E}(\vec{r}) \times \vec{n} = \vec{g}_R(\vec{r}) \quad \text{on } \Gamma_R\,, \tag{2.37}$$

where the Dirichlet part, i.e., $\vec{E}(\vec{r}) \times \vec{n}$ on Γ_R, must be again introduced as an additional unknown in the weak formulation.

Multiplying Eq. (2.34) with a vectorial test function $\vec{v}$, integrating over the whole domain and applying the integration by parts formula [79]

$$\int_\Omega (\vec{\nabla} \times \vec{u}) \cdot \vec{v}\, d\Omega = \int_\Omega \vec{u} \cdot (\vec{\nabla} \times \vec{v})\, d\Omega - \int_\Gamma (\vec{u} \times \vec{n}) \cdot \vec{v}\, d\Gamma \tag{2.38}$$

with $\vec{u} = \vec{\nabla} \times \vec{E}$ yields

$$\begin{aligned} \int_\Omega (\vec{\nabla} \times \vec{E}) \cdot (\vec{\nabla} \times \vec{v})\, d\Omega - \int_\Omega n^2 k^2\, \vec{E} \cdot \vec{v}\, d\Omega = \int_\Omega \vec{f} \cdot \vec{v}\, d\Omega \\ + \int_{\Gamma_N} \vec{g}_N \cdot \vec{v}\, d\Gamma + \int_{\Gamma_D} [(\vec{\nabla} \times \vec{E}) \times \vec{n}] \cdot \vec{v}\, d\Gamma\,. \end{aligned} \tag{2.39}$$

Since the last integral is unknown, we rewrite it as

$$\int_{\Gamma_D} [(\vec{\nabla} \times \vec{E}) \times \vec{n}] \cdot \vec{v}\, d\Gamma = - \int_{\Gamma_D} (\vec{v} \times \vec{n}) \cdot (\vec{\nabla} \times \vec{E})\, d\Gamma \tag{2.40}$$

and demand – similar to $v = 0$ on Γ_D in the scalar case – that $\vec{v} \times \vec{n} = 0$ on Γ_D [79] such that the integral vanishes. Thus, the resulting so-called *curl-curl problem* is given by

$$\int_\Omega (\vec{\nabla} \times \vec{E}) \cdot (\vec{\nabla} \times \vec{v})\, d\Omega - \int_\Omega n^2 k^2\, \vec{E} \cdot \vec{v}\, d\Omega = \int_\Omega \vec{f} \cdot \vec{v}\, d\Omega + \int_{\Gamma_N} \vec{g}_N \cdot \vec{v}\, d\Gamma\,. \tag{2.41}$$

Next, the above equation has to be discretized by introducing vectorial basis functions. As it turns out, however, the nodal basis functions briefly introduced in the previous section are not very well suited for describing electromagnetic problems since they force all field components to be continuous (shared nodes between two elements feature the same values). The interface conditions derived from Maxwell's equations, however, only demand the continuity of the tangential $\vec{E}$-field at material interfaces while its normal component can be discontinuous. Moreover, using a nodal basis also makes it difficult to obtain a scalar degree of freedom on each node due to the vectorial nature of the electric field. Therefore, so-called edge-based *vector elements*[11] (also known as Whitney forms, Nédélec or Bossavit elements) have been introduced, whose degrees of freedom are only associated with the tangential component of the field on the corresponding edge [76, 84–86]. Thus, tangential continuity, as required by Maxwell's interface conditions, can be easily imposed, while leaving the normal component free to jump across material interfaces. In fact, such elements give rise to a better description of electromagnetic eigenvalue problems. In particular, they drastically reduce the number of spurious modes,

---

[11] In computational electromagnetics, the term "element" often refers to the basis functions rather than to the mathematical definition of the element like, e.g., a tetrahedron, together with a polynomial space defined on it [83].

Die approbierte gedruckte Originalversion dieser Dissertation ist an der TU Wien Bibliothek verfügbar.
The approved original version of this doctoral thesis is available in print at TU Wien Bibliothek.
TU Bibliothek WIEN Your knowledge hub

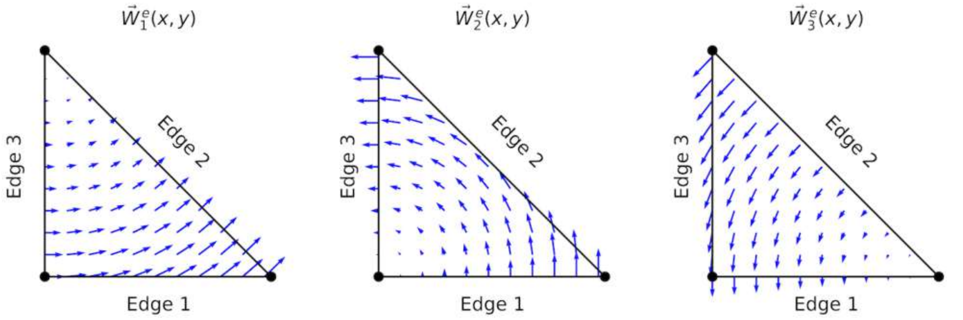

Figure 2.4: Edge-based vector elements of lowest order [Eqs. (2.42)-(2.44)] on the reference triangle in two dimensions which only have a non-vanishing and constant tangential component on their defined edge.

which do not satisfy the divergence constraints of Maxwell's equations [76, 85] and which thus cannot be excited by the driven vector Helmholtz equation (2.34) considered here. Moreover, the relaxed continuity conditions of these elements allow a better description at sharp edges due to the absence of a nodal value at the electric field singularity [85].

To get a better understanding of these elements, Fig. 2.4 shows the lowest order edge-based vector elements on a reference triangle in two dimensions, whose analytical expressions are given by [76]

$$\vec{W}_1^e = \varphi_1 \vec{\nabla}\varphi_2 - \varphi_2 \vec{\nabla}\varphi_1 \,, \tag{2.42}$$

$$\vec{W}_2^e = \varphi_2 \vec{\nabla}\varphi_3 - \varphi_3 \vec{\nabla}\varphi_2 \,, \tag{2.43}$$

$$\vec{W}_3^e = \varphi_3 \vec{\nabla}\varphi_1 - \varphi_1 \vec{\nabla}\varphi_3 \,. \tag{2.44}$$

It can be easily shown that $\vec{t}_i \cdot \vec{W}_i^e = 1/\ell_i^e$ with $\vec{t}_i$ being the tangential vector of the i-th edge and ℓ_i^e being its length. This means that each of these elements has a constant tangential component on the associated edge which is inversely proportional to its length and thus one typically normalizes them by using [77]

$$\vec{N}_i^e = \ell_i^e \vec{W}_i^e \,. \tag{2.45}$$

These basis functions can further be easily generalized to a reference tetrahedron in three dimensions by adding the 3 basis functions defined on the edges that connect the base triangle with the top of the tetrahedron [76, 85]. As can be seen, each of these edge elements[12] has a non-vanishing (and constant) tangential component on its associated edge, whereas its tangential component vanishes on all the other edges. Most importantly, the above definition and properties of the considered elements are not only valid on the right-angled reference triangle, but can be mapped to any triangle [76]. Lastly, we want to emphasize that these elements are also called curl-conforming since the electric field expanded in such elements has a curl that is square-integrable. More precisely, this so-called $H(\mathrm{curl};\Omega)$ function space is defined as

---

[12] The first order vector elements discussed here are exclusively defined via degrees of freedom on the edges which has caused the term edge elements. In case of higher order basis functions, one gets additional degrees of freedom inside the element and therefore one then usually speaks of edge-based vector elements [76].

$$H(\mathrm{curl};\Omega) = \{\vec{E} \in [L_2(\Omega)]^3 : \mathrm{curl}\,\vec{E} \in [L_2(\Omega)]^3\}\,. \tag{2.46}$$

In the discretized formulation of the FEM, this translates into piecewise continuous vector-valued polynomials featuring tangential continuity – just like the above defined $\vec{N}_i^e$.

For simplicity, we now continue the discussion with these edge-based vector elements of lowest order and write the discretized solution as

$$\vec{E}_h = \sum_{j\,\in\,\Omega_F} c_{F,j}\,\vec{N}_j^e + \sum_{j\,\in\,\Gamma_D} g_{D,j}\,\vec{N}_j^e\,, \tag{2.47}$$

where we have again split the solution into the free degrees of freedom $c_{F,j}$ and the prescribed Dirichlet data $g_{D,j}$. Next, applying the Galerking method, i.e., using $\vec{v}_{h,i} = \vec{N}_i^e$, yields the discretized weak form of the vector Helmholtz equation

$$\begin{aligned}
&\sum_{j\,\in\,\Omega_F}\left(\int_\Omega (\vec{\nabla}\times\vec{N}_j^e)\cdot(\vec{\nabla}\times\vec{N}_i^e)\,d\Omega - \int_\Omega n^2k^2\,\vec{N}_j^e\cdot\vec{N}_i^e\,d\Omega\right)c_{F,j}\\
&\qquad = \int_\Omega \vec{f}\cdot\vec{N}_i^e\,d\Omega + \int_{\Gamma_N}\vec{g}_N\cdot\vec{N}_i^e\,d\Gamma \qquad\qquad (2.48)\\
&\qquad\quad - \sum_{j\,\in\,\Gamma_D}\left(\int_\Omega (\vec{\nabla}\times\vec{N}_j^e)\cdot(\vec{\nabla}\times\vec{N}_i^e)\,d\Omega - \int_{\Omega_F} n^2k^2\,\vec{N}_j^e\cdot\vec{N}_i^e\,d\Omega\right)g_{D,j}\,.
\end{aligned}$$

The elements of the stiffness and modified mass matrix in the considered vectorial case are

$$K_{ij} = \int_\Omega (\vec{\nabla}\times\vec{N}_j^e)\cdot(\vec{\nabla}\times\vec{N}_i^e)\,d\Omega\,, \tag{2.49}$$

$$M_{ij} = -\int_\Omega n^2k^2\,\vec{N}_j^e\cdot\vec{N}_i^e\,d\Omega\,, \tag{2.50}$$

and the first two integrals on the right-hand side of Eq. (2.48) can again be written as a vector $\vec{b}$ with elements

$$b_i = \int_\Omega \vec{f}\cdot\vec{N}_i^e\,d\Omega + \int_{\Gamma_N}\vec{g}_N\cdot\vec{N}_i^e\,d\Gamma\,. \tag{2.51}$$

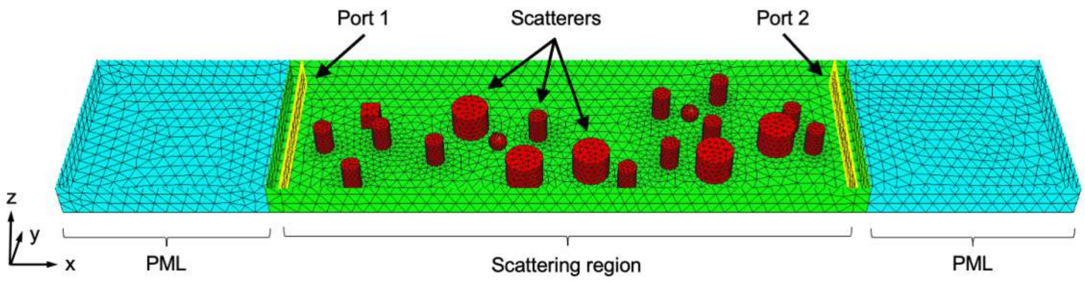

Figure 2.5: Cut through the mesh of a generic 3D waveguide system (only surfaces are shown) consisting of a scattering region (green), which is attached to PMLs (cyan) on both ends which absorb all outgoing waves. Moreover, the scattering region is filled with scatterers (red) of different sizes and shapes, where metallic scatterers are cut out of the mesh (not shown) since the imposed homogeneous Dirichlet boundary conditions make internal degrees of freedom unnecessary. Like in 2D, the boundaries of the scatterers are curved due to the usage of third order curvilinear elements. The planes next to the PML interfaces are the waveguide ports (marked by the yellow lines), on which source terms [Eqs. (2.54) and (2.55)] are defined. Homogeneous Dirichlet boundary conditions [Eq. (2.53)] are further imposed on the whole outer cuboid boundary.

Again, the assembly of the quantities in Eq. (2.49)-(2.51) is provided by NGSolve and together with the definition $A = K + M$, Eq. (2.48) becomes

$$\sum_{j\,\in\,\Omega_F} A_{ij}\, c_{F,j} = b_i - \sum_{j\,\in\,\Gamma_D} A_{ij}\, g_{D,j}\,. \tag{2.52}$$

Similar to the scalar 2D case, we can then extend the Dirichlet data $g_{D,j}$ defined on Γ_D into the whole domain resulting in the coefficients $c_{D,j} \in \Omega$. Finally, following the steps in Eqs. (2.20)-(2.23), we obtain the solution coefficient vector $\vec{c} = \vec{c}_F + \vec{c}_D$ as a sum of the solution on the free degrees of freedom and the Dirichlet data.

Having again a very general solution strategy for the vectorial problem at hand, we now specify the system and the parameters in use. The system under consideration is given by a rectangular, metallic two-port waveguide, where Fig. 2.5 shows a generic mesh of such. We typically use three vertices per half wavelength and curvilinear elements of order $n_c = 3$. NGSolve supports Nédélec elements of arbitrary order which we typically choose to be $n_p \geq 3$. The PEC boundary condition demands a vanishing tangential field at the waveguide walls which translates into a homogeneous Dirichlet boundary condition

$$\vec{E} \times \vec{n} = 0 \quad \text{on } \Gamma_D = \partial\Omega \tag{2.53}$$

that can be easily implemented by using $\vec{c}_D = 0$ and inverting A_{FF} on the free degrees of freedom. Natural boundary conditions are again absent in our problem letting the second term in Eq. (2.51) vanish.

Die approbierte gedruckte Originalversion dieser Dissertation ist an der TU Wien Bibliothek verfügbar.
The approved original version of this doctoral thesis is available in print at TU Wien Bibliothek.
TU Bibliothek WIEN Your knowledge hub

To absorb the waves at both ends of the scattering region, the PMLs provided by NGSolve are again used with a complex scaling parameter of $\alpha_{\mathrm{PML}} = 2i$. Similar to the scalar 2D case, their length is increased automatically close to mode openings to ensure full absorption and sufficient decay of all propagating and evanescent waveguide modes at the PML ends, respectively.

To inject a certain superposition of waveguide modes characterized by a coefficient vector $\vec{a}$ into the system, we use source terms which are structurally identical to the scalar case, but now contain the full-vectorial form of the TE_{mn} modes:

$$\vec{f}_{\mathrm{port}\ 1} = \sum_{n=1}^{N} -2ik_{x,n}\, a_n\, \tilde{\vec{E}}_n^{\mathrm{TE}}(y,z)\,, \tag{2.54}$$

$$\vec{f}_{\mathrm{port}\ 2} = \sum_{n=1}^{N} -2ik_{x,n}\, a_n\, \tilde{\vec{E}}_n^{\mathrm{TE}\,*}(y,z)\,. \tag{2.55}$$

Here, the indices of all propagating TE-modes have been mapped to a single index, i.e., $(m,n) \to n$, and a tilde denotes again flux-normalized quantities.

The transmission and reflection matrices can then be calculated similarly to the previous section, but with the scalar quantities replaced by the vectorial fields. Assuming flux-normalized input states in Eq. (2.54), the transmission and reflection matrix elements for an input from port 1 read

$$\begin{aligned} t_{mn} &= \frac{\iint_{\mathrm{port}\ 2} \tilde{\vec{E}}_m^{\mathrm{TE}\,*} \cdot \tilde{\vec{E}}_n \, dy\, dz}{\iint_{\mathrm{port}\ 2} |\tilde{\vec{E}}_m^{\mathrm{TE}}|^2 \, dy\, dz} \\ &= \sqrt{\frac{k_{x,m}}{k_{x,n}}} \iint_{\mathrm{port}\ 2} \vec{E}_m^{\mathrm{TE}\,*} \cdot \vec{E}_n \, dy\, dz\,, \end{aligned} \tag{2.56}$$

$$\begin{aligned} r_{mn} &= \frac{\iint_{\mathrm{port}\ 1} \tilde{\vec{E}}_m^{\mathrm{TE}} \cdot (\tilde{\vec{E}}_n - \tilde{\vec{E}}_n^{\mathrm{TE}}) \, dy\, dz}{\iint_{\mathrm{port}\ 1} |\tilde{\vec{E}}_m^{\mathrm{TE}}|^2 \, dy\, dz} \\ &= \sqrt{\frac{k_{x,m}}{k_{x,n}}} \iint_{\mathrm{port}\ 1} \vec{E}_m^{\mathrm{TE}} \cdot (\vec{E}_n - \vec{E}_n^{\mathrm{TE}}) \, dy\, dz\,, \end{aligned} \tag{2.57}$$

respectively. The corresponding matrix elements for an input from port 2 are

$$\begin{aligned} t'_{mn} &= \frac{\iint_{\text{port 1}} \tilde{\vec{E}}_m^{\text{TE}} \cdot \tilde{\vec{E}}_n \, dy\, dz}{\iint_{\text{port 1}} |\tilde{\vec{E}}_m^{\text{TE}}|^2 \, dy\, dz} \\ &= \sqrt{\frac{k_{x,m}}{k_{x,n}}} \iint_{\text{port 1}} \vec{E}_m^{\text{TE}} \cdot \vec{E}_n \, dy\, dz \,, \end{aligned} \tag{2.58}$$

$$\begin{aligned} r'_{mn} &= \frac{\iint_{\text{port 2}} \tilde{\vec{E}}_m^{\text{TE}\,*} \cdot (\tilde{\vec{E}}_n - \tilde{\vec{E}}_n^{\text{TE}\,*}) \, dy\, dz}{\iint_{\text{port 2}} |\tilde{\vec{E}}_m^{\text{TE}}|^2 \, dy\, dz} \\ &= \sqrt{\frac{k_{x,m}}{k_{x,n}}} \iint_{\text{port 2}} \vec{E}_m^{\text{TE}\,*} \cdot (\vec{E}_n - \vec{E}_n^{\text{TE}\,*}) \, dy\, dz \,. \end{aligned} \tag{2.59}$$

Using Eqs. (2.56)-(2.59) does not yet result in a unitary scattering matrix, since TE_{mn} modes with $m \geq 1$ and $n \geq 1$ can scatter into energetically degenerate TM_{mn} modes. We therefore also have to project onto such outgoing TM_{mn} modes if $m \geq 1$ and $n \geq 1$ (otherwise these modes do not exist), which results in rectangular matrices that finally satisfy $S^\dagger S = \mathbb{1}$. As can be seen in Fig. 1.3, TM modes feature transverse as well as longitudinal electric field components, with the latter being neglected when performing surface integrals in an $H(\text{curl}; \Omega)$-conforming function space[13]. To calculate the overlap integrals correctly, we either read-out the solution on the respective waveguide port and perform the integration manually or interpolate the full solution onto a vector $H^1(\Omega)$-conforming space of continuous functions and use the built-in integration function provided by NGSolve. As in the previous section, we also validate the symmetries Eqs. (1.2) and (1.9) of the numerically calculated scattering matrix in Fig. 2.6.

The neglection of normal components on surfaces further prevents the solution for TM modes in the $\vec{E}$-field formulation. However, the developed code can be easily adapted to the solution of the vector Helmholtz equation in the $\vec{H}$-field formulation in which the TM modes are exclusively transverse. In this formulation, the PEC boundary condition Eq. (2.53) corresponds to a homogeneous natural boundary condition for the $\vec{H}$-field due to Maxwell's equation (1.35). Moreover, the interface condition in Eq. (A.6) implies that the $H(\text{div})$-conforming finite element space

$$H(\text{div}; \Omega) = \{\vec{E} \in [L_2(\Omega)]^3 : \text{div}\, \vec{E} \in L_2(\Omega)\} \tag{2.60}$$

spanned by normally-continuous face elements has to be employed [83].

---

[13] On material interfaces, normal components of the electric field are not continuous and thus not well defined. However, in mathematical terms, the so-called trace operator [79] has to be continuous across boundaries and thus only the tangential trace is taken into account, even though there are no material interfaces like, e.g., on the waveguide ports.

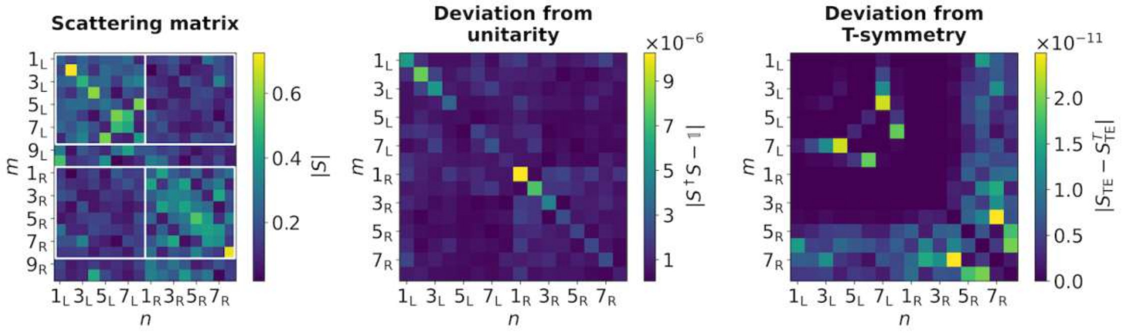

Figure 2.6: Numerically calculated scattering matrix of the system shown in Fig. 2.5 for 8 propagating input TE modes which can additionally scatter into 2 outgoing TM modes (row 9, 10). The $\vec{E}$-field intensities of the modes used in this calculation are depicted in Fig. 1.3. The left plot shows the absolute value of the scattering matrix elements, where the white frames mark the submatrices for in- and outgoing TE modes. The middle plot shows the deviation of the full rectangular scattering matrix from unitarity and the right plots shows the deviation of the TE scattering matrix from transposition symmetry. The subscripts L/R again indicate the input from the left/right waveguide port 1/port 2.

Part II.

Applications and results

Chapter 3

Optimal wave fields for micromanipulation[14]

3.1 The generalized Wigner-Smith operator

The concept of Wigner-Smith time-delay has triggered an entire field of research and has led to numerous insights and discoveries in the field of complex wave scattering. Most notably, it enables the creation of wavefronts which feature a well-defined propagation time through a complex scattering system only based on the knowledge of the system's scattering matrix. In this chapter, we push the concept further and generalize it to a whole new class of operators which we term *generalized Wigner-Smith (GWS)* operators whose eigenstates are optimal for micromanipulation tasks since they – as we show in the following – transfer well-defined amounts of physical quantities to a target. To generalize the Wigner-Smith operator, we replace the frequency derivative with a derivative with respect to an arbitrary parameter, i.e., $\omega \to \theta$. The resulting operator then reads

$$Q_\theta^{(S)} = -iS^\dagger(\theta)\frac{dS(\theta)}{d\theta}\,, \tag{3.1}$$

where θ can now be any parameter on which the scattering matrix depends. Irrespective of the chosen parameter θ, the output wavefronts of the eigenstates of $Q_\theta^{(S)}$ for a unitary scattering matrix ($S^\dagger = S^{-1}$) are by construction invariant with respect to a small change in θ – just like the principal modes are invariant with respect to a change in ω to first order [40]. To associate physical meaning to the eigenvalues τ_θ of $Q_\theta^{(S)}$, we use the fact that the eigenvalues of $Q_\omega^{(S)}$ are proper time-delays [37]. More precisely, the frequency derivative in $Q_\omega^{(S)}$ gives rise to eigenvalues which are associated to the conjugate quantity (in the sense of a Fourier relation), i.e., the time. Analogously, the eigenvalues of the operator $Q_\theta^{(S)}$, which involves a derivative of the scattering matrix by θ, have to be associated with the quantity conjugate to θ. To illustrate this correspondence, we can write the shifted scattering matrix $S(\theta+\Delta\theta)$ with the help of a generalized "translation operator" $e^{iC_\theta\Delta\theta}$ as [56, 87]

---

[14] The results presented in this chapter were obtained in collaboration with my former colleagues Philipp Ambichl and Andre Brandstötter, my current colleagues Michael Horodynski and Kevin Pichler, our experimental collaborators Ulrich Kuhl and his former PhD student Julian Böhm from the Université Côte d'Azur and Yan V. Fyodorov from King's College in London. The theoretical analysis was carried out by Philipp Ambichl, Michael Horodynski, myself and Andre Brandstötter under the supervision of Stefan Rotter. The numerical simulations were mainly performed by myself, whereas the experiments were conducted by Julian Böhm and Kevin Pichler under the supervision of Ulrich Kuhl. The presented results are based on two joint publications [55, 56] from which parts of the text and figures have been taken.

$$S(\theta+\Delta\theta) = e^{-iC_\theta\Delta\theta} S(\theta) e^{iC_\theta\Delta\theta}\,, \tag{3.2}$$

with C_θ being the conjugate operator to θ. In case of very small $\Delta\theta$, Taylor-expanding the translation operators gives

$$\begin{aligned} S(\theta+\Delta\theta) &= \left[\mathbb{1} - iC_\theta\Delta\theta + \mathcal{O}(\Delta\theta^2)\right] S(\theta) \left[\mathbb{1} + iC_\theta\Delta\theta + \mathcal{O}(\Delta\theta^2)\right] \\ &\approx S(\theta) - iC_\theta S(\theta)\Delta\theta + iS(\theta)C_\theta\Delta\theta\,, \end{aligned} \tag{3.3}$$

where we neglected terms of the order $(\Delta\theta)^n$ with $n \geq 2$ in the second line. The derivative of S with respect to θ appearing in Eq. (3.1) can then be expressed as

$$\frac{dS}{d\theta} = \lim_{\Delta\theta\to 0} \frac{S(\theta+\Delta\theta) - S(\theta)}{\Delta\theta} = iS(\theta)C_\theta - iC_\theta S(\theta)\,. \tag{3.4}$$

Making use of the assumed unitarity of the scattering matrix $S^\dagger S = \mathbb{1}$, $Q_\theta^{(S)}$ can finally be written as

$$Q_\theta^{(S)} = -iS^\dagger \frac{dS}{d\theta} = C_\theta - S^\dagger C_\theta S\,. \tag{3.5}$$

Choosing θ as, e.g., the spatial shift of the system in a certain direction with unit vector $\hat{n}$, the corresponding conjugate operator is given by the momentum operator in shifting direction, i.e., $C_\theta = \vec{k}\cdot\hat{n}$. In this case, the expectation value of the GWS operator for an input state $|u\rangle$ in bra-ket notation reads

$$\begin{aligned} \langle u|Q_{\hat{n}}^{(S)}|u\rangle &= \langle u|\vec{k}\cdot\hat{n}|u\rangle - \langle v|\vec{k}\cdot\hat{n}|v\rangle \\ &= \langle\vec{k}\cdot\hat{n}\rangle_{\text{in}} - \langle\vec{k}\cdot\hat{n}\rangle_{\text{out}}\,, \end{aligned} \tag{3.6}$$

where $|v\rangle = S|u\rangle$ is the corresponding output vector. This shows that $Q_{\hat{n}}^{(S)}$ measures the momentum difference between the incident and outgoing wave and is thus related to the momentum transferred to the system in $\hat{n}$-direction.

The above derivation has been carried out for a global parameter change and is not easily adaptable to arbitrary local parameter changes. We therefore utilize the effective Hamiltonian framework briefly introduced in Section 1.1 to arrive at a more general expression relating the asymptotic quantities like the input state and the scattering matrix with the local wave function inside the system. We start with the scattering matrix [Eq. (1.10)]

$$S = -\mathbb{1} + 2iV^\dagger G V\,, \tag{3.7}$$

Die approbierte gedruckte Originalversion dieser Dissertation ist an der TU Wien Bibliothek verfügbar.
The approved original version of this doctoral thesis is available in print at TU Wien Bibliothek.
TU Bibliothek WIEN Your knowledge hub

where $G = (G_0^{-1} + iVV^\dagger)^{-1}$, $G_0 = [\Delta + U(\vec{r})]^{-1}$ is the Green's function of the scalar Helmholtz equation and $U(\vec{r}) = n(\vec{r})^2 k^2$ is the corresponding potential. Next, the derivative of Eq. (3.7) with respect to θ reads

$$\frac{dS}{d\theta} = -2iV^\dagger G \frac{dU}{d\theta} GV \,, \tag{3.8}$$

where we have assumed that the coupling matrices V are independent of the parameter θ. Substituting Eqs. (3.7) and (3.8) into the GWS operator then yields

$$Q_\theta^{(S)} = 2(\mathbb{1} + 2iV^\dagger G^\dagger V)V^\dagger G \frac{dU}{d\theta} GV \,. \tag{3.9}$$

For a unitary scattering matrix, we can further make use of the relation [71]

$$-2iG^\dagger VV^\dagger G = G - G^\dagger \tag{3.10}$$

and arrive at

$$Q_\theta^{(S)} = 2V^\dagger G^\dagger \frac{dU}{d\theta} GV \,. \tag{3.11}$$

Since the wave function $|\psi_u\rangle$ for an arbitrary input state $|u\rangle$ can be written as [71]

$$|\psi_u\rangle = 2iGV|u\rangle \,, \tag{3.12}$$

the expectation value of the GWS operator becomes

$$\langle u|Q_\theta^{(S)}|u\rangle = \frac{1}{2}\langle\psi_u|\frac{dU}{d\theta}|\psi_u\rangle \,. \tag{3.13}$$

This relation is very powerful since it relates asymptotic quantities like the input vector $|u\rangle$ (typically a coefficient vector $\vec{u}$ of modal amplitudes) and the GWS operator with the corresponding wave function inside the scattering system $|\psi_u\rangle$ (typically a spatially resolved electric field distribution) and the local or global derivative of the potential $dU/d\theta$. In other words, it allows the extraction of information about the local wave function inside the system via the knowledge of asymptotic quantities only. This in turn enables us to assign physical meaning to the eigenvalues of different $Q_\theta^{(S)}$ operators with the advantage that Eq. (3.13) can be easily evaluated also for a local parameter change such as the position of a single scatterer inside a disordered medium.

In the following, we investigate different $Q_\theta^{(S)}$ operators and show, that choosing θ to be either the position, the radius, the rotational angle or the refractive index of an arbitrarily shaped target buried deeply inside a disordered medium results in GWS eigenstates whose corresponding eigenvalues are related to the transfer of a well-defined linear, radial or angular momentum to that target or to the intensity stored inside of it.

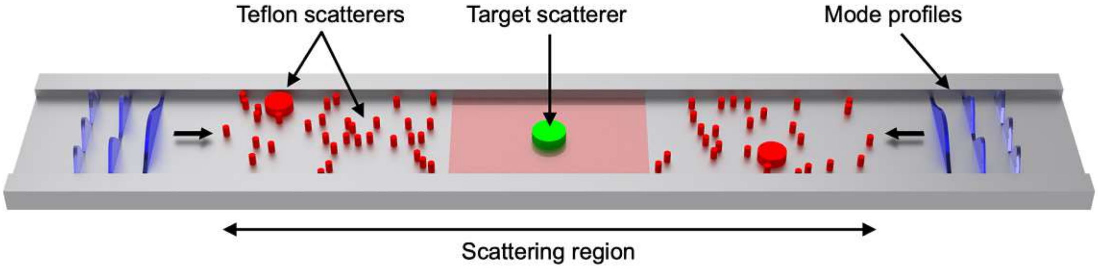

Figure 3.1: Sketch of the microwave waveguide used in the experiment. The length and width of the scattering region are $L = 50$ cm and $W = 10$ cm, respectively, and its height is $h = 8$ mm. Due to the small height, only TE_{m0} modes can be excited at the operational frequency reducing the numerical problem to a two-dimensional waveguide with hard walls in the transverse direction and semi-infinite leads on the left and right. Experimentally, waves are injected by 8 antennas on each side of the waveguide (not shown). Red cylinders indicate the randomly distributed Teflon scatterers (with radii of 2.55 mm and 11 mm and a refractive index of $n = 1.44$), whereas the green cylinder represents a target scatterer whose material, size and shape is chosen specifically for each of the different GWS operators we investigate. The surrounding disorder is characterized by a transport mean free path $\ell^* \approx 35$ cm $= 0.7L$ and a scattering mean free path of $\ell_s \approx 27$ cm $= 0.54L$. The top plate (not shown) features small grid holes through which the electric field is measured in the red-shaded region around the target.

To set the stage for our investigations, we specify our system of choice which is given by a rectangular microwave waveguide as depicted in Fig. 3.1. This experimental setup gives access to the full scattering matrix as well as to the electric field distribution inside the waveguide. Moreover, it allows the injection of arbitrary superpositions of waveguide modes from both sides and enables the variation of the scattering geometry needed for $dU/d\theta$. The waveguide contains randomly distributed Teflon scatterers simulating a disordered medium and a target scatterer placed in the middle of the scattering region. The operational frequency is set to 12.75 GHz resulting in a wavelength of $\lambda = 2\pi/k = 2.35$ cm at which 8 transverse TE_{m0} modes can propagate. Note that the experimental waveguide suffers from weak global absorption and thus we use $q_\theta^{(S)}$ containing S^{-1} (rather than $Q_\theta^{(S)}$ which contains $S^\dagger$) such that the eigenvalues are only related to the derivative of the scattering phase. Since the experimentally measured scattering matrix is only close to unitary, the resulting eigenvalues will be complex (just like for the principal modes) and thus we consider their absolute values if we speak about the GWS eigenvalues in the following. To showcase the good agreement between experimental measurements and numerical simulations, we also compare the spatial intensity distributions of the corresponding eigenstates of the first GWS operator considered below.

As a first parameter, we choose θ to be the orientation angle φ (not to be confused with the scalar test function in Section 2.1) of a non-circular target in which case the corresponding GWS operator is given by $q_\varphi^{(S)} = -iS^{-1}dS/d\varphi$. Utilizing Eq. (3.13), we show in the supplementary material of [55] that the GWS eigenvalue $\tau_\varphi^{(i)}$ is half of the torque M_z the corresponding eigenstate $\vec{u}_\varphi^{(i)}$ exerts onto the target if the latter is metallic:

$$M_z[\vec{u}_\varphi^{(i)}] \equiv \int_{\mathcal{C}} [\vec{m}_\perp(\vec{c}) \times \vec{n}(\vec{c})|\partial_{\vec{n}}\psi(\vec{c})|^2]_z \, ds = 2\tau_\varphi^{(i)} \,. \tag{3.14}$$

Here, the integral is taken along the target's boundary $\mathcal{C}$ which is parametrized by $\vec{c}$. The quantity $\vec{m}_\perp(\vec{c})$ is the lever (the part of the distance from the boundary to the target's center of mass that is normal to $\vec{n}$) and $\vec{n}(\vec{c})|\partial_{\vec{n}}\psi(\vec{c})|^2$ is the normal force exerted by the electric field $\psi(\vec{c})$ at every point on the boundary. It's important to note that no approximations have been applied in the derivation of this relation and thus the GWS eigenvalue $\tau_\varphi^{(i)}$ is a direct measure for the torque that is locally exerted onto a target. Experimentally, the GWS operator $q_\varphi^{(S)}$ is obtained by approximating the derivative by a finite difference using the angles $\varphi = \pm 5°$ (and $\varphi = 0°$ for S^{-1}). To visualize how GWS eigenstates manage the optimal transfer of angular momentum, we consider an empty waveguide with a single complex-shaped target in its center and experimentally inject the eigenstate corresponding to the largest eigenvalue. The resulting measured intensity distribution around the target is shown in Fig. 3.2(a), where one can clearly see that the wave focuses onto the point of the target with the largest lever, thus maximizing the applied torque. Moreover, this eigenstate does not only transfer angular, but also linear momentum to the target causing a force which would move the target in a certain direction.

If one is only interested in rotating the target while keeping the position of its center of mass fixed, one can choose two eigenstates $\vec{u}_\varphi^{(1)}$ and $\vec{u}_\varphi^{(2)}$ that apply a high torque in the same direction, but transfer linear momentum in opposite directions. To minimize the linear momentum transfer, one can then superpose those two eigenstates $\vec{s} = \vec{u}_\varphi^{(1)} + \vec{u}_\varphi^{(2)}$ resulting in an intensity distribution that focuses onto both of the opposite, most protruding parts of the target, as can be seen in Fig. 3.2(b).

Figures 3.2(c) and (d) show the corresponding results from numerical simulations which are in very good agreement with the experimental measurements. However, the order of the eigenstates featuring the two largest eigenvalues is reversed in the numerical simulation, i.e., the eigenstate shown in Fig. 3.2(c) features the second largest eigenvalue. This might be caused by the fact that the experimental setup suffers from weak global absorption (which is not included in the simulation), noise, slightly varying antenna couplings as well as small uncertainties in the fabrication and adjustment of the orientation angle of the target which together can strongly effect the scattering phase.

To show that this approach also works in the multiple scattering regime, we consider a metallic square target embedded in a disordered medium formed by

TU Bibliothek Your knowledge hub WIEN
Die approbierte gedruckte Originalversion dieser Dissertation ist an der TU Wien Bibliothek verfügbar.
The approved original version of this doctoral thesis is available in print at TU Wien Bibliothek.

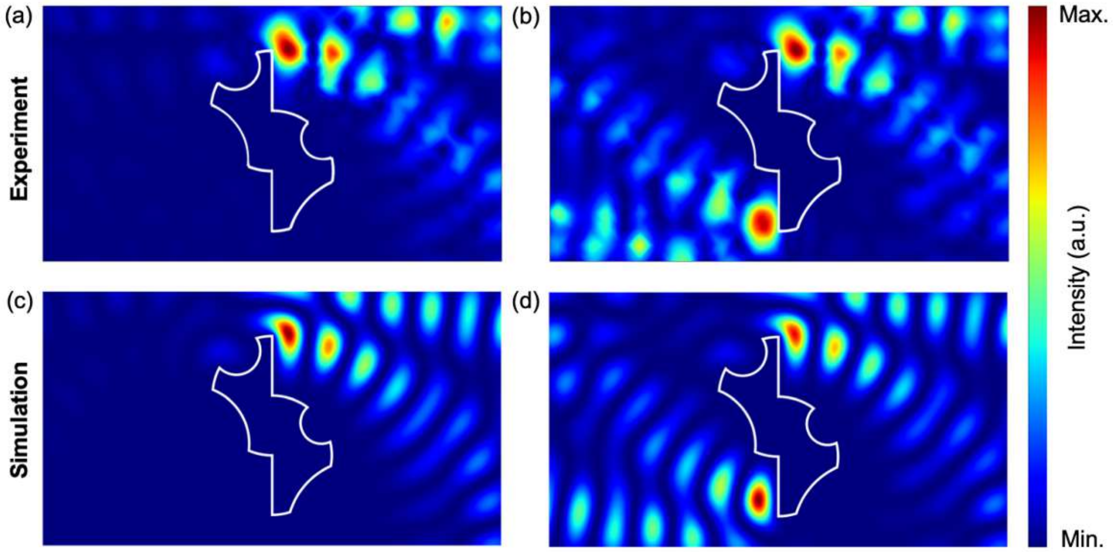

Figure 3.2: Spatial electric field intensities of $q_\varphi^{(S)}$ eigenstates for a complex-shaped metallic target in an empty waveguide. (a) Experimentally measured intensity distribution of $\vec{u}_\varphi^{(1)}$ corresponding to the largest eigenvalue $|\tau_\varphi^{(1)}| \approx 8.52$ which focuses onto the point with the maximal lever. (b) Experimentally measured intensity distribution of the superposition $\vec{s} = \vec{u}_\varphi^{(1)} + \vec{u}_\varphi^{(2)}$ of the eigenstates with the two largest eigenvalues (with $|\tau_\varphi^{(2)}| \approx 7.23$) that transfers angular, but almost no linear momentum to the target. The corresponding intensity builds up on both of the most protruding parts of the target. (c,d) Corresponding results from a numerical simulation, where (c) shows $\vec{u}_\varphi^{(2)}$ which features the second largest eigenvalue.

randomly distributed scatterers (similar to the scattering configuration shown in Fig. 3.1). Figure 3.3(a) shows the intensity distribution of the $q_\varphi^{(S)}$ eigenstate featuring the largest eigenvalue, where one can clearly see that even in such a strongly scattering regime the wave still focuses onto the point with the maximal lever in order to exert the maximal possible torque onto the target. On the other hand, eigenstates with a small eigenvalue should transfer very little angular momentum to the target, which is exactly what can be seen in Fig. 3.3(b). Here, the depicted eigenstate scatters off both of the square's side walls in order to exert only a negligible amount of torque. Figures 3.3(c) and (d) again show the corresponding results from numerical simulations, where – just like in Fig. 3.2 – the eigenvalues and thus also their order are slightly different compared to the ones obtained in the experiment. The latter might again be caused by the experimental imperfections mentioned above, with additional uncertainties in the placement of the randomly distributed Teflon scatterers coming into play here.

In a second step, we study the GWS operator in which the parameter $\theta = R$ is chosen to be the radius of a metallic circular target surrounded by a disordered

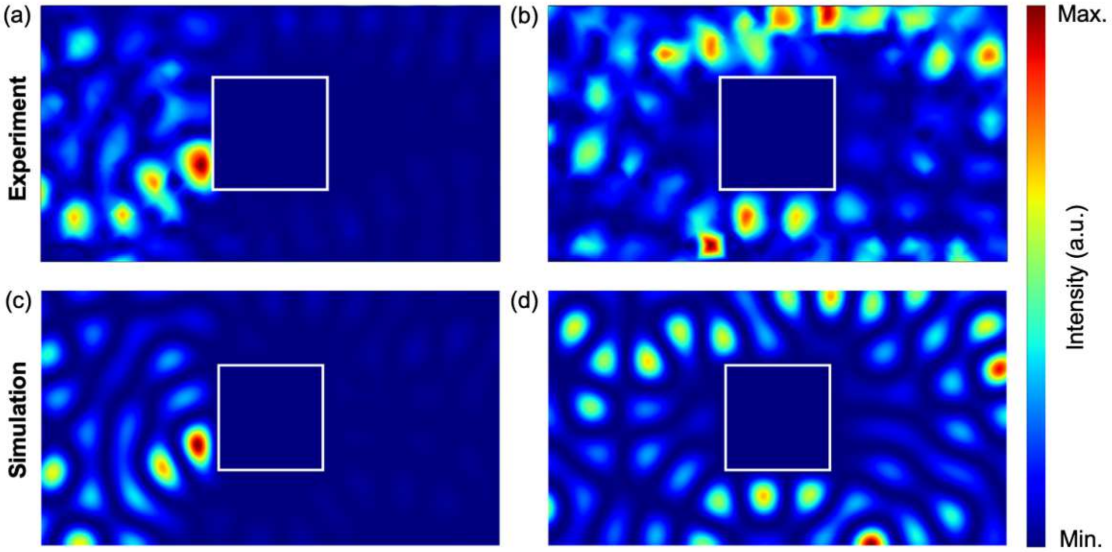

Figure 3.3: Spatial electric field intensities of $q_\varphi^{(S)}$ eigenstates for a metallic square target (with a side length of 35 mm) embedded in a disordered medium. (a) Experimentally measured intensity distribution of $\vec{u}_\varphi^{(\max)}$ corresponding to the largest eigenvalue $|\tau_\varphi^{(\max)}| \approx 5.85$. Even in such a disordered medium, this eigenstate focuses onto the point with the maximal lever to maximize the exerted torque. (b) Experimentally measured intensity distribution of an eigenstate with a small eigenvalue of $|\tau_\varphi^{(\text{small})}| \approx 0.2$ which transfers very little angular momentum since it scatters off both of the square's side walls. (c,d) Corresponding results from a numerical simulation, where (c) again shows the eigenstate with the second largest eigenvalue.

medium. As above, using Eq. (3.13) lets us assign physical meaning to the eigenvalues $\tau_R^{(i)}$ of $q_R^{(S)} = -iS^{-1}dS/dR$ if the scattering matrix is unitary. As shown in the supplementary material of [55], the eigenvalues are linearly proportional to the radiation pressure P an eigenstate $\vec{u}_R^{(i)}$ applies to the metallic target:

$$P[\vec{u}_R^{(i)}] \equiv \int_0^{2\pi} |\partial_r \psi(r=R)|^2 \, d\varphi = -\frac{2\tau_R^{(i)}}{R} \, . \tag{3.15}$$

In the above expression, the absolute value squared of the radial derivative of the electric field ψ gets integrated along the boundary of the target with radius R. Thus, the eigenstate featuring the largest (smallest) eigenvalue maximizes (minimizes) the integrated radial derivative of the electric field resulting in the maximal (minimal) possible pressure. To verify this experimentally, we set up the GWS operator $q_R^{(S)}$ with the derivative dS/dR being approximated by a finite difference using cylinders with radii $R = 16$ and 12 mm (and $R = 14$ mm for S^{-1}). The resulting eigenstate corresponding to the largest eigenvalue is shown in Fig. 3.4(a), where one can

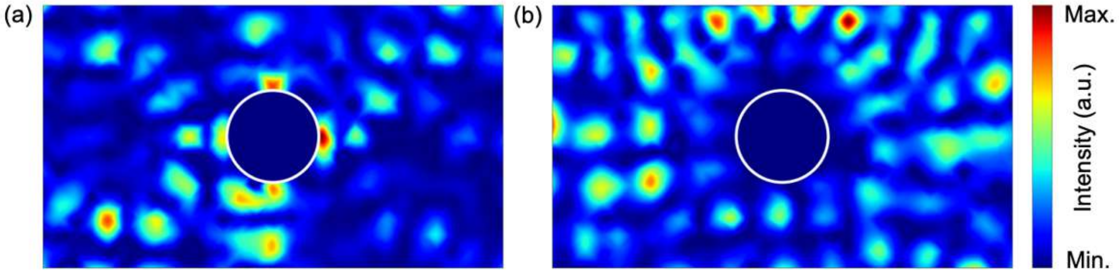

Figure 3.4: Experimentally measured spatial intensity distributions of $q_R^{(S)}$ eigenstates for a cylindrical metallic target (with a radius of $R = 14$ mm) embedded in a disorder of randomly placed Teflon scatterers. (a) Intensity distribution of the eigenstate corresponding to the largest eigenvalue $|\tau_R^{(\max)}| \approx 709$. A focus on the metallic boundary of the cylinder can clearly be observed, verifying that these states control the applied radiation pressure. (b) Intensity distribution of an eigenstate featuring a small eigenvalue of $|\tau_R^{(\text{small})}| \approx 86$, which avoids the target in order to minimize the applied pressure.

clearly see the intensity build-up on all sides of the target's boundary to maximize the applied pressure. On the other hand, an eigenstate featuring a small eigenvalue minimizes the applied pressure by avoiding the target as can be seen in Fig. 3.4(b).

Another possible parameter to consider is the permittivity $\varepsilon = n^2$ of a dielectric scatterer resulting in the GWS operator $q_\varepsilon^{(S)} = -iS^{-1}dS/d\varepsilon$ with eigenvalues $\tau_\varepsilon^{(i)}$. In this case, Eq. (3.13) reduces to the simple expression

$$I[\vec{u}_\varepsilon^{(i)}] \equiv \int_A |\psi(\vec{r})|^2 \, dA = \frac{2\tau_\varepsilon^{(i)}}{k^2} \,, \tag{3.16}$$

which measures the integrated intensity inside the target area A and is thus related to the local dwell time inside the target scatterer [10, 70]. Therefore, in order to maximize (minimize) the intensity stored inside a target scatterer, one only has to inject the eigenstate corresponding to the largest (smallest) eigenvalue into the system. To experimentally obtain the operator $q_\varepsilon^{(S)} = -iS^{-1}dS/d\varepsilon$, the refractive index of the target scatterer has to be varied. Instead of directly changing the Teflon target's refractive index, we vary its height from $h = 4$ to 6 to 8 mm in order to obtain the effective permittivity values $\varepsilon = 1.4884$, 1.7689 and 2.0736, respectively. The latter is justified by the fact that only TE_{m0} modes can be excited at the operational frequency which are constant in the vertical z-direction (see Fig. 1.3). The experimentally measured intensity distribution of the eigenstate with the largest eigenvalue obtained in this way is depicted in Fig. 3.5(a). Here, the corresponding eigenstate focuses directly into the target scatterer in order to store the maximal amount of intensity inside of it – as predicted. An eigenstate corresponding to a small eigenvalue again avoids the target and reduces the amount of stored intensity, as can be seen in Fig. 3.5(b).

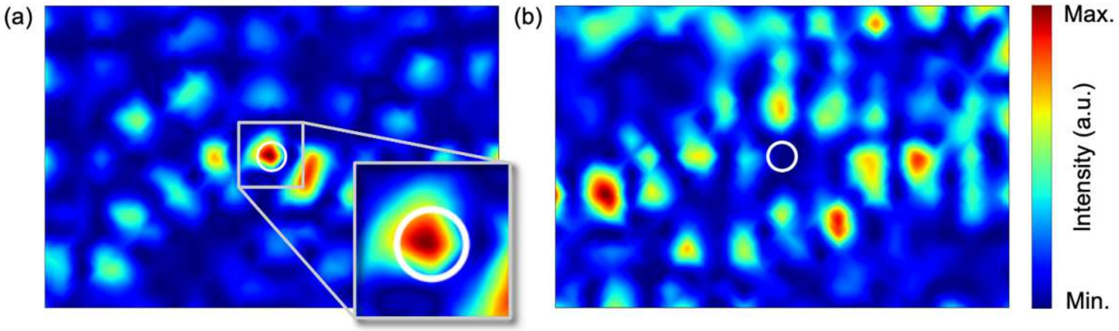

Figure 3.5: Experimentally measured spatial intensity distributions of $q_\varepsilon^{(S)}$ eigenstates for a small cylindrical Teflon target (with a radius of $R = 3.75$ mm) surrounded by randomly placed Teflon scatterers. (a) Intensity distribution of the eigenstate corresponding to the largest eigenvalue $|\tau_\varepsilon^{(\mathrm{max})}| \approx 1.96$ which clearly focuses inside of the dielectric target. (b) Intensity distribution of the eigenstate with a small eigenvalue of $|\tau_\varepsilon^{(\mathrm{small})}| \approx 0.46$, which avoids the target in order to minimize the stored intensity in the target region.

Last, we also consider the spatial shift of a single scatterer into a certain direction specified by the unit vector $\hat{n}$ as parameter θ. For a global shift, we have already shown above that the resulting eigenvalues are related to the momentum difference between the incident and outgoing wave [see Eq. (3.6)]. In case of a local spatial shift, i.e., a shift of the position of a single scatterer inside a disordered medium, Eq. (3.13) enables us to generalize this result and relate the GWS eigenvalue $\tau_{\hat{n}}^{(i)}$ to the wave field inside the scattering system. For a metallic circular target with radius R, Eq. (3.13) boils down to

$$F[\vec{u}_{\hat{n}}^{(i)}] \equiv \hat{n} \cdot \int_0^{2\pi} \begin{pmatrix} \cos\varphi \\ \sin\varphi \end{pmatrix} |\partial_r \psi(r = R)|^2 \, d\varphi = -\frac{2\tau_{\hat{n}}^{(i)}}{R} \,, \tag{3.17}$$

where the integral runs over the boundary of the target at $r = R$. Since Eq. (3.17) is the generalization of Eq. (3.6) to local position shifts, it corresponds to the local change in the optical momentum of the field and thus represents the locally applied force. Therefore, injecting an eigenstate $\vec{u}_{\hat{n}}^{(i)}$ into a scattering system makes it possible to apply a well-defined force in $\hat{n}$-direction to a single target scatterer inside a disorder. As one example, we experimentally set up the operator $q_{\hat{x}}^{(S)}$ for which $\hat{n} = (1, 0)^T \equiv \hat{x}$ denotes a shift of the target in x-direction, where we shift a metallic square target (rather than a circular target) by $\Delta x = \pm 2$ mm from its initial position to calculate the derivative $dS/d\hat{x}$. The intensity distributions of the resulting eigenstates with the largest and smallest eigenvalue are now shown in Figs. 3.6(a) and (b), respectively. One can clearly see that the eigenstate with the largest eigenvalue scatters off the target's back side to apply the maximal force in the negative x-direction [see Fig. 3.6(a)]. The eigenstate featuring the smallest

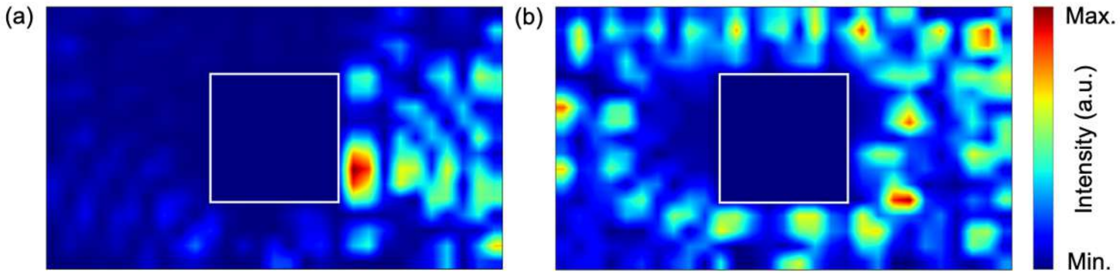

Figure 3.6: Experimentally measured spatial intensity distributions of $q_{\hat{x}}^{(S)}$ eigenstates for a metallic square target (with a side length of 45 mm) surrounded by a disorder of randomly placed Teflon scatterers. (a) Intensity distribution of the eigenstate corresponding to the largest eigenvalue $|\tau_{\hat{x}}^{(\max)}| \approx 520.13$ which hits the target from the right in order to apply the maximal force in the negative x-direction. (b) Intensity distribution of the eigenstate with a small eigenvalue of $|\tau_{\hat{x}}^{(\mathrm{small})}| \approx 10.84$, which avoids the target and only scatters off the square's side walls in order to transfer almost no linear momentum in x-direction.

eigenvalue avoids the front and back face of the target and only scatters off its sides in order to minimize the momentum transfer in the longitudinal direction [see Fig. 3.6(b)].

The relations in Eq. (3.14), (3.15) and (3.17) have all been derived for impenetrable metallic targets, however, similar linear relations between the eigenvalues and the physical quantities can also be found for dielectric targets. For completeness, the relations for a target with permittivity ε read as follows (for a derivation and the numerical verification of these relations we refer to the supplementary material of [55]):

$$M_z[\vec{u}_\varphi^{(i)}] \equiv \int_{\mathcal{C}} [\vec{m}_\perp(\vec{c}) \times \vec{n}(\vec{c}) |\psi(\vec{c})|^2]_z \, ds = -\frac{2\tau_\varphi^{(i)}}{k^2(\varepsilon - 1)} , \tag{3.18}$$

$$P[\vec{u}_R^{(i)}] \equiv \int_0^{2\pi} |\psi(r = R)|^2 \, d\varphi = \frac{2\tau_R^{(i)}}{Rk^2(\varepsilon - 1)} , \tag{3.19}$$

$$F[\vec{u}_{\hat{n}}^{(i)}] \equiv \hat{n} \cdot \int_0^{2\pi} \begin{pmatrix} \cos\varphi \\ \sin\varphi \end{pmatrix} |\psi(r = R)|^2 \, d\varphi = \frac{2\tau_{\hat{n}}^{(i)}}{Rk^2(\varepsilon - 1)} , \tag{3.20}$$

where for Eq. (3.19) and (3.20) a circular target with radius R has been assumed.

An important point that we have only briefly touched on until now is the question of optimality. Each GWS operator is Hermitian in case of a unitary scattering matrix thus providing a complete and orthonormal set of basis states. This means, that the eigenstate that corresponds to the largest eigenvalue applies the highest possible torque, pressure or force to the target or optimally focuses inside of it.

3.2 Optimal focusing compared to the field matrix method

To showcase the optimality of the GWS eigenstates, we compare the latter to another method for optimal focusing which has been introduced in Ref. [88]. Therein, the authors achieve an optimal focus onto a point inside a disorder by using the so-called field matrix $e(x)$ which relates the incident wave field with the field at a specific depth x. More precisely, the matrix elements $e_{ba}(x)$ in a chosen basis relate the incident wave field ψ_a in channel a with the field $\psi_b(x)$ at a specific depth x in channel b, i.e., $\psi_b(x) = e_{ba}(x)\psi_a$. The optimal focus onto a target point β can then be achieved by shaping the incident wavefront as

$$\psi_a^{(\mathrm{opt})}(x) = \mathcal{N}_\beta(x) e^*_{\beta a}(x)\,. \tag{3.21}$$

Here, $\mathcal{N}_\beta(x) = 1/\sqrt{\sum_a |e_{\beta a}(x)|^2}$ is a normalization factor (see also [22]) which ensures that the incident flux is unity and the complex conjugate has to be taken to bring the fields into phase at the focusing point. Interpreting the field matrix as a transmission matrix into a specific depth of the scattering medium, Eq. (3.21) is equivalent to selecting a suitable superposition of input channels a that focuses onto the corresponding "output" channel β at depth x.

To compare the field matrix method with the GWS approach using $q_\varepsilon^{(S)}$ in the numerical simulations[15], we choose a dielectric sub-wavelength target scatterer embedded in a disorder. For such a sub-wavelength target, our method converges to the limit of focusing onto a point, as considered in the field matrix method. Moreover, we choose the basis of waveguide modes for the input channels a, while we use a spatially-resolved basis for the "output" channels b by reading out the field in the transverse y-direction at depth x. As focus point β we choose the center of the target scatterer. The input coefficients obtained from Eq. (3.21) now only represent the input from the left waveguide port, however, the optimal GWS eigenstates are based on the full scattering matrix resulting in an input wave injected from both waveguide ports. Therefore, we also evaluate Eq. (3.21) for an input from the right waveguide port and finally inject both of the obtained field matrix states from their respective sides. Figure 3.7(a) compares the results obtained with both methods on a transverse slice through the center of the target scatterer, i.e., the focusing plane, where we find that the $q_\varepsilon^{(S)}$ eigenstate with the largest eigenvalue is indistinguishable from the one obtained with the field matrix method. Therefore, both methods deliver an optimal focus in form of a single peak inside the target.

---

[15] Note that we use a much finer finite difference derivative than in the experiment for the numerical calculation of $dS/d\varepsilon$ in this case which – together with the unitary S-matrix provided by our numerics – makes the GWS operator Hermitian, i.e., $q_\varepsilon^{(S)} = Q_\varepsilon^{(S)} = Q_\varepsilon^{(S)\dagger}$, and in turn its eigenstates optimal.

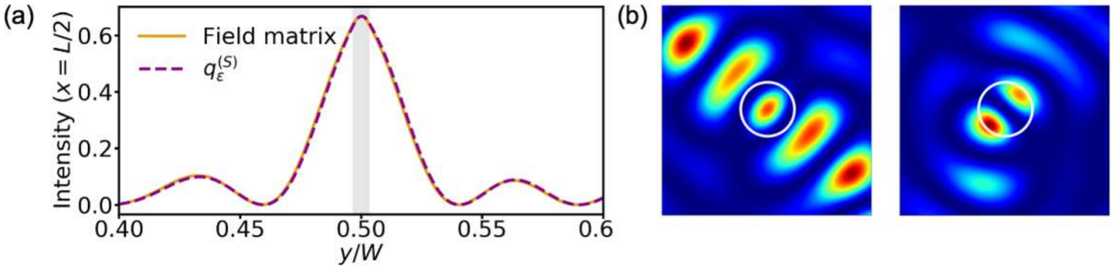

Figure 3.7: (a) Comparison of the states obtained with the field matrix method and the GWS approach using the eigenstate of $q_\varepsilon^{(S)}$ with the largest eigenvalue. Shown are the intensity distributions on a transverse slice through through the center (at $x = L/2$) of the sub-wavelength Teflon target scatterer. The latter has a diameter of 0.69 mm which corresponds to 10% of the wavelength inside the target (the grey-shaded region marks its extension). In these simulations we use the same geometry as in the experiment (see Fig. 3.1), featuring a disorder, but with a frequency of 30 GHz resulting in 20 propagating modes and a wavelength of 1 cm. For such an almost point-like scatterer, both states perfectly coincide confirming our prediction that we can achieve an optimal focus. (b) Comparison of the spatial intensity distributions of the states obtained with the field matrix method (left) and the GWS approach (right) for a larger target with a diameter of 10.4 mm. Similar to (a), the focus point for the field matrix method has been chosen as the target's center and ε is varied inside the entire target for the calculation of $q_\varepsilon^{(S)}$. For such a larger scatterer, the GWS approach results in an optimal eigenstate which features two intensity maxima leading to a two-fold increase of the integrated intensity inside the target scatterer as compared to the single peak produced by the field matrix method.

In contrast to the field matrix method, which is designed for focusing on a single point, the GWS concept, however, also enables optimal focusing on extended targets of arbitrary size. For targets larger than the wavelength, the GWS eigenstate with the largest eigenvalue manages to deposit the maximal amount of intensity by creating a wave that features multiple intensity maxima inside the target area. This can, e.g., be seen in the right plot in Fig 3.7(b), where the larger target leads to a $q_\varepsilon^{(S)}$ eigenstate that fits two intensity maxima into it. The state obtained with the field matrix method for a focus on the target's center, however, only yields a state which features a single intensity maximum. In the case considered here, the use of the optimal GWS eigenstate leads to a doubling of the integrated intensity within the target compared to the field matrix state. Furthermore, it should be noted that the GWS approach exclusively relies on the knowledge of far field information, whereas the field matrix method requires local field information at the focusing plane inside the scattering system which is difficult to obtain.

3.3 Incomplete access to the scattering matrix

Up to now, we have considered GWS operators based on the full scattering matrix, which captures all the incoming and outgoing flux, however, the latter is very challenging to measure experimentally. We therefore investigate in the following the GWS concept for the case where only a subpart of the scattering matrix is accessible [56]. Specifically, we consider the scattering setup depicted in Fig. 3.1 at an operational frequency of 15.5 GHz at which 10 TE_{m0} modes can propagate and restrict ourselves to the measurement of the 10×10 transmission matrix (instead of the full scattering matrix). To obtain the GWS operator $q_{\hat{y}}^{(t)} = -it^{-1}dt/d\hat{y}$, we shift a circular brass target with radius $R = 8.825$ mm embedded in a disorder in the transverse y-direction by $\Delta y = \pm R$. In contrast to the scattering matrix, the transmission matrix is now sub-unitary since the reflected part of the incident wave is not contained in t. Even worse, strong reflections can cause t to be singular in which case no ordinary inverse exists and the calculation of a pseudoinverse as described in Appendix C has to be applied.

To verify that the GWS protocol creates eigenstates which transfer momentum to the central brass target, we calculate the eigenstates of $q_{\hat{y}}^{(t)}$, inject them into the system and measure the intensity distribution in the close vicinity of the target scatterer. The obtained intensity distributions for the eigenstates with the three largest eigenvalues are shown in Fig. 3.8(a), where one can clearly see that the waves hit the target from the side transferring a large amount of linear momentum in shifting direction. As a second check, Fig. 3.8(b) shows the intensity distributions of the same eigenstates in a scattering setup in which the central target has been removed. In this case, the intensity distributions drastically change since the waves do not get back-reflected anymore, but instead propagate freely through the area in which the target scatterer was located. Figure 3.9(a) shows the intensity distributions of the eigenstates with the three smallest eigenvalues which avoid the target thus transferring almost no linear momentum to it. Therefore, the intensity patterns remain almost unchanged when the target scatterer is removed [see Fig. 3.9(b)].

Due to the sub-unitarity of t, the eigenvalues of $q_{\hat{n}}^{(t)}$ are complex and no longer correspond directly to the transferred momentum, but still can be related to the momentum transfer described by the Hermitian operator $Q_{\hat{n}}^{(S)}$ as we will show in the following. The eigenstates of $q_{\hat{n}}^{(t)}$ are now only injected from the left waveguide port and in order to compare them to the eigenstates of $Q_{\hat{n}}^{(S)}$ which are injected from both ports, we write the GWS operator $Q_{\hat{n}}^{(S)}$ in its block structure

$$Q_{\hat{n}}^{(S)} = \begin{pmatrix} Q_{\hat{n}}^{(S,11)} & Q_{\hat{n}}^{(S,12)} \\ Q_{\hat{n}}^{(S,21)} & Q_{\hat{n}}^{(S,22)} \end{pmatrix}. \tag{3.22}$$

Calculating its expectation value for a wave entering only from the left waveguide

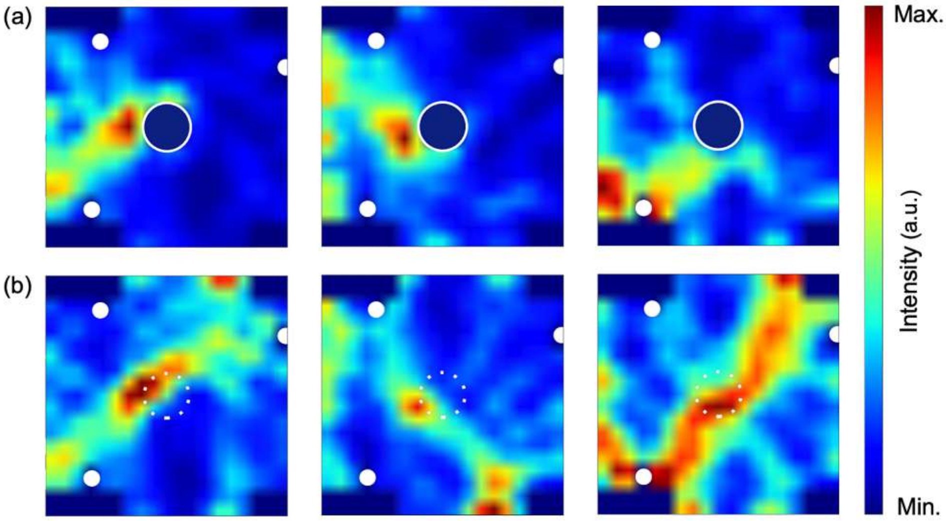

Figure 3.8: (a) Measured spatial intensity distributions of the $q_{\hat{y}}^{(t)}$ eigenstates with the three largest eigenvalues $|\tau_{\hat{y}}| \approx 96.9$, 81.6 and 66.9 (from left to right). Each of these eigenstates features an enhanced intensity distribution at one side of the target scatterer (central white circle) resulting in a large momentum transfer to it. (b) Same as in (a), but with the central target scatterer removed which strongly changes the intensity patterns.

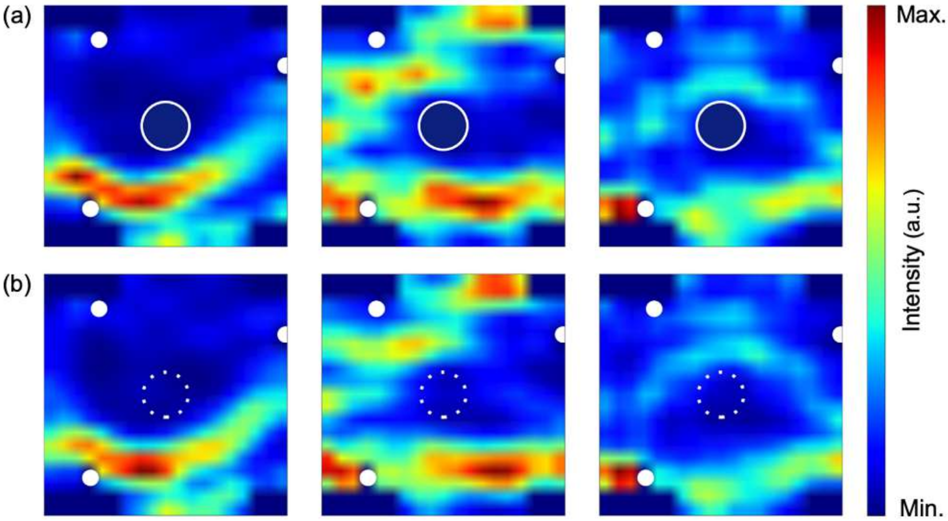

Figure 3.9: Same as Fig 3.8, but for the eigenstates of $q_{\hat{y}}^{(t)}$ with the three smallest eigenvalues $|\tau_{\hat{y}}| \approx 1.9$, 2.1 and 6.0 (from left to right). (a) The measured intensity patterns clearly avoid the target scatterer in order to minimize the momentum transferred to it. (b) Same as in (a), but with the central target scatterer removed which leaves the intensity patterns almost unchanged.

port, i.e., $\vec{u} = (\vec{u}_l, 0)^T$ gives

$$\begin{aligned}\langle Q_{\hat{n}}^{(S)} \rangle &= \vec{u}^\dagger Q_{\hat{n}}^{(S)} \vec{u} \\ &= \vec{u}_l^\dagger Q_{\hat{n}}^{(S,11)} \vec{u}_l \\ &= \langle Q_{\hat{n}}^{(S,11)} \rangle \\ &= \langle \vec{k} \cdot \hat{n} \rangle_{\text{in}} - \langle \vec{k} \cdot \hat{n} \rangle_{\text{out}} \equiv \Delta k_{\hat{n}} \,,\end{aligned} \tag{3.23}$$

where $\Delta k_{\hat{n}}$ is the local momentum difference in $\hat{n}$-direction. Furthermore, $Q_{\hat{n}}^{(S,11)}$ is the upper left block of $Q_{\hat{n}}^{(S)}$ which can be written as

$$\begin{aligned}Q_{\hat{n}}^{(S,11)} &= -it^\dagger \frac{dt}{d\hat{n}} - ir^\dagger \frac{dr}{d\hat{n}} \\ &= t^\dagger t q_{\hat{n}}^{(t)} + Q_{\hat{n}}^{(r)} \,.\end{aligned} \tag{3.24}$$

Calculating now the expectation value of $Q_{\hat{n}}^{(S,11)}$ for an eigenstate of $q_{\hat{n}}^{(t)}$ and resolving for its complex eigenvalue $\tau_{\hat{n}}$ (in the following we will omit the eigenstate index for the sake of readability) yields

$$\tau_{\hat{n}} = \frac{1}{|t|^2} \left(\Delta k_{\hat{n}} - \langle Q_{\hat{n}}^{(r)} \rangle \right) \tag{3.25}$$

with $|t|^2 = \langle t^\dagger t \rangle$ being the global transmittance of the eigenstate. In analogy to the derivation of Eq. (1.19), the eigenvalue of the GWS operator can also be written as [71]

$$\tau_{\hat{n}} = \frac{d\phi_t}{d\hat{n}} - i \frac{d \ln(|t\vec{u}_l|)}{d\hat{n}} \,, \tag{3.26}$$

where the real part is the derivative of the global transmitted scattering phase ϕ_t. The imaginary part can be interpreted as the global change in the output intensity with respect to a change of the local transverse position of the target scatterer. Thus, comparing Eq. (3.25) with (3.26) shows that the imaginary part of the $q_{\hat{n}}^{(t)}$ eigenvalue can be related to global reflections, i.e.,

$$\operatorname{Im}(\tau_{\hat{n}}) = -\frac{d \ln(|t\vec{u}_l|)}{d\hat{n}} = -\frac{1}{|t|^2} \operatorname{Im} \left(\langle Q_{\hat{n}}^{(r)} \rangle \right) . \tag{3.27}$$

These reflections have been omitted in the construction of $q_{\hat{n}}^{(t)}$, however, they do affect the corresponding eigenvalues. Most notably, the reflection term $\langle Q_{\hat{n}}^{(r)} \rangle$ in Eq. (3.25) also features a real part and thus the derivative of the transmitted scattering phase is not only given by $\Delta k_{\hat{n}}/|t|^2$. To assign further physical meaning to the real part of the eigenvalues, we write the expectation value of $Q_{\hat{n}}^{(S)}$ as a sum of the derivatives of the scattering phases weighted by the output intensities in the corresponding modes, i.e., [71]

$$\begin{aligned}\langle Q_{\hat{n}}^{(S)}\rangle &= \sum_{n=1}^{2N} |(S\vec{u})_n|^2 \frac{d\phi_n}{d\hat{n}} \\ &= \sum_{n=1}^{N} |(r\vec{u}_l)_n|^2 \frac{d\phi_{r,n}}{d\hat{n}} + \sum_{n=1}^{N} |(t\vec{u}_l)_n|^2 \frac{d\phi_{t,n}}{d\hat{n}}\,.\end{aligned} \tag{3.28}$$

In the second line, we have split the sum over all scattering channels into the corresponding reflected and transmitted parts with N being the number of propagating modes. For an evaluation of this expectation value with an eigenstate of $q_{\hat{n}}^{(t)}$, we make use of the fact that the transmitted phase derivatives described by the real part of its eigenvalues are the same for all modes, i.e., $d\phi_{t,n}/d\hat{n} = d\phi_t/d\hat{n} = \mathrm{Re}(\tau_{\hat{n}})$. Thus, bringing this factor in front of the sum and rearranging the above expression yields

$$\begin{aligned}\mathrm{Re}(\tau_{\hat{n}}) = \frac{d\phi_t}{d\hat{n}} &= \frac{1}{|t|^2}\left[\Delta k_{\hat{n}} - \mathrm{Re}\left(\langle Q_{\hat{n}}^{(r)}\rangle\right)\right] \\ &= \frac{1}{|t|^2}\left[\Delta k_{\hat{n}} - \sum_{n=1}^{N} |(r\vec{u}_l)_n|^2 \frac{d\phi_{r,n}}{d\hat{n}}\right].\end{aligned} \tag{3.29}$$

This shows that the derivative of the transmitted scattering phase contains not only the momentum transfer $\Delta k_{\hat{n}}$, but also the derivative of the reflected scattering phase weighted by the corresponding reflected intensities of each mode. Nevertheless, we show in the supplementary material of [56] that a strong correlation between $|\tau_{\hat{n}}|$ and $|\Delta k_{\hat{n}}|$ for $\hat{n} = \hat{x}$ still persists. Notably, we find an even stronger correlation for $|\tau_{\hat{n}}|$ and $|\Delta k_{\hat{n}}|/|t|^2$. However, due to the appearance of $\langle Q_{\hat{n}}^{(r)}\rangle$ in Eq. (3.25), very strong global reflections will inevitably lead to a decrease of this correlation which can be restored by projecting onto highly-transmitting channels via the procedure described in Appendix C (see supplementary material of [56] for more details).

3.4 Conclusion

When the full unitary scattering matrix is available, the GWS concept enables the creation of optimal wavefronts that locally apply a well-defined torque, pressure or force to a target or store a well-defined amount of intensity inside of it. Therefore, we expect the framework of GWS to be optimally suited for optical micromanipulation tasks whose key idea is the application of forces at the position of a target in order to manipulate them in a non-contact manner. Micromanipulation finds application in many different research areas, e.g., in cellular manipulation [89, 90],

TU Bibliothek WIEN Your knowledge hub
Die approbierte gedruckte Originalversion dieser Dissertation ist an der TU Wien Bibliothek verfügbar.
The approved original version of this doctoral thesis is available in print at TU Wien Bibliothek.

in fluid dynamics [91], in microrobotics [92] and in surface imaging [93]. Moreover, it can be used for indirect optical trapping [94], for measuring optical forces [95] as well as for tests of fundamental physics [96, 97]. However, remaining critical challenges include the difficulty of manipulating complex-shaped targets, the embedding of targets in disordered environments and the question of optimality. Optical tweezers, for example, are a powerful tool for trapping particles [89, 98, 99], however, they typically operate with Gaussian beams [100, 101] which are not very well suited for optimally trapping complex-shaped targets. Therefore, recent advances already exploit the possibilities of structured light [102–105]. The presence of a surrounding disordered environment is another critical challenge, especially for applications in biology and soft matter, since a complex medium like, e.g., tissue, scatters the incoming beam and thus destroys the wave pattern required to locally manipulate a target efficiently [106]. Although the emerging field of wavefront shaping has already led to micromanipulation strategies well beyond the standard Gaussian trap [103], optimality has only been approached via iterative computational optimization schemes. The latter have, for example, been used to increase the stiffness of optical traps [107, 108], to enhance micromanipulation capabilities [109] or to trap nano-particles across highly turbid media [106]. However, such iterative schemes do not guarantee the convergence to the global optimum and may require a large number of computational steps. With the GWS concept, we overcome all those difficulties since it applies to arbitrarily shaped targets that can even be embedded in complex scattering environments. Moreover, it provides the optimal solution (in case of having access to the full scattering matrix) only by means of a simple eigenvalue problem. In addition, the already existing applications to avoid disorder in multi-mode fibers [110] and to cool a moving gas of particles [111] as well as its connection to the Fisher information [112, 113] and its extension to time-periodic systems [114] make us confident, that the presented concept has great potential for future innovations. In particular, extending the GWS concept to fully time-dependent systems to enable the optimal spatio-temporal manipulation of targets would be highly desirable.

In the next chapter, we introduce another set of optimal modes which share a close relation with the GWS concept introduced in this chapter. More precisely, a further generalization of the GWS operator gives rise to so-called scattering invariant modes which propagate through a scattering medium as through a homogeneous medium.

Chapter 4

Scattering invariant modes[16]

The eigenstates of the GWS operator q_θ (containing the inverse of the considered scattering, transmission or reflection matrix) introduced in the previous chapter do not only transfer well-defined amounts of a specific physical quantity to a target of interest, but their output profiles are by construction also invariant with respect to a small change in θ [see Section 1.2]. The latter property is caused by the demand that the change of the corresponding output vector for a change of θ is parallel to the unshifted output vector. A natural question that arises in this context is if this invariance to first order in θ can be further extended such that the output profiles of the corresponding eigenstates are invariant with respect to larger changes in the parameter under consideration. As we will show in the following, this can easily be achieved by further generalizing the GWS operator and replacing the derivative of, e.g., the transmission matrix t with respect to θ with a "coarse" finite difference quotient enabling the creation of wave states that propagate through a strongly scattering medium as through a homogeneous medium. More precisely, just as $dt/d\theta$ in $q_\theta^{(t)}$ gives rise to a first-order stability in θ, replacing the derivative with a finite difference quotient with a larger step size $\Delta\theta$ will yield eigenstates whose output profiles are invariant with respect to a change $\theta \to \theta + \Delta\theta$. Note, however, that this invariance does not apply to values between θ and $\theta + \Delta\theta$. To illustrate that, we use $q_\varepsilon^{(t)}$ and generalize it to a finite change in the permittivity $\Delta\varepsilon$ using a forward finite difference quotient to arrive at the following eigenvalue equation:

$$q_{\Delta\varepsilon}^{(t)}\vec{u}_{\Delta\varepsilon}^{(i)} = \left[-it^{-1}(\varepsilon)\frac{t(\varepsilon+\Delta\varepsilon)-t(\varepsilon)}{\Delta\varepsilon}\right]\vec{u}_{\Delta\varepsilon}^{(i)} = \tau_{\Delta\varepsilon}^{(i)}\vec{u}_{\Delta\varepsilon}^{(i)}\,. \tag{4.1}$$

This eigenvalue equation can then be rewritten as follows

$$t(\varepsilon+\Delta\varepsilon)\vec{u}_{\Delta\varepsilon}^{(i)} = \alpha_{\Delta\varepsilon}^{(i)}\,t(\varepsilon)\vec{u}_{\Delta\varepsilon}^{(i)} \tag{4.2}$$

---

[16] The results presented in this chapter were obtained in collaboration with Allard Mosk and his former PhD students Pritam Pai and Jeroen Bosch from Utrecht University. The theoretical analysis and the 2D full-wave numerical simulations were carried out by myself under the supervision of Stefan Rotter, and the 3D simulations were performed by Allard Mosk. The experiments were conducted by Pritam Pai and Jeroen Bosch under the supervision of Allard Mosk. The text and figures in this chapter partially go back to our joint publication [57].

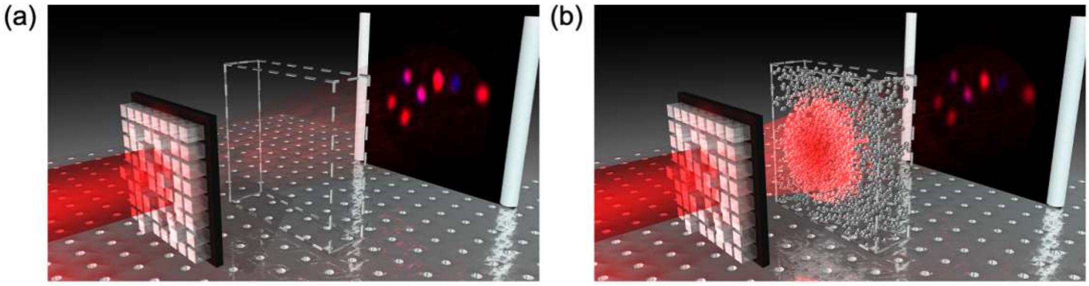

Figure 4.1: (a) A SIM is generated by an SLM and propagates through free space. (b) Using the same SLM configuration, the same input SIM is propagated through a scattering sample which produces the same output pattern as in (a) apart from a reduction in overall brightness and a global phase-shift described by the corresponding complex SIM eigenvalue.

with the eigenvalue

$$\alpha^{(i)}_{\Delta\varepsilon} = (1 + i\Delta\varepsilon\tau^{(i)}_{\Delta\varepsilon}) \, . \tag{4.3}$$

Assuming now that ε is the permittivity of the scatterers in our disorder configuration, using $\varepsilon = \varepsilon_{\text{air}} = 1$ corresponding to the permittivity of air and $\varepsilon + \Delta\varepsilon = \varepsilon_{\text{scat}}$ corresponding to the actual permittivity of the scatterers yields

$$t_{\text{scat}}\vec{u}^{(i)} = \alpha^{(i)} \, t_{\text{air}}\vec{u}^{(i)} \, . \tag{4.4}$$

Here, $t_{\text{scat}} = t(\varepsilon_{\text{scat}})$ and $t_{\text{air}} = t(\varepsilon_{\text{air}})$ are the transmission matrices through the scattering medium and through air, respectively, where we have also omitted the subscript $\Delta\varepsilon$ for the sake of readability. Equation (4.4) is a generalized linear eigenvalue problem which states that the output profile of an eigenstate $\vec{u}^{(i)}$ propagated through the scattering medium [left-hand side of Eq. (4.4)] is the same as the output profile for a propagation through air [right-hand side of Eq. (4.4)] up to the eigenvalue $\alpha^{(i)}$ (see Fig. 4.1 for a corresponding illustration). The latter is complex-valued and represents the additional attenuation and acquired phase when transmitted through the scattering medium rather than through air. Due to the similarity of the output profiles, irrespective of whether they scatter through a disordered sample or propagate ballistically through a homogeneous medium, these modes have been termed *scattering invariant modes (SIMs)*. Equation (4.4) can also be rewritten in terms of an ordinary eigenvalue problem

$$t_{\text{air}}^{-1} t_{\text{scat}}\vec{u}^{(i)} = \alpha^{(i)}\vec{u}^{(i)} \, , \tag{4.5}$$

which might be ill-posed as the inverse of the reference transmission matrix in air can be singular. In this case, a pseudo-inverse can again be employed (see Appendix C). Instead, we approximate the inverse matrix with its Hermitian conjugate assuming a close-to-unitary reference matrix to arrive at the following numerically stable eigenvalue problem:

$$t_{\mathrm{air}}^{\dagger} t_{\mathrm{scat}} \vec{u}^{\,(i)} = \alpha^{(i)} \vec{u}^{\,(i)} \,. \tag{4.6}$$

The SIMs resulting from this eigenvalue equation are then invariant in shape with respect to a forward propagation in the scattering medium followed by a backpropagation in air.

4.1 Scattering invariance in a strongly scattering medium and air

To experimentally realize this concept in the optical domain, a vector wavefront synthesizer was used to generate coherent fields with controllable amplitude, phase and polarization ellipse, while the transmitted light was recorded with a vector wavefront analyzer which measures the same quantities on a hexagonal 2D array of pixels [62]. The chosen scattering sample consisted of a layer of zinc oxide (ZnO) nanoparticles deposited on a glass slide, where a cleaned part of the glass slide was used as the scattering-free reference medium. In a first demonstration, a dense and hole-free scattering layer of length $L = 1.5\ \mu\mathrm{m} \approx 2\ell^* \approx 2\ell_s$ was used (since the ZnO particles correspond to sub-wavelength scatterers, the transport mean free path ℓ^* equals the scattering mean free path ℓ_s) and its transmission matrix t_{scat} was measured. Together with the measured transmission matrix t_{air} of the scatterer-free part of the glass slide, the SIMs were then obtained via Eq. (4.6).

Figures 4.2(a)-(d) show the experimentally measured transmitted fields of a SIM with $|\alpha| = 0.64$ projected through both media. As can bee seen, the fields transmitted through air ($\vec{E}_{\mathrm{air}}$) and through the scattering medium ($\vec{E}_{\mathrm{scat}}$) are very similar in both polarization components which can be quantified by a cosine similarity of $|\vec{E}^*_{\mathrm{scat}} \cdot \vec{E}_{\mathrm{air}}|/(|\vec{E}_{\mathrm{scat}}||\vec{E}_{\mathrm{air}}|) = 0.79$. Ideally, the output profiles of all SIMs should be perfectly correlated, however, the measured cosine similarity shown in Fig. 4.2(e) does not exceed 0.82 which is the result of experimental imperfections like noise and imperfect projection as well as the non-unitarity of the air transmission matrix $t_{\mathrm{air}}^{\dagger} \neq t_{\mathrm{air}}^{-1}$ in Eq. (4.6). In fact, the latter gives rise to a strong dependence of the cosine similarity on $|\alpha|$, where we find a monotonically increasing similarity with increasing $|\alpha|$. The experimentally obtained complex SIM eigenvalue spectrum is shown in Fig. 4.2(f), where the diffusive scattering of the ZnO layer leads to an almost isotropic distribution of the phase. The density of the eigenvalues gradually decays from the origin, which is in stark contrast to the eigenvalues obtained from a complex Gaussian random matrix with the same average transmission shown in Fig. 4.2(g). The latter are uniformly distributed inside a sharply bounded Ginibre disk [115] indicating that a random matrix model cannot capture the sample-specific details and correlations encoded in the actual scattering process.

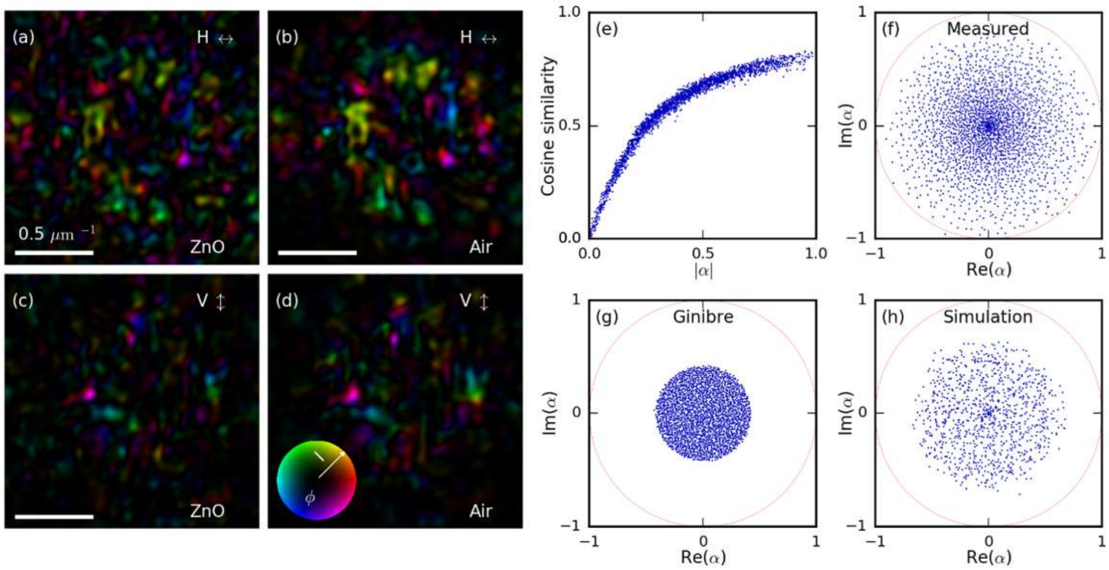

Figure 4.2: (a)-(d) Transmitted far-fields of a SIM with $|\alpha| = 0.64$ propagated (a,c) through a dense ZnO layer of length $L = 1.5\ \mu\text{m} \approx 2\ell^*$ or (b,d) through the same thickness of air, where (a,b) and (c,d) show the fields in the horizontal and vertical polarization component, respectively. The associated cosine similarity of these fields is 0.79. The color represents the phase and the brightness represents the amplitude [see inset in (d)]. (e) Cosine similarity of all SIM fields versus the magnitude of the corresponding SIM eigenvalues $|\alpha|$. (f) Experimentally obtained SIM eigenvalues in the complex plane. (g) Numerically obtained eigenvalue distribution of a random matrix from the Ginibre ensemble. (h) SIM eigenvalues from a numerical 2D simulation for a sample with a thickness of $L \approx \ell^*$.

In a next step, we therefore perform full-wave simulations within the numerical framework presented in Section 2.1. To mimic the openness of the experimental system, we use a scattering region which is not only longitudinally, but also transversally attached to leads featuring PMLs (instead of the hard walls) to absorb the out-scattered waves. The leads feature transverse homogeneous Dirichlet boundary conditions representing hard walls which enables us to use the basis of waveguide modes. Specifically, we use $k = 2\pi/\lambda = 1000.5\pi/W$ with W being the width of the scattering region and the longitudinal input and output lead. The scattering matrix is then calculated between the input and output port with the top and bottom lead serving as loss channels that resemble the finite numerical aperture of the objectives used in the experiment [116]. The length of the scattering region was scaled to feature the same ratio L/λ as in the experiment, i.e., $L = \lambda(L^{\text{exp}}/\lambda^{\text{exp}})$ with $L^{\text{exp}} = 2.1\ \mu\text{m}$ and $\lambda^{\text{exp}} = 633$ nm. The ZnO particles are modeled by circular scatterers with a refractive index of $n_{\text{scat}} = 2$, whose diameters are also scaled to match the ones in the experiment, i.e., $d_{\text{scat}} = \lambda(d^{\text{exp}}_{\text{scat}}/\lambda^{\text{exp}})$ with $d^{\text{exp}}_{\text{scat}} \approx 200$ nm. Since the ZnO nanoparticles tend to stick together, we mimic this by also using scatterers with a larger diameter of $d_{\mathrm{scat}}^{\mathrm{exp}} \approx 400$ nm, where we choose that every scatterer size fills out the same fraction of the total area of the scattering region. The experimentally used layer of ZnO particles is then modeled by a scattering region which is 40% filled with such scatterers. To simulate free space, we remove all the scatterers, leaving us with an empty scattering region in which waves could escape through the transversally added leads featuring PMLs that absorb the outgoing waves. The SIM eigenvalues obtained with this numerical setup are shown in Fig. 4.2(h), where we also observe a non-uniform radial distribution as in the experiment confirming that the non-uniformity of the eigenvalue spectrum stems from correlations which cannot be captured by a random matrix approach.

4.2 Scatterer avoidance in sparse scattering layers

To further understand the behavior of SIMs, let us first discuss the ideal case of an eigenvalue of $|\alpha^{(i)}| = 1$ which corresponds to an arbitrary phase shift, but no attenuation. In this case, the latter translates into $(1 + \Delta\varepsilon^2 |\tau_{\Delta\varepsilon}^{(i)}|^2)^{1/2} = 1$ and thus $|\tau_{\Delta\varepsilon}^{(i)}| = 0$. Even though $\tau_{\Delta\varepsilon}^{(i)}$ cannot be interpreted as the intensity stored inside the scatterers anymore due to the use of the finite difference quotient in Eq. (4.1), it still resembles the change of the transmission matrix for a change of the scatterer's permittivity. Therefore, eigenstates with a large $|\alpha^{(i)}|$ will be largely unaffected by a change of the permittivity and thus they tend to avoid scatterers if the sample is sparse enough to allow some light to pass unscattered.

To check whether SIMs corresponding to large eigenvalues, indeed, minimize the overlap with the scatterers, we experimentally and numerically use a second sparse scattering sample as reference (instead of air) to further highlight the versatility of the SIM concept. In this case, SIMs are wavefronts that produce the same output pattern when propagated through the principal and the reference scattering medium. Experimentally, a sparse scattering sample consists of two layers of sparsely-distributed ZnO nanoparticles separated by a transparent film of optical glue whose thickness is approximately 15 μm. For the reference medium, a different part of the same film was used. These scattering layers have been imaged under incoherent illumination, where the resulting scatterer configuration for both samples is indicated by the white dots in the insets in Figs. 4.3(a,b). The principal medium has a scatterer coverage of 11% and 32% at the front and back surface, respectively, resulting in an average coverage of 22%, while the reference medium has an average coverage of 15%. The transmission matrices for these scattering samples are then measured, where only a single polarization component is used. This is justified as the weak scattering in the sparsely-populated layers causes only weak polarization mixing which further allows a better comparison with the scalar description in the numerical simulations. The intensity profile of a SIM at the input and output interface of the principal and reference medium computed via the measured transmission matrices is shown in the insets in Figs. 4.3(a,b). Due to its large eigenvalue, the SIM clearly avoids the scatterers in both the principal and reference medium as expected. To quantify the behavior of all SIMs, the main panels in Figs. 4.3(a,b) show the experimentally obtained percentage of intensity of a SIM wave function that falls onto the scatterers as a function of the corresponding eigenvalue with the color indicating the associated cosine similarity. SIMs with high values of $|\alpha|$ hardly interact with scatters and are thus almost purely ballistic light, whereas SIMs with intermediate values of $|\alpha|$ do interact with scatterers, but still transmit by construction into similar output patterns. The decrease of the intensity on the scatterers for SIMs with $|\alpha|$ close to zero can be attributed to the experimental noise floor which becomes dominant for such low-transmitting states.

To verify the experimentally obtained results, we perform numerical simulations in which we model the double-layer structure by a rectangular scatterer with refractive index $n_{\text{glue}} = 1.5$ representing the film of optical glue with circular ZnO scatterers along its width on both sides. The thickness of the film is again scaled in order to match the experimental values, i.e., we set its length to $L_{\text{glue}} = \lambda(L_{\text{glue}}^{\text{exp}}/\lambda^{\text{exp}})$ with $L_{\text{glue}}^{\text{exp}} = 15\ \mu\text{m}$. Since the film features small thickness variations in the experiment, we also incorporate these by slightly modifying the shape of the rectangular scatterer. More precisely, we use a polygonal scatterer with 25 equidistant points along the width of the rectangle on both of its sides whose longitudinal position we randomly displace by $\delta L = r\lambda$ with r being a random number between 0 and 1. Since the ZnO particles at the output side are immersed in the optical glue film, we also take this into account by placing the circular scatterers at the output side inside the polygonal scatterer. As can be seen in the insets in Figs. 4.3(a,b), the experimental scatterer distributions show a clustering which we also incorporate by drawing random scatterer positions near the surface of the polygon around two cluster centers which we also choose randomly. As for the densely-filled scatterer samples, we use circular scatterers with diameters corresponding to $d_{\text{scat}}^{\text{exp}} = 200$ and 400 nm, where each scatterer size covers the same fraction of the surface of the corresponding layer and sample. To determine the overlap of a SIM with the scatterers, we – similar to the method used in the experiment – transversally read out its wave function right in front of (after) the circular scatterers at the input (output) side and integrate the corresponding intensity at the scatterer positions.

Figures 4.3(c,d) show the resulting statistics of SIM intensities on the scatterers which coincide very well with the experimentally obtained results in (a,b). SIMs with an eigenvalue close to one completely avoid the scatterers, with the corresponding results from the experiment showing slightly larger intensity values which can be attributed to the limited resolution in the experiment leading to a slight overestimation of the overlap. SIMs with smaller eigenvalues again interact with the scatterers featuring overlap values that are similar for very small and intermediate eigenvalues.

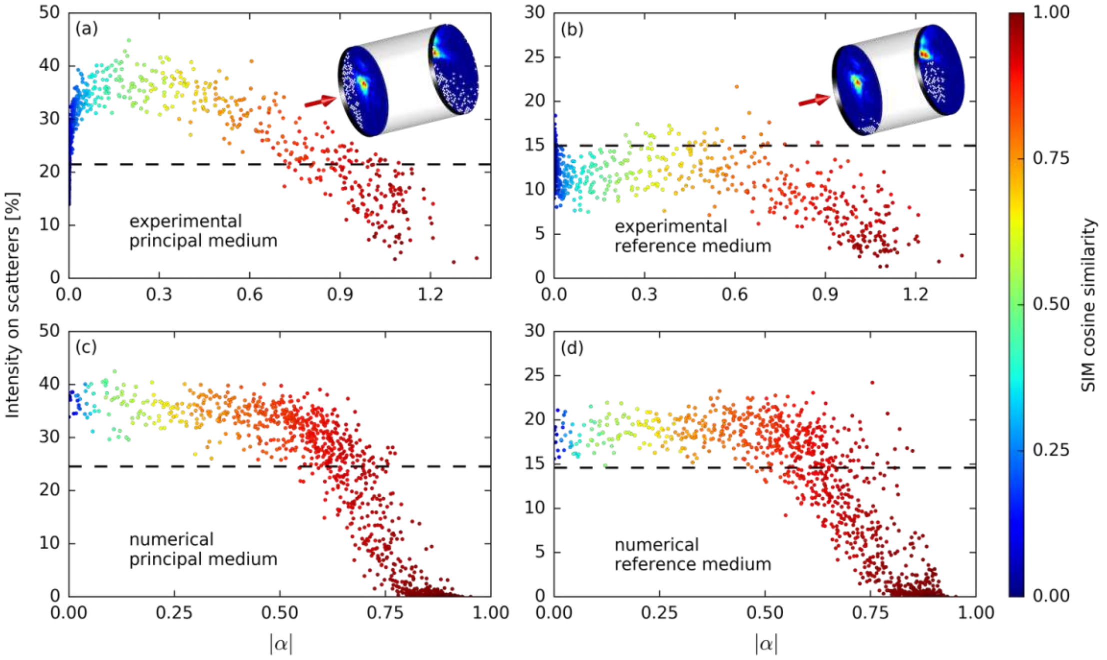

Figure 4.3: Overlap of the SIM intensity distributions with the scatterer positions in sparsely-occupied double-layer structures in dependence on the magnitude of the corresponding SIM eigenvalues. The color of the dots represents the cosine similarity of the fields propagated through both media and the respective surface coverages are indicated by the black dashed lines. (a,b) Experimentally obtained results on the (a) principal and (b) reference medium, where the insets show the experimentally measured intensity distribution of a SIM with a high value of $|\alpha|$ on both layers of the corresponding sample. There, the color represents the normalized intensity on each layer, with the positions of the scatterers indicated by white dots. (c,d) Corresponding results from a numerical simulation with similar surface coverages which coincide very well with the experimentally obtained results in (a,b) thus confirming that SIMs with a large eigenvalue minimize the overlap with the scatterers if the scattering samples are sparse enough.

To showcase the similarity of SIMs in the numerical simulations, Fig. 4.4 shows three SIMs with a high value of $|\alpha|$ in the numerically modeled double-layer structure. As can be seen, the output profiles of these SIMs transmitted through the principal and the reference medium are indistinguishable. Moreover, they clearly avoid the scatterer clusters (areas with scatterers are highlighted by a yellow frame) which gives rise to very similar intensity distributions also inside the polygonal film scatterer. However, the latter features different thickness variations in the principal and reference medium and thus the SIM wave functions are not identical, but very similar inside the film scatterers. Hence, SIMs with a large eigenvalue propagate purely ballistically in such sparse scattering layers.

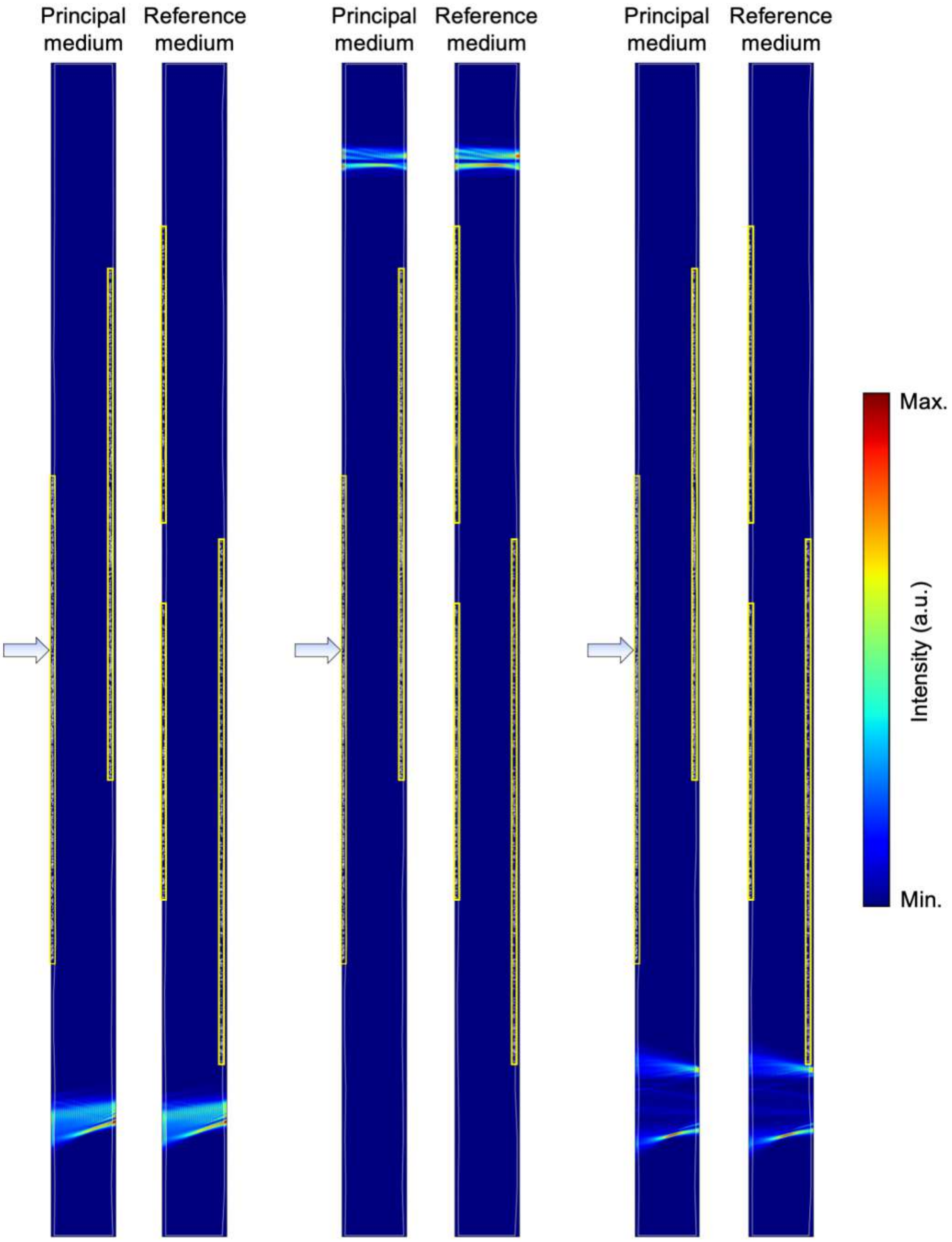

Figure 4.4: Numerically obtained intensity distributions of SIMs in a sparse principal and reference scattering medium. The shown wave functions correspond to the SIMs with the three largest eigenvalues which have been propagated through both media. The arrow indicates the input port and the yellow rectangles highlight the positions of the ZnO scatterer clusters. Due to their large eigenvalue, these SIMs avoid the ZnO scatterers leading to an identical wave function at the output of both media and a very similar intensity distribution inside the polygonal film scatterers.

4.3 Application to improve scanning fluorescence imaging

Based on the observations in the previous section, we show in Ref. [57] that also in case of a densely-filled principal medium and air as reference medium, SIMs are not only identical at the output side of both media, but still maintain a certain degree of correlation with the ballistic light (i.e., the wave propagated through air) also *inside* the scattering medium. Since current imaging techniques still rely on the filtering of ballistic light in order to obtain clear images [117–119], SIMs could thus be used to improve their performance. In fact, we will show in the following that SIMs can indeed improve scanning fluorescence imaging. For this purpose, we consider a scattering medium that consists of two dense scattering layers. Between these scattering layers, we assume a free space section with fluorophores randomly placed along the transverse line at $x = L/2$ which we want to image. Conventional fluorescence imaging approaches work by back-propagating a focal spot through the reference medium, i.e., by applying $t^\dagger_{\mathrm{air}}(L/2)$ to eigenstates of Eq. (1.39), and injecting the resulting wavefronts into the scattering medium. To improve the imaging performance using SIMs, we rewrite the SIM operator in Eq. (4.5) using its spectral decomposition

$$t_{\mathrm{scat}}(L) = t_{\mathrm{air}}(L)\, U \mathrm{diag}(\{\alpha\}) U^{-1}\,, \tag{4.7}$$

where U is a matrix that contains the SIM eigenvector coefficients in the chosen basis. Instead of using the reference medium for back-propagation, we now assume that SIMs are correlated with the ballistic propagation through air and thus acquire half of the phase at $x = L/2$ if the scattering is homogeneous. Furthermore, neglecting multiple reflections between the two scattering layers lets us assume that the intensity decrease in the middle of the scattering medium can be described by $\sqrt{|\alpha|}$. Putting everything together, we can thus approximate the transmission matrix into the plane at depth $x = L/2$ by the square-root of the total transmission matrix, i.e.,

$$t_{\mathrm{scat}}(L/2) = t_{\mathrm{air}}(L/2)\, U \mathrm{diag}\left(\sqrt{\{\alpha\}}\right) U^{-1}\,. \tag{4.8}$$

Note that the SIM eigenvalues are complex and in order to avoid jumps in the retrieved phase values we set the branch cut of the square-root in Eq. (4.8) to the angle in the complex plane at which the SIM eigenvalue distribution has its lowest density. Back-propagating focal spots $E_{\mathrm{foc}}(x = L/2, y)$, i.e., eigenstates of Eq. (1.39), via $t^\dagger_{\mathrm{scat}}(L/2)$ then results in corrected input focusing fields. Notably, these fields feature a higher correlation with the desired images inside the scattering medium compared to conventional images resulting from uncorrected ballistic light (see below). This SIM correction procedure is now applied to scattering layers consisting of small circular obstacles with a diameter of $d_{\mathrm{scat}} = \lambda/6$ and a refractive

L/ℓ^*	$C_{\text{uncorr.}}$ (sd)	C_{SIM} (sd)
1.12	0.903 (0.031)	0.956 (0.018)
1.82	0.778 (0.069)	0.859 (0.073)
3.14	0.740 (0.079)	0.809 (0.082)

Table 4.1: Mean correlation coefficients and standard deviations (sd) for scattering systems with different transport mean free paths. Here, C_{SIM} denotes the image correlation with SIM-corrected focusing states which is improved compared to the correlation $C_{\text{uncorr.}}$ using uncorrected fields. Each correlation value is an average over 100 different scattering layer configurations and 20 different fluorescence functions, which we choose to consist of three randomly chosen spots of width $\lambda/2$ in the imaging plane. The first two rows correspond to systems with a filling fraction of 5% and 10%, respectively, whereas the systems in the last row consist of two concatenated layers with 5% filling fraction in front of and after the imaging plane.

index of $n_{\text{scat}} = 1.44$. To characterize the scattering strengths of our layers, we also calculate the transport mean free path ℓ^* which equals the scattering mean free path, i.e., $\ell^* \approx \ell_s$, due to the sub-wavelength size of the scatterers. To reduce computation time, we – in contrast to the results presented above – use a waveguide geometry (with hard side walls rather than the transverse PMLs used before) and $k = 100.5\pi/W$, i.e., 100 propagating modes. To determine the pixel values of our fluorescence images, we numerically inject all the corrected and uncorrected focusing states and calculate the overlap of their spatial intensity distributions with the fluorescence function at the imaging plane. The latter consists of 3 randomly chosen spots of width $\lambda/2$, where we additionally use Gaussian window functions around the ideal focusing spots. These window functions simulate the diffusion cones resulting from spatially localized input states thus simulating the effect of the pinhole in confocal microscopy. Their width is chosen such that 5σ equals the penetration depth into the focusing plane, i.e., $L/2$. The pixel values obtained in this way are then used for the calculation of the Pearson correlation coefficients. Table 4.1 contains the resulting correlation coefficients for different scattering strengths showing that the SIM correction yields an improvement compared to the uncorrected fields up to 4 transport mean free paths.

For more strongly scattering systems, we find that the SIM eigenvalue distributions in the complex plane lose their asymmetry with the latter reflecting the existence of ballistic contributions. More specifically, the eigenvalues of some SIMs revolve multiples of 2π in the complex plane during propagation and thus their phase cannot be predicted by the argument of their eigenvalues only. To visualize this, Fig. 4.5 shows the SIM eigenvalue distributions for layers with different filling fractions, in which the refractive index of the scatterers is increased gradually from 1 to 1.44. For $n_{\text{scat}} = 1$, the principal medium equals the reference medium and thus $\alpha^{(i)} = 1$ for all SIMs since no relative phase is acquired or amplitude is lost.

TU Bibliothek WIEN Your knowledge hub
Die approbierte gedruckte Originalversion dieser Dissertation ist an der TU Wien Bibliothek verfügbar.
The approved original version of this doctoral thesis is available in print at TU Wien Bibliothek.

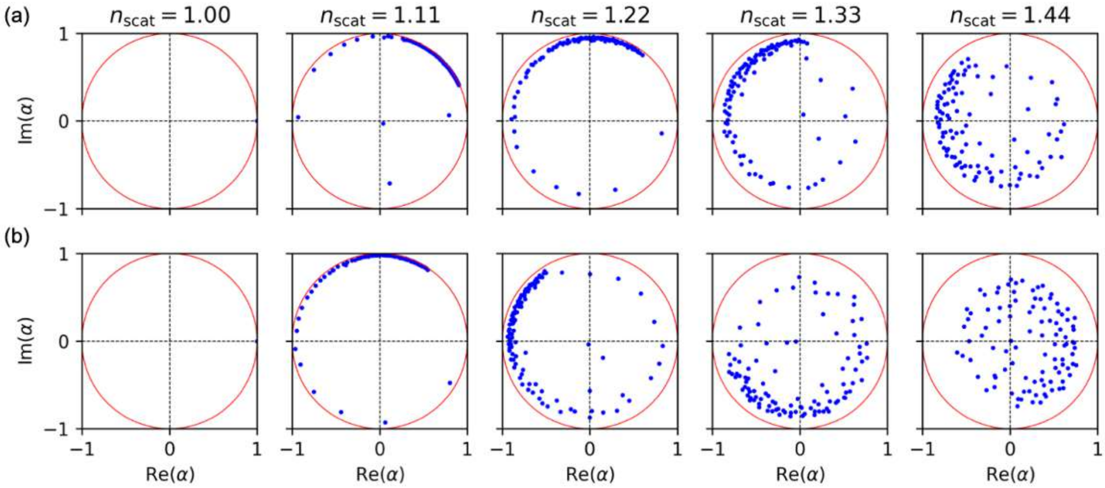

Figure 4.5: Evolution of the SIM eigenvalue spectrum in the complex plane for an increasing refractive index n_{scat} of the circular scatterers in the two scattering layers with a filling fraction of (a) 5% and (b) 10%. The corresponding scattering strengths of these systems for $n_{\mathrm{scat}} = 1.44$ can be found in the first two rows of Table 4.1.

Increasing the refractive index then causes the eigenvalues to rotate along the unit circle in the complex plane. Note that a further increase leads to eigenvalues which revolve multiples of 2π or pass through zero causing a loss of the distribution's asymmetry with increasing scattering strength. To reduce the number of eigenvalues which revolve multiples of 2π, one could use a homogeneous reference medium with the same effective refractive index as the scattering medium instead of air. This would lead to a smaller relative phase between the fields propagated through both media and thus to a slower rotation of the eigenvalue cloud.

Up to now, we have only considered 2D scattering setups, however, in Ref. [57] we also employ a tight-binding model on a hexagonal grid and obtain similar imaging improvements in three dimensions. In fact, the SIM correction even outperformed the conventional uncorrected method up to 9 transport mean free paths which can be attributed to a correction scheme slightly different from the one outlined above. Unlike in 2D, the 3D simulations show a strong dependence of the fidelity and phase of the SIMs on the phases of the corresponding eigenvalues. Rather than performing a correction based on the square-root of the SIM eigenvalues as in the 2D case, one can now use heuristically found dependencies to correct their amplitudes and phases. The obtained improvements of the correlation values compared to the uncorrected fields are similar to the 2D case, but persist up to scattering strengths of 9 transport mean free paths (a table with the correlation values of the 3D simulation can be found in Ref. [57], where the corresponding supplementary material contains all the details about the numerical implementation of the tight-binding model). To demonstrate the improvements resulting from the SIM correction approach in 3D,

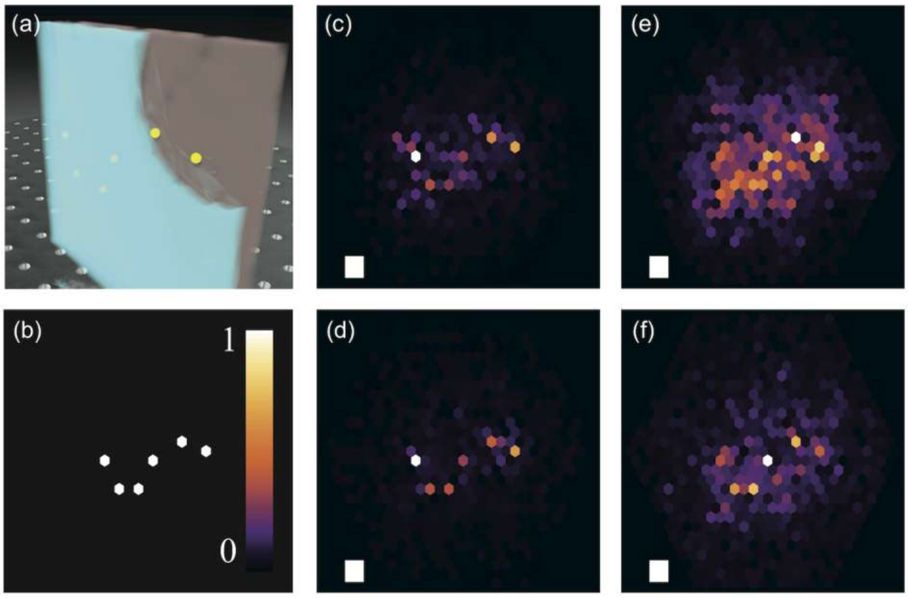

Figure 4.6: (a) Sketch of the numerical setup used in the 3D simulations in which fluorescent particles (yellow dots) are sandwiched between two scattering layers of thickness $L/2$ (one is partially removed for clarity). (b) Plot of the fluorescent object in the imaging plane which consists of six point-like particles. The inset shows the intensity color scale used in (c)-(f). (c) and (d) show the uncorrected and SIM-corrected image for a system thickness of $L \approx 5.4\ell^*$, respectively, while (e) and (f) show the uncorrected and corrected image for a system of length $L \approx 7.1\ell^*$. The white squares indicate the wavelength in the simulation.

Fig. 4.6 shows a sketch of the simulation setup together with the obtained images for the uncorrected and corrected case for scattering media with different thicknesses. Note that the uncorrected image is already heavily distorted even for the weaker scattering system in Fig. 4.6(e).

4.4 Conclusion

SIMs are based on the transmission matrix whose study has already led to numerous insights and has greatly extended our understanding of complex wave scattering, where much research has been done on the transmission eigenchannels [120–125], i.e., the eigenstates of $t_{\text{scat}}^{\dagger} t_{\text{scat}}$, and their statistics [126–128]. By further generalizing the eigenvalue problem of the GWS operator introduced in the previous chapter, we obtain a SIM operator that is structurally very similar to the operator of the transmission eigenchannels. However, the corresponding SIMs feature the remarkable property that their output profile is identical up to a global phase and amplitude if they are propagated through air or through a strongly scattering medium. In sparse scattering layers, we then show that SIMs embody the defining feature of ballistic light since they tend to avoid scatterers. For imaging applications, the ballistic contributions of light are essential and despite the rapid progress in advanced optical imaging techniques [129–136], accessing them is still very difficult, especially in optically thick media where they are exponentially rare [117]. Since SIMs still maintain a certain degree of correlation with ballistic light even inside a dense scattering medium, we show in a first demonstration how these special states of light can be used to improve scanning fluorescence imaging in two and three dimensions. In a further study, we have already shown that they can also be used to customize the angular memory effect in order to go beyond the conventional memory effect [137]. Another possible future application could exploit the SIM's stability with respect to the presence of scatterers to overcome imperfections in optical elements if the corresponding transmission matrix of the perfect optical element has been used as reference in their construction. Moreover, in analogy to the super-princicpal modes [44], an extension of the SIMs invariance property to a broader range of parameters, i.e., to more than two media, could also be the scope of future research. Together with the presented results, the versatility of the SIM concept due to the possible use of different scattering, transmission or reflection matrices in the SIM operator makes us believe that SIMs also have the potential to improve current state-of-the-art techniques in optical as well as in ultrasound imaging.

Having explored different generalizations of the Wigner-Smith concept, we return to the roots in the next chapter and revisit the concept of time-delay. More specifically, we investigate the mean time-delay of waves inside complex scattering media and encounter a surprising invariance property that holds in all transport regimes.

Die approbierte gedruckte Originalversion dieser Dissertation ist an der TU Wien Bibliothek verfügbar.
The approved original version of this doctoral thesis is available in print at TU Wien Bibliothek.
TU Bibliothek
WIEN Your knowledge hub

Chapter 5

Mean path length invariance beyond the diffusive regime[17]

In this chapter, we utilize the concept of time-delay to verify the existence of a surprising invariance property in wave scattering. More specifically, although states with well-defined time-delays exist [45] (which can, e.g., be used for optimal energy storage [50]), we show numerically and experimentally that the *mean* time-delay of waves is invariant in all transport regimes of disorder scattering as well as in structured materials featuring band-gaps.

The so-called *mean path length invariance* is a fundamental result in the field of diffusive random walks and states that the mean path length of trajectories under isotropic uniform incidence is entirely independent of the parameters entering the random walk such as, e.g., the transport mean free path ℓ^* and the scattering mean free path ℓ_s (see Appendix D). In fact, no matter how convoluted trajectory paths might be, their mean length (corresponding to their first exit of the considered bounded domain) only depends on the systems geometry (see Fig. 5.1). More precisely, the mean path length $\langle s \rangle$ only depends on the ratio of the system's area A to its external boundary C through which the particles can enter and exit the system, i.e., [138]

$$\langle s \rangle = v_t \langle t \rangle = \pi \frac{A}{C}\,, \tag{5.1}$$

where $\langle t \rangle$ is the corresponding mean time and v_t is the constant trajectory velocity. Equation (5.1) is valid in two dimensions, whereas a similar relation also holds in three dimensions, $\langle s \rangle = 4V/\Sigma$ with V and Σ being the volume and the external surface of the considered domain, respectively [138]. This invariance property generalizes the mean chord length theorem valid in the ballistic limit of straight line trajectories with infinite mean free path [139], and it has further been extended to

---

[17] The results presented in this chapter were obtained in collaboration with Matthieu Davy from the Université de Rennes 1 and Sylvain Gigan from the Laboratoire Kastler Brossel. The theoretical analysis was carried out by Matthieu Davy, myself, Stefan Rotter and Sylvain Gigan. The numerical simulations were performed by myself under the supervision of Stefan Rotter, whereas the experiments were conducted by Matthieu Davy. Parts of the text and the figures in this chapter have been taken from our joint publication [58].

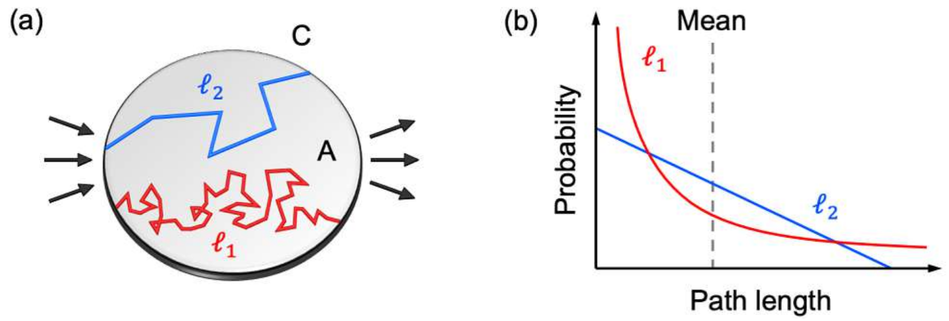

Figure 5.1: (a) Random walk trajectories inside a two-dimensional bounded domain of circular shape whose mean length is independent of the characteristic (scattering) mean free path ℓ and only depends on the ratio of the domain's area A to its circumference C [see Eq. (5.1)]. The two presented trajectories correspond to different mean free paths ℓ_1 (red) and ℓ_2 (blue), where $\ell_2 > \ell_1$. (b) Probability distribution of path lengths, which strongly depends on the mean free path, but whose mean value is invariant (reproduced from Ref. [54]).

trajectories starting from inside the considered domain [140]. Furthermore, it was shown that a similar invariance property holds in case of disconnected subdomains with area A' of the total area A in which case the corresponding mean path length is given by Eq. (5.1) with A replaced by A' [141]. Since the invariance property Eq. (5.1) applies to all research fields where diffusion processes or random walks occur, it leads to a broad range of applications covering nuclear physics [142], solar energy harvesting [143] as well as the movement of bacteria [144].

Recently, it was shown that this invariance property is not a peculiar feature of classical random walks, but also applies to wave scattering in disordered systems in which case the trajectory velocity has to be replaced by the wave's energy transport velocity [53]. This result is far from obvious since coherent wave effects can lead to very strong deviations from any of the transport regimes that particles can be in. Consider here, e.g., the regime of Anderson localization [145–147], in which an exponential suppression of transmission leads to a complete halt of wave diffusion, or the formation of a band gap in a photonic crystal [148], to cite just two genuinely wave-like phenomena that both rely on wave interference. The natural question to ask at this point is whether any such effects going beyond a trajectory-based description may lead to a violation of the mean path length invariance since they clearly fall outside the scope of both the mean chord length theorem and a random walk picture. More specifically, since both Anderson localization and a band gap prevent incident waves from propagating inside the scattering region, one naturally expects that the mean path length invariance should break down in these cases. However, numerical simulations suggest that the invariance property may also hold in the localized regime [53].

Experimentally, this path length invariance has recently been verified in the diffusive regime by using an optical setup and a colloidal solution of microbeads in water. The turbidity of this liquid was then changed from nearly transparent to very opaque by varying the concentration and size of the particles. The results confirm that the mean path length of isotropically incoming light stays, indeed, unchanged over nearly two orders of magnitude in scattering strength [54]. However, an experimental verification in the localized regime and in band gap materials remains open. In the following, we therefore close this gap by using an experimental setup that allows the verification of the mean path length invariance in all transport regimes, i.e., in the ballistic ($L \lesssim \ell_s$), diffusive ($\ell^* \lesssim L \lesssim \xi$ with ξ being the localization length) and localized ($L \gtrsim \xi$) regime [10], as well as in band gap materials like photonic crystals.

To analytically derive this invariant length in a wave mechanical description, we follow Ref. [53] and make use of Eq. (1.24) which states that the average dwell time associated with a scattering process is directly linked to the DOS inside the scattering region, i.e.,

$$\langle \tau_d(\omega) \rangle = \frac{2\pi}{N_{\text{in}}(\omega)} \rho(\omega) \,. \tag{5.2}$$

The key ingredient is now the so-called *Weyl law* which states that the DOS satisfies a universal law in the asymptotic limit of $\omega \to \infty$ that just depends on the geometry of the system, but not on the specific details of the considered scattering potential. In this limit, the DOS can be written as [149, 150]

$$\rho(\omega) = \frac{A\omega}{2\pi c^2} \,. \tag{5.3}$$

Assuming a straight two port waveguide similar to the one in Fig. 3.1, $N_{\text{in}}(\omega) = 2N(\omega)$ with $N(\omega)$ being the ω-dependent integer number of propagating modes at each port. In a waveguide of width W, the latter is given by the step-function $N(\omega) = \lfloor \omega W / c\pi \rfloor$. To obtain a smooth function of frequency, we smoothen this expression over one mode interval resulting in $N(\omega) \approx \omega W/\pi c - 0.5$. Inserting this and Eq. (5.3) into Eq. (5.2) finally yields

$$s_{\text{theo}}(\omega) = c\langle \tau_d(\omega) \rangle \approx \pi \frac{A}{C} \,, \tag{5.4}$$

with $C = 2W$ which coincides with Eq. (5.1) for $v_t \to c$. Making use of the close relation between the dwell time and the time-delay operator, i.e., $Q_d \approx Q_\omega^{(S)}$, Eq. (5.4) has been verified in numerical simulations via $\langle \tau_d(\omega) \rangle = \text{Tr}(Q_\omega^{(S)})/[2N(\omega)]$ in the ballistic and the diffusive as well as in the localized regime in Ref. [53]. Therein, a straight waveguide geometry with a varying number of metallic impenetrable circular scatterers was used. The obtained results satisfy the analytical prediction very accurately thus confirming that the trajectory-based result Eq. (5.1) is also valid in disordered wave scattering. In the localized regime, however, the large number of

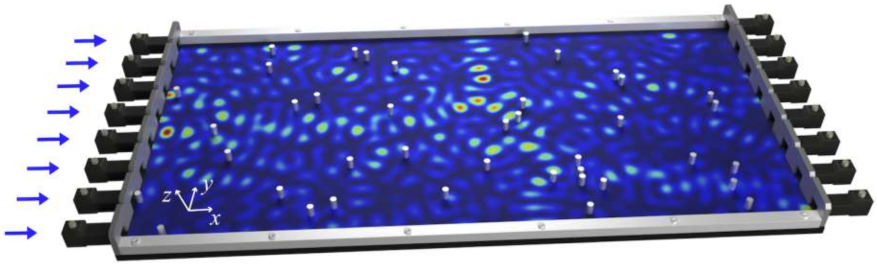

Figure 5.2: Sketch of the experimental setup, where 40 metallic scatterers are randomly placed inside the scattering region to increase the scattering strength of the system (the top plate is not shown in order to visualize the interior). The embedded intensity distribution corresponds to the highest transmitting transmission eigenstate in this scattering configuration obtained from a numerical simulation with the blue arrows indicating the input leads of the waveguide.

impenetrable scatterers leads to a deviation from Eq. (5.3) since the DOS is reduced close to their boundaries. To account for this, the following correction proposed by Weyl must be employed [150, 151]

$$\rho(\omega) = \frac{1}{2\pi c}\left(\frac{A\omega}{c} + \frac{C-B}{2}\right). \tag{5.5}$$

This next-order correction also involves the internal boundaries B which consist of the waveguide walls and the boundaries of the impenetrable scatterers. Hence, the internal boundaries B are very different compared to the external boundaries C through which the waves scatter in and out. Due to the smaller number of scatterers, this correction term is negligible in the ballistic and diffusive regime, but cannot be neglected in the localized regime [53]. The resulting mean path length averaged over all scattering channels then reads

$$s_{\text{theo}}(\omega) = \frac{1}{2N(\omega)c}\left(A\omega + \frac{C-B}{2}c\right). \tag{5.6}$$

For the experimental verification of this relation, we use the microwave waveguide depicted in Fig. 5.2 whose scattering region is formed by an effectively two-dimensional cavity of length $L = 0.5$ m and width $W = 0.25$ m with two arrays of 8 leads of length $l = 38$ mm and width $w = 15.79$ mm attached on the left and right interface of the waveguide. Each lead supports a single propagating mode between 9.493 and 18.986 GHz which can be excited by an antenna that is fully coupled to the cavity, resulting in $N = 8$ input states from one side of the cavity. Using the array of antennas on the other side of the waveguide, this setup enables the measurement of the $N \times N$ transmission matrix $t(\omega)$. Note that in contrast to open waveguides (like the one in Fig. 3.1, in which the single-channel leads of the geometry in Fig. 5.2 are replaced by a single multi-channel lead with the same width as the scattering region on each side), the metallic spacings between the left and right lead interfaces induce strong internal reflections causing the transmission matrix to be not diagonal in the absence of scatterers. To increase the scattering strength from the ballistic to the diffusive and the localized regime, we then place up to 280 metallic aluminum cylinders inside the scattering region.

To determine the mean time-delay in this setup, the measurement of the full $2N \times 2N$ scattering matrix including the reflection matrices on both sides of the sample would be required. Since such a measurement is experimentally highly challenging, most setups only provide access to either the one-sided reflection or transmission matrix. To overcome this difficulty, we show that in case of non-absorbing systems (featuring a unitary scattering matrix), the mean time-delay can also be obtained by means of the transmission matrix alone. The relation between the mean path length obtained with the time-delay operator containing the full scattering matrix $q_\omega^{(S)}(\omega)$ and the operator featuring only the transmission matrix $q_\omega^{(t)}(\omega)$ reads

$$s[q_\omega^{(S)}(\omega)] = s[2q_\omega^{(t)}(\omega)]\,, \tag{5.7}$$

where $s(O) = c\mathrm{Re}[\mathrm{Tr}(O)/(2N)]$ is the mean length obtained with an operator O. To analytically prove the above simple relation, which extends the decomposition of the DOS into a superposition of contributions from each transmission eigenchannel [122], we rewrite Eq. (5.7) as

$$\mathrm{Tr}(q_\omega^{(S)}) = 2\mathrm{Re}[\mathrm{Tr}(q_\omega^{(t)})]\,. \tag{5.8}$$

Next, assuming unitarity, i.e., $S^{-1} = S^\dagger$, we can write $q_\omega^{(S)}$ as

$$q_\omega^{(S)} = Q_\omega^{(S)} = \begin{pmatrix} -ir^\dagger \frac{dr}{d\omega} - it^\dagger \frac{dt}{d\omega} & -ir^\dagger \frac{dt'}{d\omega} - it^\dagger \frac{dr'}{d\omega} \\ -it'^\dagger \frac{dr}{d\omega} - ir'^\dagger \frac{dt}{d\omega} & -ir'^\dagger \frac{dr'^\dagger}{d\omega} - it'^\dagger \frac{dt'^\dagger}{d\omega} \end{pmatrix}, \tag{5.9}$$

where its trace evaluates to

$$\mathrm{Tr}(Q_\omega^{(S)}) = \mathrm{Tr}\left(-it^\dagger \frac{dt}{d\omega} - it'^\dagger \frac{dt'^\dagger}{d\omega} - ir^\dagger \frac{dr}{d\omega} - ir'^\dagger \frac{dr'^\dagger}{d\omega}\right). \tag{5.10}$$

To calculate the first term appearing in the trace, we use the singular value decomposition of the transmission matrix $t = U\Sigma V^\dagger$. Here, $U = (\vec{u}_1, \vec{u}_2, \ldots, \vec{u}_N)$ and $V = (\vec{v}_1, \vec{v}_2, \ldots, \vec{v}_N)$ are the matrices which contain column-wise the left and right singular vectors of t, and $\Sigma = \mathrm{diag}(\{\sigma_n\})$ is a diagonal matrix containing the singular values σ_n. Making further use of $U^\dagger U = \mathbb{1}$ and $V^\dagger V = \mathbb{1}$ and the invariance of the trace with respect to cyclic permutations, we can write

$$\mathrm{Tr}\left(-it^\dagger \frac{dt}{d\omega}\right) = \mathrm{Tr}\left(-i\Sigma^2 U^\dagger \frac{dU}{d\omega} - i\Sigma^2 \frac{dV^\dagger}{d\omega} V - i\Sigma \frac{d\Sigma}{d\omega}\right). \tag{5.11}$$

Making again use of $V^\dagger V = \mathbb{1}$, we can rewrite the second term as $\frac{dV^\dagger}{d\omega}V = -V^\dagger\frac{dV}{d\omega}$. Since the singular values σ_n of t are given by the square-root of the eigenvalues τ_n of $t^\dagger t$ and $tt^\dagger$, i.e., $\sigma_n = \sqrt{\tau_n}$, we arrive at

$$\mathrm{Tr}\left(-it^\dagger\frac{dt}{d\omega}\right) = \sum_n \tau_n \frac{d\vartheta_n^{(t)}}{d\omega} - i\sigma_n^{(t)}\frac{d\sigma_n^{(t)}}{d\omega}\,, \tag{5.12}$$

where we have defined the transmission eigenchannel delay times as

$$\frac{d\vartheta_n^{(t)}}{d\omega} \equiv \frac{1}{i}\left(\vec{u}_n^{(t)\dagger}\frac{d\vec{u}_n^{(t)}}{d\omega} - \vec{v}_n^{(t)\dagger}\frac{d\vec{v}_n^{(t)}}{d\omega}\right). \tag{5.13}$$

Since the left and right singular vectors for the different transmission and reflection matrices are not identical, we have introduced a superscript denoting the matrix a singular vector (or singular value) belongs to. To calculate the remaining terms in Eq. (5.10), Eqs. (1.5)-(1.8) can be used to deduce relations between the singular vectors of the different matrices. For the right singular vectors $\vec{v}_n$, Eq. (1.5) yields

$$t^\dagger t + r^\dagger r = \mathbb{1} \quad\Rightarrow\quad \vec{v}_n^{(t)} = \vec{v}_n^{(r)} \equiv \vec{v}_n^{(t,r)}\,, \tag{5.14}$$

$$t'^\dagger t' + r'^\dagger r' = \mathbb{1} \quad\Rightarrow\quad \vec{v}_n^{(t')} = \vec{v}_n^{(r')} \equiv \vec{v}_n^{(t',r')}\,. \tag{5.15}$$

Due to Eq. (1.7), the left singular vectors $\vec{u}_n$ are related as follows

$$tt^\dagger + r'r'^\dagger = \mathbb{1} \quad\Rightarrow\quad \vec{u}_n^{(t)} = \vec{u}_n^{(r')} \equiv \vec{u}_n^{(t,r')}\,, \tag{5.16}$$

$$t't'^\dagger + rr^\dagger = \mathbb{1} \quad\Rightarrow\quad \vec{u}_n^{(t')} = \vec{u}_n^{(r)} \equiv \vec{u}_n^{(t',r)}\,. \tag{5.17}$$

Reciprocity [see Eq. (1.9)] leads to $t' = t^T$, which implies that t and t' share the same eigenvalues. Thus, $\sigma_n^{(t)} = \sigma_n^{(t')}$ and since $\sigma_n^{(t)^2} = \tau_n$ it follows that $\sigma_n^{(r)^2} = \rho_n = 1 - \tau_n = 1 - \tau_n' = \rho_n' = \sigma_n^{(r')^2}$. Setting up the remaining terms in Eq. (5.10) containing t', r and r' in a similar way and inserting them together with Eq. (5.12) into Eq. (5.10) yields

$$\begin{aligned}\mathrm{Tr}(Q_\omega^{(S)}) = \sum_n \frac{1}{i}\Bigg[&\vec{u}_n^{(t,r')\dagger}\frac{d\vec{u}_n^{(t,r')}}{d\omega} - \vec{v}_n^{(t,r)\dagger}\frac{d\vec{v}_n^{(t,r)}}{d\omega}\\ &+ \vec{u}_n^{(t',r)\dagger}\frac{d\vec{u}_n^{(t',r)}}{d\omega} - \vec{v}_n^{(t',r')\dagger}\frac{d\vec{v}_n^{(t',r')}}{d\omega}\Bigg]\\ &- i\left[\frac{d\sigma_n^{(t,t')^2}}{d\omega} + \frac{d\sigma_n^{(r,r')^2}}{d\omega}\right],\end{aligned} \tag{5.18}$$

where we have already used the relations (5.14)-(5.17). Due to the assumed unitarity of S, the operator $Q_\omega^{(S)}$ is Hermitian and thus the imaginary part of the corresponding eigenvalues given by the last term in Eq. (5.18) has to vanish. Using $\tau_n^{(\prime)} + \rho_n^{(\prime)} = 1$ (following from the unitarity of S) then indeed yields

$$\frac{d\sigma_n^{(t,t')^2}}{d\omega} + \frac{d\sigma_n^{(r,r')^2}}{d\omega} = \frac{d(\tau_n^{(\prime)} + \rho_n^{(\prime)})}{d\omega} = 0\,. \tag{5.19}$$

Making use of the similarity of certain singular vectors as indicated by their superscripts, Eq. (5.18) can be written in two different ways:

$$\begin{aligned} \mathrm{Tr}(Q_\omega^{(S)}) &= \sum_n \frac{d\vartheta_n^{(t)}}{d\omega} + \frac{d\vartheta_n^{(t')}}{d\omega} \\ &= \sum_n \frac{d\vartheta_n^{(r)}}{d\omega} + \frac{d\vartheta_n^{(r')}}{d\omega}\,. \end{aligned} \tag{5.20}$$

Finally, we want to connect this result to the trace of $q_\omega^{(t)}$ which can be simplified as follows:

$$\begin{aligned} \mathrm{Tr}(q_\omega^{(t)}) &= \left(-it^{-1}\frac{dt}{d\omega}\right) \\ &= \mathrm{Tr}\left(-iU^\dagger\frac{dU}{d\omega} + iV^\dagger\frac{dV}{d\omega} - i\Sigma^{-1}\frac{d\Sigma}{d\omega}\right) \\ &= \sum_n \frac{d\vartheta_n^{(t)}}{d\omega} - i\frac{d\ln(\sigma_n^{(t)})}{d\omega}\,. \end{aligned} \tag{5.21}$$

Note that the eigenchannel delay times $d\vartheta_n^{(t)}/d\omega$ correspond to the time-delays of the transmission eigenchannels which are different from the real part of the eigenvalues of $q_\omega^{(t)}$. However, the invariance of the trace under similarity transformations used in the derivation above keeps their sum the same. To further simplify Eq. (5.20), we again employ $t' = t^T$ to rewrite $q_\omega^{(t')} = t'^{-1}q_\omega^{(t)T}t'$. This shows that $q_\omega^{(t')}$ can be written as a similarity transformation of $q_\omega^{(t)}$ which implies that they share the same eigenvalues resulting in the same trace. Since reciprocity does not relate the reflection matrices r and r', no direct relation between the eigenvalues of $q_\omega^{(r)}$ and $q_\omega^{(r')}$ exists, but unitarity still enforces that the sum of the corresponding eigenchannel delay times in transmission and reflection is equal [see Eq. (5.20)]. With the help of Eq. (5.21) and similar expressions for $q_\omega^{(t')}$, $q_\omega^{(r)}$ and $q_\omega^{(r')}$, Eq. (5.20) can then finally be written as

$$\begin{aligned} \mathrm{Tr}(Q_\omega^{(S)}) &= \mathrm{Re}[\mathrm{Tr}(q_\omega^{(r)}) + \mathrm{Tr}(q_\omega^{(r')})] \\ &= \mathrm{Re}[\mathrm{Tr}(q_\omega^{(t)}) + \mathrm{Tr}(q_\omega^{(t')})] \\ &= 2\mathrm{Re}[\mathrm{Tr}(q_\omega^{(t)})]\,. \end{aligned} \tag{5.22}$$

This proves that the mean path length can be determined by transmission measurements only.

5.1 Disordered systems

To verify the invariance of the mean path length, we consider the system depicted in Fig. 5.2 for a varying number of scatterers. Figures 5.3(a) and (b) show the mean path length obtained via $\langle s[2q_\omega^{(t)}(\omega)]\rangle$ in a single scattering configuration averaged over a certain frequency range (denoted by the angle brackets) for each number of scatterers in comparison with the corresponding theoretical prediction $\langle s_{\text{theo}}(\omega)\rangle$ from the next-order corrected Weyl law Eq. (5.6). The scattering area is $A = LW + 2Nlw - N_{\text{scat}}\pi r_{\text{scat}}^2$ with N_{scat} being the number of impenetrable metallic scatterers of radius r_{scat}. The external boundaries are given by $C = 2Nw$ and the internal boundaries are $B = 2L + N_{\text{scat}}2r_{\text{scat}}\pi + 4Nl + 2(N-1)\Delta w$ with Δw being the width of the metallic spacings between the leads. The theoretical estimate and the numerically obtained values for the mean path length are averaged over the frequency range of 11-13 GHz in the ballistic and diffusive regime. In the localized regime, we use the slightly smaller interval of 11-12 GHz since the signatures of localization are more pronounced in this range. Using these frequency intervals, the theoretical mean path length decreases from 2.05 m for an empty cavity to 1.76 m for a sample with 280 metallic cylinders. It is also worth noting that the theoretical mean path length in the empty cavity is $\langle s_{\text{theo}}(\omega)\rangle \sim 4L$ which strongly exceeds the corresponding value in an open waveguide with the same dimensions $\langle s_{\text{theo}}(\omega)\rangle = \pi L/2$ [53]. This enhancement is a result of the metallic spacings between the leads at the left and right interfaces of the cavity which give rise to states with very long delay times. As shown in the supplementary material of [58], these states correspond to bouncing orbits between the top and bottom metallic walls of the cavity (in y-direction).

For the numerical verification of the mean path length invariance, we model the experimental waveguide by adapting the two-port system introduced in Section 2.1 to a $2N$-port system with N leads attached on each side of the cavity (separated by metallic spacings featuring PEC boundary conditions), again terminating the lead ends with PMLs. Since the leads only support a single mode, i.e, the TE_{10} mode, in the considered frequency interval, the transmission matrix t_{mn} describes the transmission from lead n at the input side to lead m at the output side. Figure 5.3(a) depicts the mean path lengths $\langle s[2q_\omega^{(t)}(\omega)]\rangle$ obtained in the numerical simulations in absence of absorption (black crosses) which are in perfect agreement with the Weyl prediction (red line). There, even the small reduction of the mean path length predicted for an increasing number of scatterers is well reproduced thus confirming the validity of the mean path length invariance across the onset of the localization transition.

The corresponding experimental results shown in Fig. 5.3(b) (blue circles) are also in good agreement with the Weyl law. To appreciate how non-trivial this result is, Fig. 5.3(b) also shows the strong enhancement (reduction) of the transmission (reflection) time-delays across the localization transition (black squares and trian-

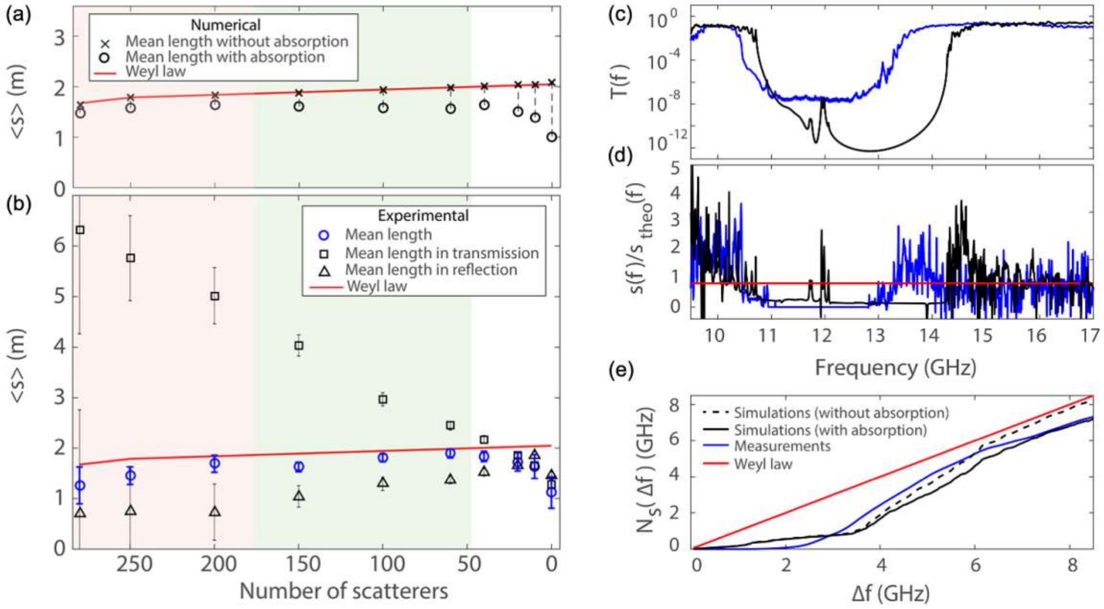

Figure 5.3: (a) Mean path length $\langle s[2q_\omega^{(t)}(\omega)]\rangle$ obtained in numerical simulations without (black crosses) and with (black circles) absorption as a function of the number of metallic cylinders within the cavity. The red solid line corresponds to the theoretical prediction of Weyl's law [see Eq. (5.6)] and the background colors rose, green and white indicate the localized, diffusive and the ballistic regime, respectively. (b) The same quantity, $\langle s[2q_\omega^{(t)}(\omega)]\rangle$, found experimentally (blue circles). The black squares and triangles show the mean path length in transmission and in reflection, respectively. The error bars represent the corresponding standard deviations. (c) Transmission spectra of a photonic crystal consisting of a periodic arrangement of aluminum and Teflon cylinders obtained in measurements (blue line) and in numerical simulations including absorption (black line). A transmission band gap is clearly observed for this sample with 15 longitudinal layers of regularly spaced scatterers. (d) Corresponding normalized path length spectra, where the finite photonic crystal gives rise to a drastically reduced, but not vanishing path length within the band gap in the numerical simulations. In both the measurements and the simulations, an enhancement of the path lengths can be observed at the edges of the corresponding band gap. (e) Integral of the path length normalized by its theoretical value over a frequency window of width Δf around the center of the corresponding band gap. Both the results obtained in measurements and in numerical simulations converge towards a value slightly below the theoretical prediction due to the presence of absorption. Numerical simulations in the absence of absorption (dashed black line) confirm the mean path length invariance by converging towards the Weyl law.

gles). We also observe a slight underestimation of the mean path length, especially in the ballistic regime, which can be attributed to the presence of absorption. This deviation comes as no surprise since the above derivations all rely on the assumption of a unitary scattering matrix. Thus, even though the DOS integrated over frequency is independent of absorption [152], the latter breaks unitarity and thus the correspondence between $s[q_\omega^{(S)}(\omega)]$ and $s[2q_\omega^{(t)}(\omega)]$, i.e., Eq. (5.7), as well as the close similarity of the time-delay and the dwell time operator [49].

To numerically model the uniform absorption in the experiment, we add an imaginary part to the effective refractive index of the cavity. The latter is determined by the comparison of the measured frequency-averaged transmission in the empty cavity with the numerical simulations, resulting in an average uniform imaginary part of the refractive index of $n_i = 2 \times 10^{-4}$ which is then also used for all the disorder configurations. Since the absorption introduced by this imaginary refractive index is small, the scattering matrix is still sufficiently unitary and thus $\langle s[2q_\omega^{(t)}(\omega)]\rangle$ still provides a reliable estimator for the theoretical value in absence of absorption. Interestingly, stronger deviations from the Weyl law can be found in the empty cavity which can be traced back to the above-mentioned wave states that correspond to bouncing orbits between the top and bottom cavity boundary (in y-direction). Due to their long cavity dwell times, these states are very strongly affected by dissipation which causes significant deviations from the mean path length invariance. The better agreement with the theoretical prediction for an increasing scattering strength can then be explained by the disorder scattering which naturally leads to a suppression of such states.

5.2 Photonic crystal

Having verified the mean path length invariance numerically as well as experimentally in all transport regimes of disorder scattering, we now investigate the opposite limit of a structured medium with periodic order. More specifically, we consider a periodic arrangement of alternating aluminum and Teflon cylinders forming a photonic crystal (PC) with 15 layers in the longitudinal direction (see supplementary material of Ref. [58]). As shown in Fig 5.3(c), this structure features a band gap (solid blue line) centered at $f_0 = 12$ GHz with a width of $\Delta f_0 \approx 2$ GHz. The periodic arrangement of scatterers fills the whole width of the waveguide and is longitudinally centered only filling out the middle part of the cavity. Thus, the free space in front of and after the PC also contributes to $s[2q_\omega^{(t)}(\omega)]$, and we subtract the theoretical free space contribution from the obtained mean path length outside the band gap in order to isolate the impact of the PC. In the band gap, the transmission remains in the noise floor of the experimental setup ($\approx 10^{-6}$) and we set $s[2q_\omega^{(t)}(\omega)] = 0$.

Numerical simulations are then performed for the same arrangement of aluminum and Teflon scatterers. However, instead of manually removing the free space contribution, we use a cavity whose length is adjusted to the longitudinal dimension of the PC. To include possible uncertainties in the experimental scatterer placement,

Die approbierte gedruckte Originalversion dieser Dissertation ist an der TU Wien Bibliothek verfügbar.
The approved original version of this doctoral thesis is available in print at TU Wien Bibliothek.
TU Bibliothek WIEN Your knowledge hub

we introduce a slight disorder by adding a random value drawn from the interval $[-r_{\text{scat}}/10, r_{\text{scat}}/10]$ to the transverse and longitudinal positions of the scatterers. Furthermore, we add absorption in order to closely mimic the situation in the experiment. The band gap obtained from the numerical simulations [solid black line in Fig. 5.3(c)] is centered at $f_0 = 12.6$ GHz with a width of $\Delta f_0 \approx 3.3$ GHz which is larger than in measurements. These differences might be attributed to tiny air gaps between the aluminum cylinders and the top plate of the waveguide (which cannot be captured by a 2D simulation), as scattering off the cylinder's top edge gives rise to the excitation of evanescent modes. The latter can then couple to neighboring Teflon scatterers whose higher refractive index compared to air might enable an evanescent mode to become propagating thus locally modifying the effective properties of the scatterers.

Figure 5.3(d) shows the corresponding path length spectra $s[2q_\omega^{(t)}(\omega)]$ normalized by the theoretical value $s_{\text{theo}}(\omega)$ in which the area of the Teflon scatterers has to be multiplied by their refractive index squared to account for the increased DOS in dielectric materials [153]. The path lengths obtained in the numerical simulations are now strongly reduced within the band gap, but do not completely vanish (similar to the transmission) as a consequence of the finite length of the PC. Also note that the dwell time can be negative as a result of absorption [49] and since the dwell time operator is related to the time-delay operator and thus also to $s[2q_\omega^{(t)}(\omega)]$, this explains the negative values in Fig. 5.3(d).

The appearance of a band gap seems to suggest that the path length invariance does not hold in such periodic structures. However, prior works on frequency sum rules [152, 154] show that reductions and enhancements of the DOS should compensate each other in arbitrary systems including band gap materials if the spectral window is sufficiently broad. Since the DOS is closely related to the path length $s[2q_\omega^{(t)}(\omega)]$, its strong decrease within the band gap should therefore be compensated by a corresponding enhancement right outside the band gap. Figure 5.3(d) shows that we indeed observe such enhancements close to the band edges, with $s[2q_\omega^{(t)}(\omega)]$ even exceeding $3s_{\text{theo}}(\omega)$ in measurements and simulations.

To verify the mean path length invariance, we normalize the path length by the theoretical Weyl prediction and integrate it over a frequency window Δf around the center of the corresponding band gap f_0 obtained in the experiment or in the simulation, i.e.,

$$N_s(\Delta f) = \int_{f_0-\Delta f/2}^{f_0+\Delta f/2} \frac{s[2q_\omega^{(t)}(\omega)]}{s_{\text{theo}}(\omega)} \,. \tag{5.23}$$

Note that the band gap centers are not located in the center of our frequency interval and thus we continue integration with only the higher frequency range once the lower end of 9.5 GHz is reached. The Weyl prediction for this quantity is $N_s(\Delta f) = \Delta f$ which increases linearly with the considered frequency range. Figure 5.3(e) shows the integrated ratio $N_s(\Delta f)$ of the experimental data (solid blue line) which vanishes for a spectral window smaller than the band gap, but then increases rapidly and progressively converges towards $N_s(\Delta f) \approx 0.86\Delta f$ at $\Delta f =$ 8.5 GHz. Similar to the empty cavity or the considered disorder configurations, the 14% deviation from the Weyl law can again be attributed to dissipation within the system. This is confirmed by numerical simulations (solid black line) in which the presence of absorption (modeled by $n_i = 2 \times 10^{-4}$) causes $N_s(\Delta f)$ to converge to the same value as in the measurements. The latter is even more remarkable when considering that the band gap widths obtained in the simulation and the experiment are not identical. In numerical simulations without absorption (dashed black line), $N_s(\Delta f)$ reaches $N_s(\Delta f) \approx 0.975\Delta f$ thus confirming that the almost vanishing path length inside the band gap is entirely compensated by the pronounced enhancements of $s[2q_\omega^{(t)}(\omega)]$ at the edges of the band gap.

Note that the numerical calculation of $q_\omega^{(t)}$ might involve singular transmission matrices for which an ordinary inverse does not exists. We therefore project each matrix onto the subspace containing only singular vectors corresponding to singular values greater than 10^{-10}. This enables us to compute the pseudo-inverse as presented in Appendix C. Experimentally, transmission eigenvalues smaller than $\tau_n < 10^{-6}$ are removed from the data since these eigenchannels may contain time-delays which are corrupted by the noise level of the experimental setup.

5.3 Influence of absorption

Equation (5.22) enables the estimation of the mean path length by using either the scattering, the transmission or both reflection matrices. However, absorption breaks this relation, and therefore we investigate its impact on all the involved operators in the following to identify the most reliable estimator of the mean path length in the presence of absorption. To arrive at analytical relations, we consider a toy model of a straight open waveguide (rather than the system depicted in Fig. 5.2) which consists of two scattering regions with scattering matrices

$$S_1 = \begin{pmatrix} r_1 & t_1' \\ t_1 & r_1' \end{pmatrix}, \quad S_2 = \begin{pmatrix} r_2 & t_2' \\ t_2 & r_2' \end{pmatrix} \tag{5.24}$$

separated by free space described by the scattering matrix S_2^{free}. We also add a free space section described by S_1^{free} (S_3^{free}) in front of the first (after the second) scattering region for generality. The corresponding scattering matrices for the free space sections are given by

$$S_j^{\text{free}} = \begin{pmatrix} 0 & P_j \\ P_j & 0 \end{pmatrix}, \tag{5.25}$$

where the propagation matrices, i.e., the transmission matrices through free space, are

$$P_j = \text{diag}\left(e^{ik_{x,n}L_j}\right). \tag{5.26}$$

Here, $j = 1, 2, 3$ is the number of the considered section with length L_j, where $k_{x,n} = \sqrt{k^2 - k_{y,n}^2}$ are the longitudinal propagation constants of the waveguide modes with $k_{y,n} = n\pi/W$ in an open waveguide of width W.

To investigate the impact of absorption on $\mathrm{Tr}(q_\omega^{(t)})$, we make use of the Feynman path integral formulation to calculate the transmission matrix as a sum over all possible paths, i.e.,

$$\begin{aligned} t &= P_3 t_2 P_2 t_1 P_1 \\ &\quad + P_3 t_2 P_2 r_1' P_2 r_2 P_2 t_1 P_1 \\ &\quad + P_3 t_2 P_2 r_1' P_2 r_2 P_2 r_1' P_2 r_2 P_2 t_1 P_1 + \ \ldots \\ &= P_3 t_2 \sum_{n=0}^{\infty} (P_2 r_1' P_2 r_2)^n P_2 t_1 P_1 \\ &= P_3 t_2 (\mathbb{1} - P_2 r_1' P_2 r_2)^{-1} P_2 t_1 P_1 \,. \end{aligned} \tag{5.27}$$

Here, we have employed the Neumann series, i.e., the analog of the geometric series for operators, assuming a convergent operator norm in which case $\sum_{n=0}^{\infty} O^n = (\mathbb{1} - O)^{-1}$ for an operator O. Hence, the inverse of the transmission matrix can be written as

$$t^{-1} = P_1^{-1} t_1^{-1} P_2^{-1} (\mathbb{1} - P_2 r_1' P_2 r_2) t_2^{-1} P_3^{-1} \,. \tag{5.28}$$

Using Eqs. (5.27) and (5.28), the trace of $q_\omega^{(t)} = -it^{-1} dt/d\omega$ then evaluates to

$$\mathrm{Tr}(q_\omega^{(t)}) = \mathrm{Tr}(q_\omega^{(t)})_{\text{direct}} + \mathrm{Tr}(q_\omega^{(t)})_{\text{multi}} \,, \tag{5.29}$$

with

$$\begin{aligned} \mathrm{Tr}(q_\omega^{(t)})_{\text{direct}} = \frac{1}{c} \mathrm{Tr}\Big[& - iP_3^{-1} \frac{dP_3}{dk} - it_2^{-1} \frac{dt_2}{dk} \\ & - iP_2^{-1} \frac{dP_2}{dk} - it_1^{-1} \frac{dt_1}{dk} - iP_1^{-1} \frac{dP_1}{dk} \Big] \end{aligned} \tag{5.30}$$

being the time-delay of the direct path. The second term in Eq. (5.29) reads

$$\mathrm{Tr}(q_\omega^{(t)})_{\text{multi}} = \frac{1}{c} \mathrm{Tr}\left[-i(\mathbb{1} - P_2 r_1' P_2 r_2) \frac{d(\mathbb{1} - P_2 r_1' P_2 r_2)^{-1}}{dk} \right] \tag{5.31}$$

and corresponds to contributions from the multiply scattered paths, where we have used the linearity of the trace and its invariance under cyclic permutations. We now introduce absorption by adding a uniform imaginary part n_i to the refractive index distribution which causes a change of the total wave vector $k \to k + i\kappa$ with $\kappa = n_i k$. In case of $n_i \ll 1$, the propagation constants can be written as

$$k_{x,n} \to \tilde{k}_{x,n} \left(1 + i n_i k^2 / \tilde{k}_{x,n}^2 \right) \tag{5.32}$$

with $\tilde{k}_{x,n} = \sqrt{(1-n_i^2)k^2 - k_{y,n}^2}$ and thus

$$P_j \to \mathrm{diag}\left(e^{i\tilde{k}_{x,n}L_j}e^{-n_i L_j k^2/\tilde{k}_{x,n}}\right). \tag{5.33}$$

The derivative of this quantity with respect to k is given by

$$\frac{dP_j}{dk} \to \mathrm{diag}\left(\frac{ikL_j}{\tilde{k}_{x,n}} - n_i L_j \left[\frac{2k}{\tilde{k}_{x,n}} - \frac{k^3}{\tilde{k}_{x,n}^3}\right]\right) P_j\,. \tag{5.34}$$

To further simplify Eq. (5.31), we Taylor-expand the inverse matrix expression

$$(\mathbb{1} - P_2 r_1' P_2 r_2)^{-1} = \mathbb{1} + P_2 r_1' P_2 r_2 + (P_2 r_1' P_2 r_2)^2 + \ \ldots \tag{5.35}$$

and use Eq. (5.34) to find

$$\frac{d(\mathbb{1} - P_2 r_1' P_2 r_2)^{-1}}{dk} \propto \mathcal{O}(P_2^2)\,. \tag{5.36}$$

Due to the exponential decay of P_j [see Eq. (5.33)], $\mathrm{Tr}(q_\omega^{(t)})_{\mathrm{multi}} = \mathcal{O}(P_2^2) \to 0$ in the limit of strong absorption and thus

$$\mathrm{Tr}(q_\omega^{(t)}) \to \mathrm{Tr}(q_\omega^{(t)})_{\mathrm{direct}}\,. \tag{5.37}$$

This reveals that the transmission delay times converge to those of the most direct path, i.e., the path from the input to the output leads that corresponds to the shortest time-delay, in the limit of strong absorption. This limit is already reached for $n_i \ll 1$ due to the fast exponential decay in Eq. (5.33). In case of a one-dimensional scattering system featuring barriers of finite height, it can be even shown that $cq_\omega^{(t)}$ reduces to the optical path length of the direct path through this system if absorption is strong. It is also worth pointing out that the contributions to the direct path in Eq. (5.30) are independent of absorption. In particular, the exponential decay drops out due to the appearance of P_j^{-1} and absorption only enters in form of a correction term in (5.34). However, since usually $n_i \ll 1$, these corrections are small and one can approximate $\tilde{k}_{x,n} \approx k_{x,n}$ and $dP_j/dk \approx \mathrm{diag}(ikL_j/k_{x,n})$, where the latter expression yields the free space propagation delay time in the absence of absorption in Eq. (5.30).

The convergence towards the most direct path in transmission is also reflected in the Poynting vector. As an example, the Poynting vector of the highest transmitting transmission eigenchannel in the empty cavity is shown in Figs. 5.4(a) and (b) in the absence and presence of strong absorption, respectively. There, the color of the vectors corresponds to the longitudinal component of the Poynting vector normalized by its magnitude. Without absorption, the metallic spacings between the leads of the cavity lead to scattering which in turn yields flux components pointing

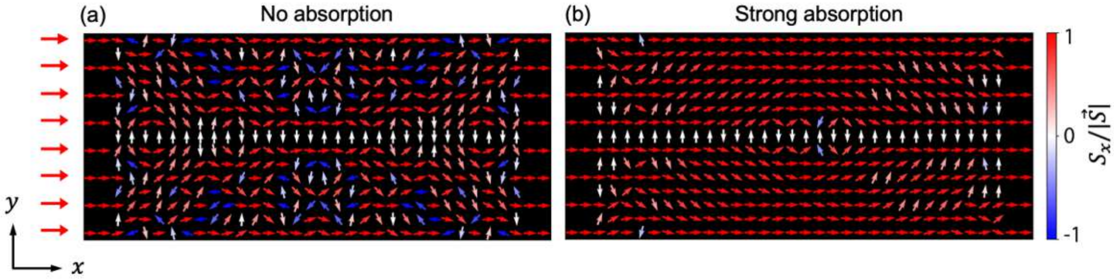

Figure 5.4: Spatial distribution of the time-averaged Poynting vector [Eq. (E.5), colored arrows] of the highest transmitting transmission eigenstate injected from the left leads (indicated by the red arrows on the outside) into the empty cavity. Here, the color corresponds to the longitudinal component of the Poynting vector normalized by its magnitude with red (blue) indicating the flux in the positive (negative) x-direction. (a) In the absence of absorption, scattering at the interfaces between the leads gives rise to flux-contributions pointing in the negative x-direction (blue color). (b) Same as (a), but for strong absorption modeled by a uniform imaginary part of the refractive index of $n_i = 10^{-2}$. One can clearly see that strong dissipation eliminates multiply scattered paths causing the flux to align with the positive x-direction (red color) which is a result of the convergence towards the most direct path in transmission from the input to the output leads as described by Eq. (5.37).

in the backward direction, i.e, the negative x-direction [blue color in (a)]. Introducing strong absorption then suppresses all the multiply scattered paths resulting in a Poynting vector distribution that is almost perfectly aligned with the forward direction, i.e., the positive x-direction [red color in (b)]. This behavior is very general and thus it can also be observed in the diffusive and localized regime (not shown) where the most direct paths get elongated due to the presence of scatterers.

Following the same strategy as above, we investigate the effect of absorption on $\mathrm{Tr}(q_\omega^{(r)})$. We start with the Feynman path integral representation of the reflection matrix

$$\begin{aligned} r = &P_1 r_1 P_1 \\ &+ P_1 t_1' P_2 r_2 P_2 t_1 P_1 \\ &+ P_1 t_1' P_2 r_2 P_2 r_1' P_2 r_2 P_2 t_1 P_1 + \ \ldots \\ = &P_1 r_1 P_1 + P_1 t_1' P_2 r_2 \sum_{n=0}^{\infty} (P_2 r_1' P_2 r_2)^n P_2 t_1 P_1 \\ = &P_1 r_1 P_1 + P_1 t_1' P_2 r_2 (\mathbb{1} - P_2 r_1' P_2 r_2)^{-1} P_2 t_1 P_1 \,, \end{aligned} \tag{5.38}$$

which we can rewrite as

$$r = P_1 r_1 P_1 \left[\mathbb{1} + P_1^{-1} r_1^{-1} t_1' P_2 r_2 (\mathbb{1} - P_2 r_1' P_2 r_2)^{-1} P_2 t_1 P_1 \right] . \tag{5.39}$$

Assuming strong absorption, the second term in the square brackets is small which allows us to approximate its inverse by $(1+x)^{-1} \approx 1 - x$. Thus we get

$$r^{-1} \approx \left[\mathbb{1} - P_1^{-1} r_1^{-1} t_1' P_2 r_2 (\mathbb{1} - P_2 r_1' P_2 r_2)^{-1} P_2 t_1 P_1\right] P_1^{-1} r_1^{-1} P_1^{-1} \,. \tag{5.40}$$

Using the above expressions, we now calculate $dr/d\omega$ and $q_\omega^{(r)}$ and find

$$\mathrm{Tr}(q_\omega^{(r)}) = \mathrm{Tr}(q_\omega^{(r)})_{\text{direct}} + \mathrm{Tr}(q_\omega^{(r)})_{\text{multi}} \tag{5.41}$$

with the contributions from the direct path being

$$\mathrm{Tr}(q_\omega^{(r)})_{\text{direct}} = \frac{1}{c} \mathrm{Tr}\left[-iP_1^{-1} \frac{dP_1}{dk} - ir_1^{-1} \frac{dr_1}{dk} - iP_1^{-1} \frac{dP_1}{dk}\right] . \tag{5.42}$$

The contributions from the multiply scattered paths are again

$$\mathrm{Tr}(q_\omega^{(r)})_{\text{multi}} = \mathcal{O}(P_2^2) \,. \tag{5.43}$$

In the limit of strong absorption, we thus again find that $\mathrm{Tr}(q_\omega^{(r)})_{\text{multi}} \to 0$ which yields

$$\mathrm{Tr}(q_\omega^{(r)}) \to \mathrm{Tr}(q_\omega^{(r)})_{\text{direct}} \,. \tag{5.44}$$

Similar to the delay times in transmission, also the delay times in reflection for strong absorption and $n_i \ll 1$ reduce to the delay times of the most direct path (in the absence of absorption) which corresponds to reflections at the first scattering layer.

To complete the picture, we now also investigate the effect of absorption on $\mathrm{Tr}(q_\omega^{(S)})$ which contains the full scattering matrix of the system

$$S = \begin{pmatrix} r & t' \\ t & r' \end{pmatrix} . \tag{5.45}$$

Due to the additional information stored in S, one might be tempted to think that $q_\omega^{(S)}$ will lead to a better estimate of the Weyl prediction, however, this is not the case as we will show in the following. To calculate $q_\omega^{(S)}$, we invert the scattering matrix blockwise

$$S^{-1} = \begin{pmatrix} r^{-1} + r^{-1} t' M t r^{-1} & -r^{-1} t' M \\ -M t r^{-1} & M \end{pmatrix} \tag{5.46}$$

with $M = (r' - t r^{-1} t')^{-1}$ which is valid if r and M are non-singular. The trace of $q_\omega^{(S)}$ then evaluates to

$$\begin{aligned} \mathrm{Tr}(q_\omega^{(S)}) = \frac{1}{c} \mathrm{Tr}\Bigg[& - ir^{-1} \frac{dr}{dk} - ir^{-1} t' M t r^{-1} \frac{dr}{dk} \\ & + ir^{-1} t' M \frac{dt}{dk} + iM t r^{-1} \frac{dt'}{dk} - iM \frac{dr'}{dk} \Bigg] . \end{aligned} \tag{5.47}$$

Die approbierte gedruckte Originalversion dieser Dissertation ist an der TU Wien Bibliothek verfügbar.
The approved original version of this doctoral thesis is available in print at TU Wien Bibliothek.
TU Bibliothek WIEN Your knowledge hub

Since absorption causes an exponential decrease in transmission, strong absorption will lead to $t \to 0$ and $t' \to 0$. In this limit, $M \to r'^{-1}$ and

$$\mathrm{Tr}(q_\omega^{(S)}) \to \mathrm{Tr}(q_\omega^{(r)}) + \mathrm{Tr}(q_\omega^{(r')})\,. \tag{5.48}$$

Thus, the consideration of the full scattering matrix in the time-delay operator leads to a substantial underestimation of the mean path length since the direct paths in reflection are much shorter than the direct paths in transmission which have to traverse the scattering system.

To validate the above findings, we perform numerical simulations of the experimental setup in the frequency range of 11-13 GHz. Absorption is then introduced via a uniform imaginary part of the refractive index which is progressively increased up to $n_i = 10^{-2}$. The resulting mean path lengths obtained with the operators $q_\omega^{(S)}$, $2q_\omega^{(t)}$ and $q_\omega^{(r)} + q_\omega^{(r')}$ are shown in Figs. 5.5(a)-(c) for the different transport regimes. Each data point in the diffusive and localized regime corresponds to an average over 200 random configurations and 100 frequency values in the considered interval. For the empty system, we use 20000 frequency values between 11 and 13 GHz to compensate the missing configuration average. For all the different operators, the corresponding mean path lengths decrease with increasing absorption.

The rapid decrease of $\langle s(2q_\omega^{(t)})\rangle/\langle s_{\mathrm{theo}}\rangle$ in the empty system can be understood by the convergence towards the most direct path in transmission as described by Eq. (5.37). To estimate its length, we use the time-delay of a straight and empty waveguide section of length ℓ which is $\ell k/k_{x,n}$. Therefore, the propagation time corresponding to the shortest possible path is given by the time-delay of the lowest transverse waveguide mode in the corresponding sections. Thus, we can estimate the direct path via

$$\langle L_{\mathrm{direct}}^{\mathrm{empty}}(k)\rangle \approx \left\langle \frac{2lk}{k_{x,1}^{\mathrm{lead}}} + \frac{Lk}{k_{x,1}^{\mathrm{scat}}} \right\rangle = 0.63\ \mathrm{m}\,, \tag{5.49}$$

where $k_{x,1}^{\mathrm{lead}} = \sqrt{k^2 - (\pi/w)^2}$ and $k_{x,1}^{\mathrm{scat}} = \sqrt{k^2 - (\pi/W)^2}$ are the propagation constants of the lowest transverse mode in the leads and the scattering region, respectively. Performing the frequency average in the interval 11-13 GHz and using the corresponding theoretical value $\langle s_{\mathrm{theo}}\rangle = 2.05$ m then yields

$$\frac{\langle L_{\mathrm{direct}}^{\mathrm{empty}}\rangle}{\langle s_{\mathrm{theo}}\rangle} \approx 0.31\,. \tag{5.50}$$

This estimation is in very good agreement with the ratio $\langle s(2q_\omega^{(t)})\rangle/\langle s_{\mathrm{theo}}\rangle$ obtained in the numerical simulations which converges to 0.32 for the strongest considered absorption [see blue curve in Fig. 5.5(a)]. The latter value is slightly larger than the estimate since the different modes do not propagate in straight lines, but are associated with certain propagation angles causing the waves to exit the system

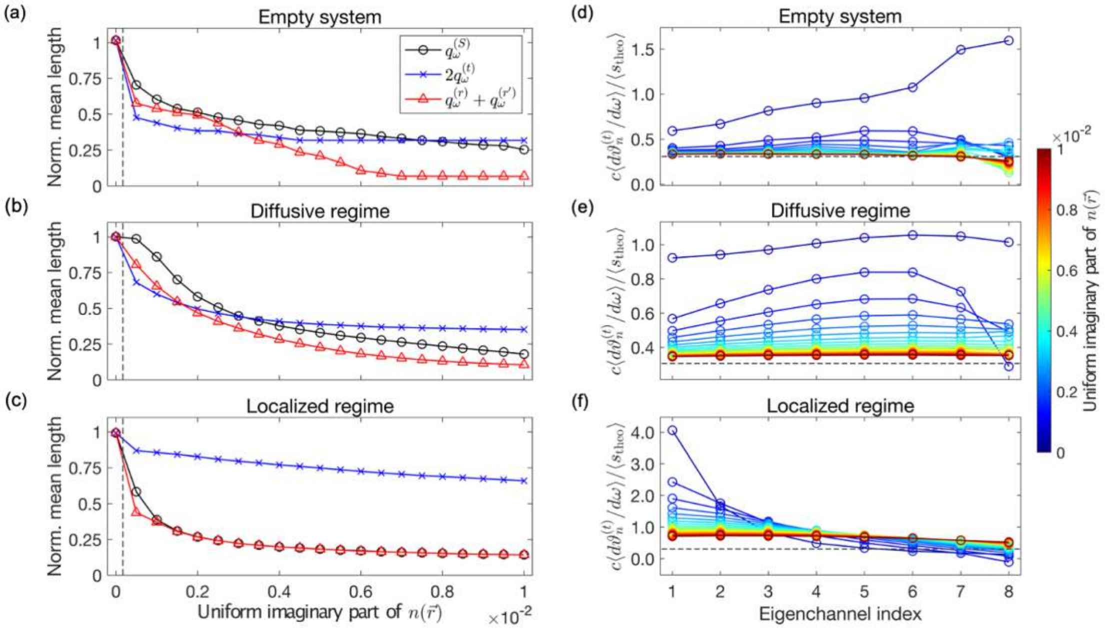

Figure 5.5: (a)-(c) Normalized mean path lengths in the empty system, the diffusive and the localized regime obtained in numerical simulations via $\langle s(O)\rangle/\langle s_{\text{theo}}\rangle$, where O represents the corresponding operators in the legend and s_{theo} is the theoretical path length in the absence of absorption [Eq. (5.6)]. In the considered frequency range of 11-13 GHz, the latter evaluates to $\langle s_{\text{theo}}\rangle = 2.05$ m in the empty system, $\langle s_{\text{theo}}\rangle = 2.03$ m for $n_{\text{scat}} = 20$ in the diffusive regime and $\langle s_{\text{theo}}\rangle = 1.76$ m for $n_{\text{scat}} = 280$ in the localized regime. The vertical dashed lines indicate the absorption strength for which the frequency-averaged conductance in the empty cavity is equal to the experimentally measured one. The mean path length obtained with each of the considered operators monotonically decreases with increasing absorption strength, where the convergence of $\langle s(q_\omega^{(S)})\rangle$ to $\langle s(q_\omega^{(r)}+q_\omega^{(r')})\rangle$ [Eq. (5.48)] can clearly be seen, especially for stronger scattering strengths. (d)-(f) Normalized transmission eigenchannel contribution to the mean path length in all the considered transport regimes as a function of the eigenchannel index, where the index 1 (8) corresponds to the highest (lowest) transmitting eigenchannel. Increasing absorption leads to a redistribution of the transmission time-delays which all converge to the length of the most direct path in the limit of strong absorption [see Eq. (5.37)]. The horizontal grey dashed line marks an estimation of the most direct path in the empty system which agrees very well with the numerically obtained transmission delay times for the strongest absorption.

through output ports not exactly opposite to their input port. Moreover, since $\langle s(q_\omega^{(S)})\rangle$ is not fully converged to $\langle s(q_\omega^{(r)}+q_\omega^{(r')})\rangle$ [Eq. (5.48)] (black and red curve), this also indicates that the absorption is too weak to suppress all but the direct path.

The convergence towards the most direct transmission path in the limit of strong absorption still holds in the diffusive and localized regime, where the presence of impenetrable metallic scatterers leads to an elongation of the most direct paths. This can be seen in Figs. 5.5(b) and (c), where an increasing number of scatterers causes the normalized mean length in transmission (blue curve) to converge to a much larger value than for the empty waveguide [Eq. (5.50)]. This effect is especially pronounced in the localized regime shown in Fig. 5.5(c). Here, the presence of 280 metallic scatterers increases the mean path length compared to the empty system leading to a better estimate of the value predicted by the Weyl law. Specifically, we numerically obtain $\langle s(2q_\omega^{(t)})\rangle = 0.66\langle s_{\text{theo}}\rangle$ for $n_i = 10^{-2}$.

Considering the mean path length in reflection, $\langle s(q_\omega^{(r)} + q_\omega^{(r')})\rangle/\langle s_{\text{theo}}\rangle$ converges to small values in all transport regimes which resemble the direct paths in reflection [see Eq. (5.44)], i.e., reflections at the first scattering layer. In case of the time-delay operator $q_\omega^{(S)}$, Figs. 5.5(a)-(c) clearly show the convergence of $\langle s(q_\omega^{(S)})\rangle$ to $\langle s(q_\omega^{(r)} + q_\omega^{(r')})\rangle$ [see Eq. (5.48)] which leads to a pronounced underestimation of the Weyl prediction. Strong absorption thus prevents the accurate prediction of the invariant mean path length in all transport regimes with the transmission matrix providing a more reliable estimator of the Weyl prediction than its estimation based on the reflection matrices or the full scattering matrix. This is particularly pronounced in strongly scattering systems, i.e., in the localized regime, in which the direct paths in transmission still have to traverse the entire system in contrast to the direct paths in reflection that correspond to reflections at the first scattering layer.

The convergence towards the most direct path in the limit of strong absorption is not a peculiar feature of a single transmission or reflection eigenstate, but holds for all eigenchannels of $t^{(\prime)\dagger}t^{(\prime)}$ and $r^{(\prime)\dagger}r^{(\prime)}$. To illustrate that, Figs. 5.5(d)-(f) show the averaged transmission eigenchannel path lengths normalized by the theoretical value given by the Weyl law, where an eigenchannel index of 1 (8) corresponds to the highest (lowest) transmitting eigenchannel. Strong absorption causes all transmission eigenchannel delay times [see Eq. (5.13)] to converge towards a single value. For the empty system in Fig. 5.5(d), this value coincides very well with the estimate of the direct path in Eq. (5.50) which is indicated by the gray dashed line. In the diffusive and localized transport regime, the elongation of the direct paths due to the presence of scatterers causes a convergence to a value larger than $\langle L_{\text{direct}}^{\text{empty}}\rangle$. The suppression of multiply scattered paths is therefore a generic feature of strong absorption which effects all transmission and reflection eigenchannels thus generalizing the observations in Ref. [155].

5.4 Conclusion

We demonstrate numerically and experimentally, that the surprising property of an invariant mean path length holds for waves in the ballistic, diffusive and localized regime of disorder scattering. In addition, we show that this invariance also applies to systems with periodic order like photonic crystals that feature a transmission band gap in a certain range of frequencies. Here, the suppression of the path length within the band gap gets compensated by an enhancement right outside the band gap. Therefore, our results provide a comprehensive bound on the enhancement of the mean path length of broadband light in a medium and are thus deeply linked to the so-called Yablonovitch limit [156] enabling applications in, e.g., the design of structures that enhance light harvesting for solar cells [157] or the enhancement of the light-matter interaction via the amount of stored light intensity. We further consider the limit of strong uniform absorption, where we encounter the convergence towards the most direct paths which applies to all eigenchannels in transmission as well as in reflection. Based on the close relation between absorption and dwell time [10, 158], we also envision an extension of the presented results to an invariance property of the mean absorption in scattering media which could be used to investigate the limits of the Yablonovitch limit in a wave-mechanical description.

In the last chapter, we stay in the realm of non-Hermitian physics and show how to obtain wave states that get optimally, i.e, perfectly, absorbed at a localized loss element that is embedded in a complex scattering environment.

Chapter 6

Random anti-lasing through coherent perfect absorption[18]

Loss and absorption are detrimental to many applications, however, in some cases the absorption of radiation is essential as, e.g., in the reception or spectral filtering of electromagnetic signals or light harvesting processes. For such applications, the goal is to reach the ultimate limit of perfect absorption which can be achieved by exploiting the effect of *coherent perfect absorption (CPA)* [59, 159–161]. CPA is commonly referred to as “anti-lasing” as it corresponds to the time-reversed process of lasing at threshold (where all radiation losses are exactly balanced by the optical gain). A schematic depiction of the CPA-laser correspondence is shown in Fig. 6.1. Note, however, that above the lasing threshold non-linear effects lead to a breakdown of this correspondence.

The effect of CPA has first been theoretically investigated in Ref. [59]. There, a simple one-dimensional system consisting of a finite region with constant refractive index and uniform absorption is irradiated from both sides. Provided that a precise amount of dissipation is added and the amplitudes and phases of the incident waves are suitably adjusted, such structures can be made perfectly absorbing due to the interplay of interference and absorption. Specifically, the reflected part of the beam incident from the left destructively interferes with the transmitted part of the beam incident from the right and vice versa. Therefore, the wave is trapped inside the absorbing slab for an infinite time [162, 163] and thus it is entirely lost to dissipation. Perfect absorption can therefore even occur in systems which feature very small rates of single-pass absorption as, e.g., a silicon slab which was used in the first experimental demonstration of this intriguing effect [160].

---

[18] The results presented in this chapter were obtained in collaboration with my former colleagues Philipp Ambichl and Andre Brandstötter, my current colleague Kevin Pichler, our experimental collaborators Ulrich Kuhl and his former PhD student Julian Böhm from the Université Côte d’Azur. The theoretical and numerical tasks were carried out by myself, Kevin Pichler, Andre Brandstötter and Philipp Ambichl under supervision of Stefan Rotter. The experimental setup was designed by Ulrich Kuhl and Julian Böhm and the measurements and data evaluation were carried out by Kevin Pichler. The presented results are based on our joint publication [60] from which parts of the text and figures have been taken.

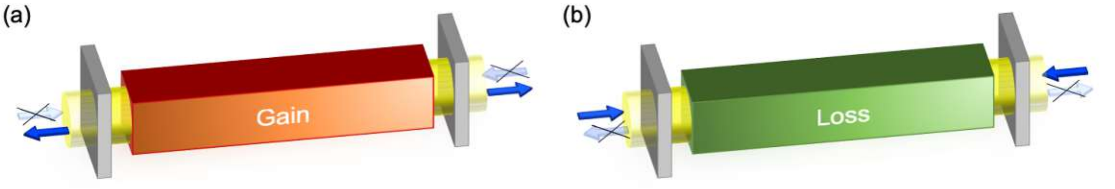

Figure 6.1: (a) Schematic of a laser in which a pumped gain medium embedded in a cavity emits outgoing coherent radiation (in the absence of waves incident from the exterior). (b) Schematic of CPA, i.e., the time-reversed process of lasing at threshold. Time-reversing the outgoing wave field of the lasing mode in (a) and replacing the gain medium by an absorbing medium with the corresponding amount of loss leads to perfect absorption of the incoming radiation and eliminates all back-reflections to the exterior.

Since then, CPA has been realized experimentally in a wide variety of different setups [161, 164–170] with the notable exception of a CPA in a disordered medium, i.e., a medium without an engineered structure. In such a case, a CPA would correspond to the time-reverse of a random laser [171, 172] in which the multiple scattering caused by a disordered active medium confines the light leading to a resonant enhancement of modes with specific frequencies. Due to the highly complex nature of the scattering process, the output profiles of such lasing modes are also spatially complex and not focused like a regular laser beam. Therefore, it is very challenging to time-reverse such light fields, especially since the time-reversal has to be applied to all of the field's degrees of freedom (in both its amplitudes and phases). In addition, also the absorption strength (time-reversal turns gain regions into loss regions) and the frequency of the radiation have to be precisely adjusted. In this chapter, we demonstrate that even for a strongly disordered medium, where the impinging wavefront first has to penetrate some scattering layers to reach the absorber, surprisingly the absorption can still be perfect. As in the one-dimensional case, this is caused by the interplay of absorption and destructive interference which fully dissipates the wave at the absorber and eliminates all back-reflections to the exterior.

In the framework of scattering theory, CPA and lasing can be related to the zeros and poles of the scattering matrix, respectively. Utilizing the input-output relationship $\vec{v} = S\vec{u}$, the injection of an S-matrix eigenstate $\vec{u}_{\text{CPA}}$ corresponding to a zero-eigenvalue $\Lambda_{\text{CPA}} = 0$ leads to a vanishing outgoing field $S\vec{u}_{\text{CPA}} = 0$ and thus to CPA. On the other hand, lasing can be described by the poles rather than the zeros of the S-matrix which give rise to a divergent response for a finite input field. Zeros and poles generally occur at discrete points in the complex frequency plane where in the absence of gain and loss they are symmetrically distributed around the real axis, i.e., zeros are complex conjugates of poles. The addition of gain or loss makes the system non-Hermitian causing the zeros and poles to move in the complex frequency plane. To illustrate that, we use the Caley transform of the scattering matrix in the effective Hamiltonian formalism which can be obtained by rewriting the latter as follows [71]:

$$\begin{aligned} S &= -\mathbb{1} + 2iV^\dagger G V \\ &= -\mathbb{1} + 2iV^\dagger [G_0^{-1} + iVV^\dagger]^{-1} V \\ &= -\mathbb{1} + 2iV^\dagger [(\mathbb{1} + iVV^\dagger G_0) G_0^{-1}]^{-1} V \\ &= -\mathbb{1} + 2iV^\dagger G_0 (\mathbb{1} + iVV^\dagger G_0)^{-1}] V \\ &= -\mathbb{1} + 2iV^\dagger G_0 \sum_n (-iVV^\dagger G_0)^n V\,. \end{aligned} \tag{6.1}$$

Here, we have used $G = (G_0^{-1} + iVV^\dagger)^{-1}$ and $G_0 = (\Delta + n^2 k^2)^{-1}$. Next, reordering the terms in the sum according to $(VV^\dagger G_0)V = V(V^\dagger G_0 V)$ yields

$$\begin{aligned} S &= -\mathbb{1} + 2iV^\dagger G_0 V \sum_n (-iV^\dagger G_0 V)^n \\ &= -\mathbb{1} + 2iV^\dagger G_0 V (1 + iV^\dagger G_0 V)^{-1} \\ &= -\frac{\mathbb{1} - iV^\dagger G_0 V}{\mathbb{1} + iV^\dagger G_0 V}\,. \end{aligned} \tag{6.2}$$

To show the mirror symmetry of zeros and poles, we calculate the determinant of Eq. (6.2) resulting in

$$\mathrm{Det}(S) = \mathrm{Det}\left(-\frac{\mathbb{1} - iV^\dagger G_0 V}{\mathbb{1} + iV^\dagger G_0 V}\right) = (-1)^{2N} \frac{\mathrm{Det}(\mathbb{1} - iV^\dagger G_0 V)}{\mathrm{Det}(\mathbb{1} + iV^\dagger G_0 V)}\,. \tag{6.3}$$

Here, the exponent of $2N$ appears due to the $2N$ scattering channels in the considered two-port device. Using Sylvester's determinant identity $\mathrm{Det}(\mathbb{1} \pm V^\dagger A V) = \mathrm{Det}(\mathbb{1} \pm AVV^\dagger)$ with $A = G_0$ then gives

$$\begin{aligned} \mathrm{Det}(S) &= \frac{\mathrm{Det}(\mathbb{1} - iG_0 VV^\dagger)}{\mathrm{Det}(\mathbb{1} + iG_0 VV^\dagger)} \\ &= \frac{\mathrm{Det}(G_0^{-1} - iVV^\dagger)}{\mathrm{Det}(G_0^{-1} + iVV^\dagger)} = \frac{\mathrm{Det}(G)}{\mathrm{Det}(G^\dagger)} = \frac{\mathrm{Det}(\tilde{G})}{\mathrm{Det}(\tilde{G}^\dagger)}\,, \end{aligned} \tag{6.4}$$

where we have used $G_0 = G_0^\dagger$ and the modified Green's function of the Helmholtz equation $\tilde{G} = Gn^2$ (for more details we refer to Ref. [71]). Since the ratio of products is equal to the product of the ratios, we can express Eq. (6.4) as a product of the ratios of the complex eigenvalues $1/(k^2 - \lambda_n)$ of the Green's function $\tilde{G}$ and its complex conjugate, i.e.,

$$\mathrm{Det}(S) = \prod_n \frac{k^2 - \lambda_n^*}{k^2 - \lambda_n} = \prod_n \frac{\omega^2 - \omega_n^2 - i\gamma_n/2}{\omega^2 - \omega_n^2 + i\gamma_n/2} \tag{6.5}$$

with $\lambda_n = k_n^2 - i\Gamma_n/2 = (\omega_n^2 - i\gamma_n/2)/c^2$ being the eigenvalues of the Helmholtz equation. The latter are complex since the term $iVV^\dagger$ describing the coupling of the closed system to the leads makes the Helmholtz operator non-Hermitian giving rise to the imaginary part of the eigenvalues $\Gamma_n = \gamma_n/c^2$. Equation (6.5) is valid in the unitary regime in which zeros and poles occur at the frequencies $\omega_{z,n}^2 = \omega_n^2 + i\gamma_n/2$ and $\omega_{p,n}^2 = \omega_n^2 - i\gamma_n/2$, respectively. This shows, that a unitary scattering matrix has zeros in the upper half of the complex frequency plane, i.e., $\mathrm{Im}(\omega_{z,n}) > 0$, whereas poles are located in the lower half of the complex plane, i.e., $\mathrm{Im}(\omega_{p,n}) < 0$. Furthermore, Eq. (6.5) shows that zeros and poles are symmetrically distributed around the real axis in the absence of gain and loss. In general, zeros and poles correspond to “unphysical” solutions since their complex frequency values give rise to exponential growth and decay in time under $e^{-i\omega t}$ convention, respectively [161].

To obtain physical solutions, loss and gain can be added to the system in order to move them onto the real axis. To demonstrate that, we consider uniform absorption which can be described by $\omega^2 \to \omega^2 + i\gamma_a/2$ [173], where $\gamma_a > 0$ defines the absorption strength. In this case, the zeros and poles become $\omega_{z,n}^2 = \omega_n^2 + i(\gamma_n - \gamma_a)/2$ and $\omega_{p,n}^2 = \omega_n^2 - i(\gamma_n + \gamma_a)/2$, respectively. Thus, when $\gamma_a = \gamma_n$, i.e., when attenuation losses exactly balance the dissipation through the channels, the imaginary part of $\omega_{z,n}$ vanishes. The disordered medium then turns into a CPA at exactly those frequencies and loss values at which $\omega_{z,n}$ crosses the real ω-axis. Similarly, uniform gain can be described by $\gamma_a < 0$ leading to physical lasing solutions as soon as the first S-matrix pole hits the real axis which defines the lasing threshold. Above threshold, nonlinear saturation effects stabilize the S-matrix poles on the real axis, while no such effects are at work for the S-matrix zeros making it possible to drag them below the real axis. Thus, as already briefly mentioned, the analogy between lasing and anti-lasing only holds on the linear level at the mode-specific lasing thresholds.

6.1 Experimental realization in a microwave setup

In the following, we present the first experimental realization of such a random anti-laser, i.e., of CPA in a disordered medium. To achieve full level of control, we use a microwave waveguide setup similar to the one used in Chapter 3 which enables us to measure the scattering matrix in a large frequency range and to inject any desired field pattern. The setup is schematically depicted in Fig. 6.2 and consists of a waveguide in which 60 randomly placed cylindrical Teflon scatterers simulate a disorder that scatters the incident waves. At the operational frequency range of 6-7.5 GHz, the waveguide supports four TE_{m0} modes which can be fully controlled in both their amplitudes and phases via four antennas on each side (left and right) of the waveguide. In the middle of the scattering region, we insert a monopole antenna which provides a localized loss channel that should perfectly absorb the incoming

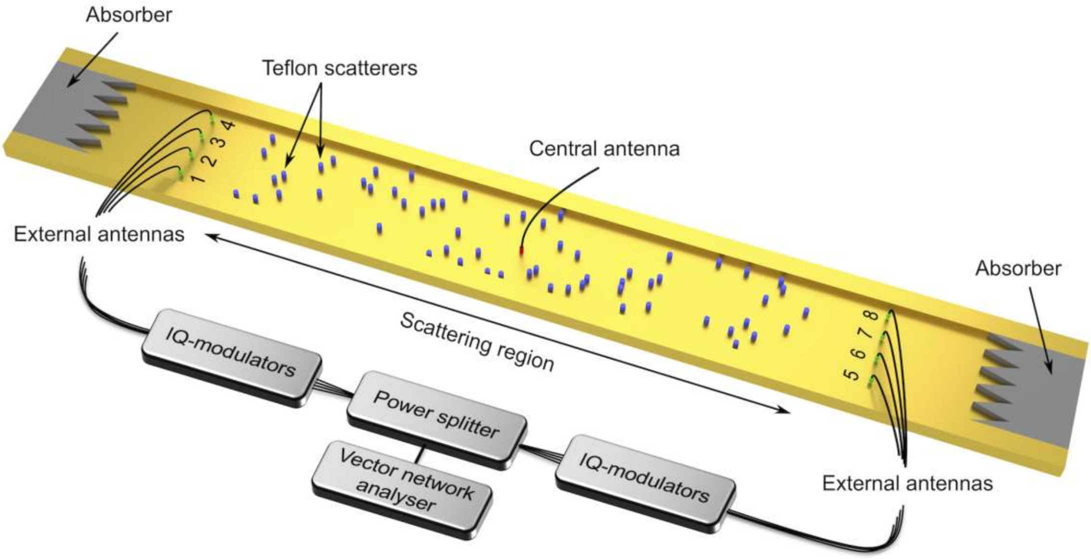

Figure 6.2: Sketch of the experimental setup in which microwaves with a well-defined frequency are generated by a vector network analyzer and equally distributed to eight in-phase/quadrature (IQ) modulators. The latter enable the control of the amplitudes and relative phases of the signals which are then injected into an aluminum waveguide of width $W = 10$ cm and height $h = 8$ mm via four antennas on each side. The central scattering region of length $L = 60$ cm contains 60 randomly placed Teflon scatterers with radius $r = 2.55$ mm that simulate a disorder. Localized absorption is introduced via the insertion of a monopole antenna (central antenna) through the top plate of the waveguide (not shown) in the middle of the disordered region. The absorption strength of this antenna can be tuned by varying its insertion length which determines its coupling to the waveguide. Absorbers are placed on both waveguide ends to avoid back-reflections of the injected and transmitted signals. To determine the scattering matrix, the field is measured between the external antennas and the scattering region on the left and right using a movable antenna (not shown) that dips into the waveguide through a grid of holes in the waveguide's top plate.

waves. As necessary for the realization of a CPA, the absorption strength of this antenna has to be precisely adjusted which can be done by varying its penetration depth into the waveguide thus changing its coupling strength to the system.

To experimentally find the point of CPA, the S-matrix of the system is measured in a frequency interval broad enough to contain many S-matrix zeros and for a number of penetration depths of the central antenna that cause absorption strong enough to drag the zeros with the smallest imaginary parts down to the real ω-axis. We then evaluate the eigenvalues of all these scattering matrices and identify the parameter combination at which the absolute value of the smallest S-matrix eigenvalue is closest to zero. Last, we set the frequency and the absorption strength to the point at which CPA occurs and inject the eigenstate corresponding to the minimum eigenvalue into the system in order to determine its degree of absorption.

Figure 6.3(a) depicts the results obtained by following this approach. There, the blue curve shows the ratio of outgoing to incoming intensity ($I_{\text{out}}/I_{\text{in}}$) of one CPA state as a function of the frequency, where we find a pronounced minimum at the corresponding CPA frequency, i.e., the frequency at which the injected CPA state was evaluated. This minimum corresponds to 99.78% absorption which is a first hallmark of CPA (the same minimum can also be observed in the minimal S-matrix eigenvalue which is not shown).

To ensure that this effect is truly caused by CPA rather than by a coherent enhancement of absorption (CEA) [61] or by one of the previously introduced focusing schemes [3, 8, 174, 175], we perform a number of independent tests. First, since global absorption in the aluminum waveguide is small, we expect the CPA state to be primarily absorbed by the central antenna. Since a CPA state is purely incoming (at its CPA frequency) due to the interferometric cancellation of the back-reflections to the exterior, the time-reversed situation of injecting a signal at the CPA frequency through the central antenna should yield a state that is purely outgoing. In this case, back-reflections into the central antenna should vanish as a result of its critical coupling [176, 177] to the disordered waveguide system. The red dashed curve in Fig. 6.3(a) shows the back-reflection signal $|R|^2$ into the central antenna, where we indeed observe a dip very close to the actual CPA frequency. This dip is slightly shifted in frequency by 0.025% with respect to the dip of $I_{\text{out}}/I_{\text{in}}$ which is a result of experimental imperfections and the imperfect time-reversal (weak uniform loss in the waveguide walls cannot be turned into uniform gain).

Since CPA requires critical coupling of the central antenna to the disordered waveguide, we also investigate its dependence on the coupling strength. Due to the absence of non-linear effects in case of absorption, an S-matrix zero can also be pulled below the real axis which in turn should lead to a reduced amount of absorption not only in the undercoupled (zero above the real axis), but also in the overcoupled regime (zero below the real axis). The right panels in Fig. 6.3(a) show the ratio $I_{\text{out}}/I_{\text{in}}$ and the back-reflection signal $|R|^2$ in a small frequency range around the CPA frequency with both being optimal, i.e., minimal, for an antenna that extends 7 mm into the waveguide (whose height is 8 mm). Moreover, we find that both under- and overcoupling corresponding to shorter and longer insertion lengths, respectively, indeed diminish the resonant CPA minimum substantially.

To further illustrate the sensitivity of CPA, we also investigate the effect of a slight amplitude or phase detuning of only one of the eight external antennas. Figure 6.3(b) shows the corresponding results, in which the amplitude (left panel) or the phase (right panel) of the antenna 2, 4 or 6 (the numbers correspond to the ones in Fig. 6.2) is sightly detuned from the actual CPA state. There, we observe that the CPA dip, i.e., the minimum of $I_{\text{out}}/I_{\text{in}}$ at approximately 7.1 GHz, gets considerably shifted upwards by factors of up to approximately 10^3. This illustrates how strongly

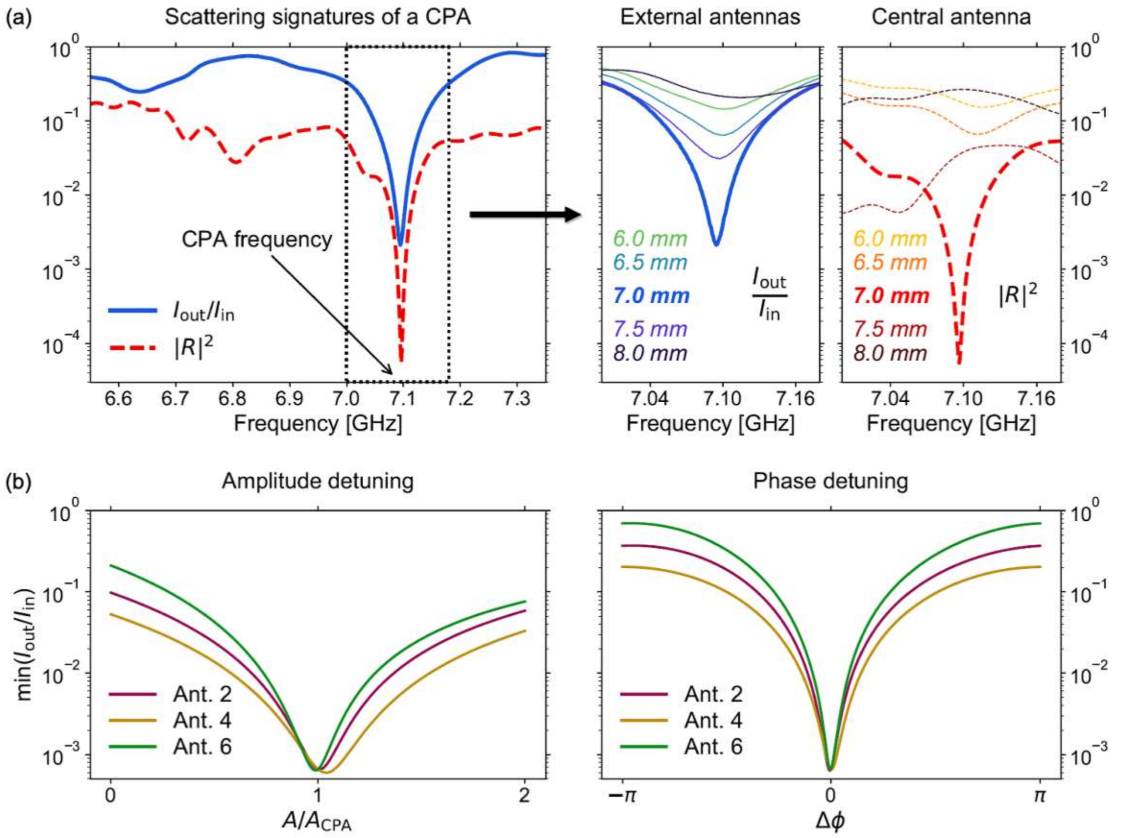

Figure 6.3: (a) Ratio of the outgoing to the incoming intensity $I_{\text{out}}/I_{\text{in}}$ (blue curve) of a CPA state in the disorder configuration shown in Fig. 6.2 as a function of the frequency. The red dashed curve is the back-reflection signal $|R|^2$ into the central antenna when microwaves are injected there. Both curves show a pronounced minimum close to the CPA frequency of 7.1 GHz. As shown in the two panels on the right, this minimum sensitively depends on the insertion length of the central antenna into the waveguide. Increasing the antenna length first deepens both dips until they reach a minimum at 7 mm. Further increasing the loss by increasing the antenna's length then results in an increase of both $I_{\text{out}}/I_{\text{in}}$ and $|R|^2$ and thus to a reduced absorption efficiency. (b) Sensitivity of the CPA minimum to a detuning of the amplitude A (left panel) or the phase ϕ (right panel) of only one of the input antennas (the antenna numbers correspond to the ones in Fig. 6.2) from the actual CPA state that is characterized by A_{CPA} and ϕ_{CPA}. Each of these detunings leads to a significant deterioration of the absorption efficiency which illustrates the sensitivity of the CPA effect.

the absorption is controlled interferometrically and highlights the importance of precisely adjusting the amplitudes and phases of all degrees of freedom of the input field in order to reach perfect absorption.

At the point of CPA, waves are exclusively propagating inwards which should be reflected in the Poynting vector of the corresponding CPA state. Since the Poynting

Die approbierte gedruckte Originalversion dieser Dissertation ist an der TU Wien Bibliothek verfügbar.
The approved original version of this doctoral thesis is available in print at TU Wien Bibliothek.
TU Bibliothek WIEN Your knowledge hub

vector is experimentally not accessible, we perform numerical simulations using the framework introduced in Section 2.1 and the scattering configuration shown in Fig. 6.2. To model the central absorbing antenna in our two-dimensional numerical simulations, we use a circular dielectric scatterer with a diameter of $d = 4$ mm and a complex refractive index whose real and imaginary part can be adjusted in order to control the absorption and the coupling to the waveguide. To find the point of CPA, we set the frequency to the experimentally obtained CPA frequency and perform a gradient descent optimization to determine the real and imaginary part of the absorbing antenna scatterer's refractive index n_{ant} at which the absolute value of the minimal S-matrix eigenvalue is very close to zero. Specifically, considering the vector $\vec{n}_{\text{ant}} = (\text{Re}(n_{\text{ant}}), \text{Im}(n_{\text{ant}}))^T$, we iterate

$$\vec{n}_{\text{ant}}^{\,(i+1)} = \vec{n}_{\text{ant}}^{\,(i)} - \delta s \vec{\nabla} \Lambda_{\text{min}}(\vec{n}_{\text{ant}}^{\,(i)}) \tag{6.6}$$

with an adaptive step size δs until we find a pair of $\text{Re}(n_{\text{ant}})$ and $\text{Im}(n_{\text{ant}})$ for which the absolute value of the minimal S-matrix eigenvalue Λ_{min} is smaller than 10^{-10}. For the scattering configuration in Fig. 6.2, the resulting refractive index of the absorbing scatterer is $n_{\text{ant}} = 3.086 + 1.051i$.

To check whether the eigenstate corresponding to the obtained minimal S-matrix eigenvalue is indeed a CPA state, we perform simulations of the time-reversed scenario (in the absence of global absorption): Similar to the injection through the central antenna, we place an emitting point source inside the corresponding antenna scatterer which serves as a good approximation since the latter is small. A point source corresponds to $f \propto \delta(\vec{r} - \vec{r}_{\text{ps}})$ with $\vec{r}_{\text{ps}}$ being the point source position which we implement as an evaluation of the test function in the first term on the right-hand side of Eq. (2.18) at a single mesh point that is added in the center of the absorbing scatterer[19]. Using such a point source and turning the absorbing scatterer's loss into the corresponding amount of gain, we find an intensity correlation between the CPA state and its time-reverse that is unity up to 10^{-14}.

To verify that the numerically found CPA state coincides with the experimentally obtained one, we measure the electric field on a 5×5 mm grid around the central absorbing antenna and compute the correlation of the corresponding intensity profile with the numerically obtained one. For a meaningful comparison, we also map the numerically obtained wave field with high resolution to the same coarse 5×5 mm grid as in the experiment. Furthermore, since the field cannot be measured in the close vicinity of the central antenna or at the positions of the Teflon scatterers, we exclude these points from the data set. The resulting experimental and pixelated numerical spatial intensity distributions are shown in Fig. 6.4(a), where we see a striking similarity that can be quantified by a correlation of 95.63%.

---

[19] Alternatively, one can also choose f to be either a constant or Gaussian function with a very small but finite extent whose spatial integral evaluates to one.

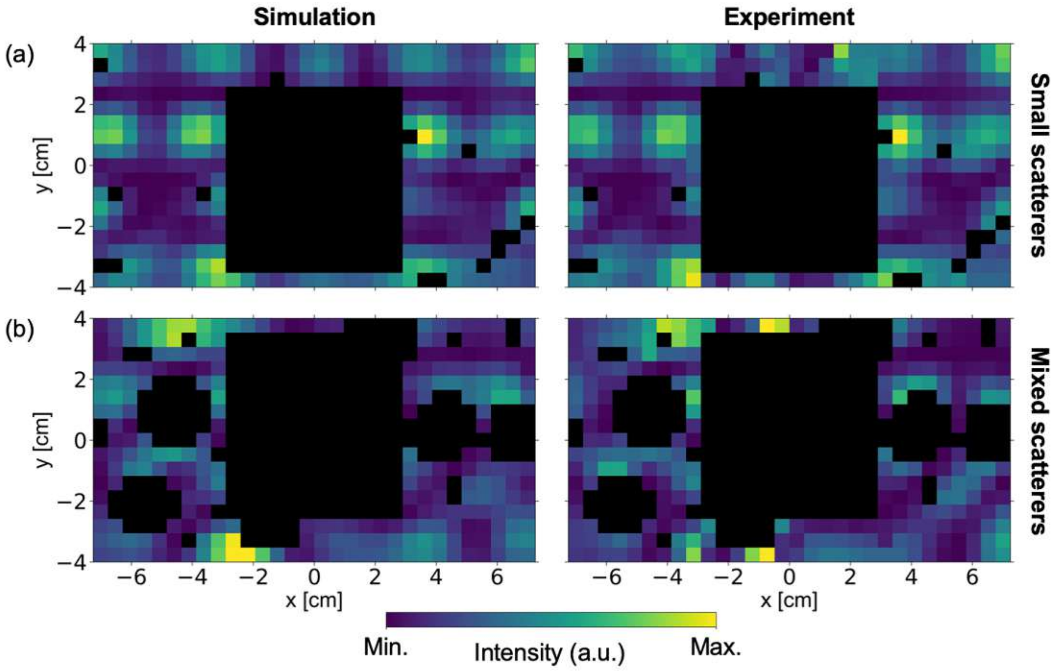

Figure 6.4: Comparison of the numerically obtained (left panels) and experimentally measured (right panels) intensity distributions of the CPA state in the configuration with (a) 60 small scatterers (with radius $r = 2.55$ mm) and (b) 60 mixed scatterers (with radii $r = 2.55$ mm and 11 mm). For a meaningful comparison, the numerical solution defined on a very fine mesh was read out on the coarse measurement grid, where each pixel corresponds to an area of 5×5 mm. The experimentally inaccessible areas in the close vicinity of the central absorbing antenna and at the scatterer positions are colored black. The numerical simulations have been performed in absence of global absorption resulting in intensity correlation values of 95.63% and 83.42% in the configuration with 60 small and 60 mixed scatterers, respectively.

Next, we demonstrate that this high degree of similarity cannot be attributed to the rather weak scattering strength of the configuration in Fig. 6.2 which can be characterized by a scattering and transport mean free path of $\ell_s \approx \ell^* \approx 1.3$ m $\approx 2.17L$. To increase the scattering strength, we use a mixture of 28 small and 32 large Teflon scatterers with radii of $r = 2.55$ mm and $r = 11$ mm, respectively, which are again randomly distributed in the scattering region. Since the diameter of the larger scatterers is much closer to the operating wavelength $\lambda \approx 43$ mm, both the scattering and the transport mean free path are now strongly reduced. Specifically, they are given by $\ell_s \approx 0.08$ m $\approx 0.13L$ and $\ell^* \approx 0.2$ m $\approx 0.33L$ which are now both substantially smaller than the length of the scattering region L. For this strongly scattering configuration, the experimentally determined CPA frequency is 6.9 GHz at which $I_{\text{out}}/I_{\text{in}} = 2.1 \times 10^{-3}$. Applying the gradient-based optimization in the numerical simulations at the experimentally found CPA frequency then results in $n_{\mathrm{ant}} = 3.336 + 1.244i$. The resulting numerically obtained spatial intensity distribution of the corresponding CPA state in this configuration is now compared to the experimentally measured one in Fig. 6.4(b), where their high correlation of 83.42% is again clearly visible.

In both scattering configurations, we observe a slight deviation from perfect correlation which can be attributed to uncertainties of about 1 mm in the experimental scatterer placement. Since strongly scattering configurations are more sensitive to such deviations, this also explains the slightly lower correlation in the configuration with the mixed scatterers compared to the configuration with only small scatterers. Another aspect we neglected in our numerical simulations is global absorption in the waveguide as it can typically be considered weak. However, when taking global absorption based on the material parameters of our aluminum waveguide into account (following [178]), we find that the intensity correlation values of the CPA states in the two considered configurations remain unchanged on the percent level. This rather weak effect of global absorption can be attributed to the loss incurred at the central antenna which is much more dominant than the weak dissipation in the waveguide. However, in strongly scattering configurations featuring long dwell times, this weak effect can also give rise to CPA caused by global absorption (see supplementary material of [60]). Specifically, the correlation values in the presence of global absorption are 95.57% and 83.44% in the configuration with 60 small and 60 mixed scatterers, respectively.

This remarkable degree of agreement enables us to investigate the full wave functions as well as the flux patterns of the numerically obtained CPA states which are shown in Fig. 6.5 for both scattering configurations. The intensity distribution of the CPA state in the configuration with 60 small scatterers (left panel) shows small interference maxima due to the weak scattering and a very narrow and pronounced peak exactly at the position of the absorbing scatterer (marked by the white arrow). This indicates that the local dwell time inside the absorbing scatterer is very large in order to cause perfect absorption. The spatial distribution of the time-averaged Poynting vector (see Appendix E) then clearly shows, that the flux is fully directed towards the absorbing scatterer (filled white circle), i.e., no flux leaves this scatterer due to the perfect absorption. Similarly, the CPA state's spatial intensity distribution in the configuration with 60 mixed scatterers (right panel) also shows interference maxima that are much more pronounced due to the stronger scattering caused by the larger obstacles. However, also in this case we observe a very narrow and pronounced peak at the position of the absorbing scatterer as a result of the long local dwell time as well as a Poynting flux that is fully directed towards the absorber.

An experimental signature of such a Poynting flux behavior is the transmission into the central absorbing antenna which should be maximal at the CPA frequency. As shown in Fig. 6.6, we indeed observe this behavior for both the weak and the

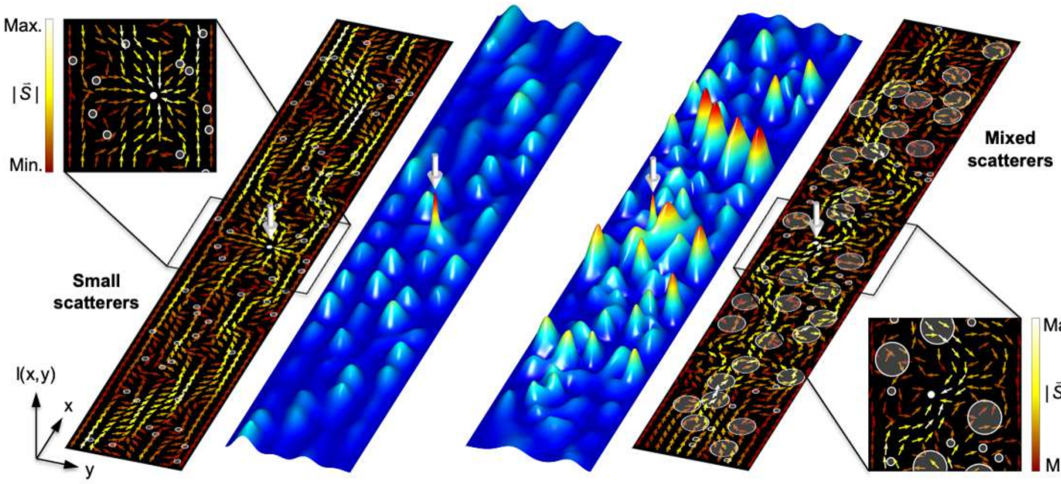

Figure 6.5: Spatial Poynting vector and intensity distributions of the numerically obtained CPA states in a weakly scattering configuration with 60 small scatterers (left panel) and a more strongly scattering configuration with 60 mixed scatterers (right panel) in the absence of global absorption. A white (red) vector color corresponds to a high (low) magnitude of the Poynting vector, and red (blue) colors in the intensity distributions correspond to high (low) intensity values. The vertical white arrow marks the position of the central absorbing antenna implemented as an absorbing scatterer in these two-dimensional simulations. The latter is depicted by a filled white circle and the semi-transparent circles represent the scatterers of the surrounding disorder. The insets show the Poynting vector distribution around the absorbing scatterer, where the color scale is adjusted to the local Poynting vector magnitude in this region. In both configurations, a pronounced peak can be seen in the spatial intensity distribution at the position of the absorbing scatterer indicating a locally enhanced dwell time. The corresponding Poynting flux is directed exclusively to this scatterer which is a result of the perfect absorption that prohibits any flux from leaving the absorber.

strong scattering configuration. Removing all the surrounding scatterers then drastically reduces the transmission into this antenna since CPA states are customized for specific scatterer configurations.

Last, we want to emphasize that the intensity peaks of the CPA states at the position of the absorbing scatterer (marked by the white arrow in the top panels of Fig. 6.7) are not diffraction-limited spots, but rather have sub-wavelength dimensions. This behavior can be explained in terms of Green's functions [179]: The radiation of a point source is described by the causal (retarded) Green's function that describes an outgoing diverging wave. On the other hand, there also exists the anti-causal (advanced) Green's function which describes an incoming converging wave. In contrast to a diverging wave, a converging wave is never observed alone since it cannot stop propagating at its focal point in free space, but continues

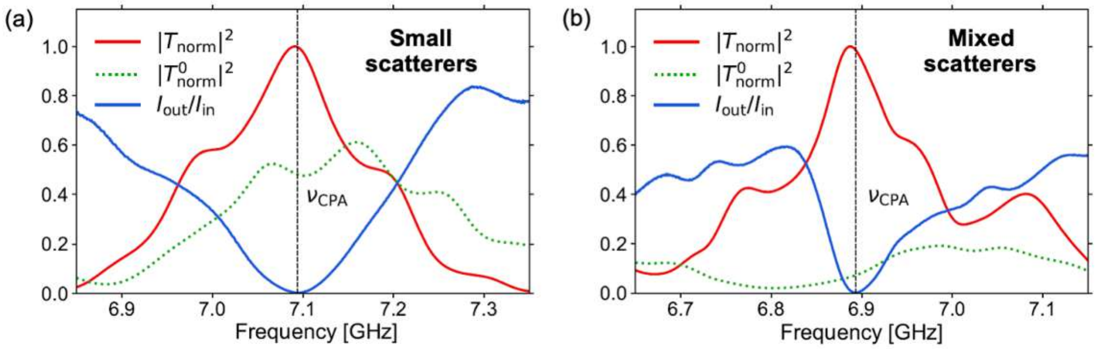

Figure 6.6: Measured transmission of the CPA states into the central absorbing antenna as a function of the frequency for the configuration with (a) 60 small scatterers and (b) 60 mixed scatterers. In both configurations, the normalized transmission into the central antenna $|T_{\mathrm{norm}}|^2$ reaches its maximum at exactly the CPA frequency ν_{CPA}, i.e., the frequency at which the ratio of outgoing to incoming intensity $I_{\mathrm{out}}/I_{\mathrm{in}}$ reaches its minimum. As a reference, we also plot the transmission of the same CPA state into the central antenna $|T^0_{\mathrm{norm}}|^2$ when all scatterers that form the surrounding disorder are removed (using the same normalization). In this case, the transmission into the central antenna is drastically reduced since CPA states are tailored to specific disorder configurations.

propagation as a diverging wave. The superposition of these two waves then results in a focal spot which is diffraction-limited. As shown in Ref. [179], this limitation can be overcome by eliminating the outgoing wave, which can be achieved by fully time-reversing the point source scenario. More precisely, turning the outgoing diverging wave into an incoming converging wave and replacing the point source with a point sink leads to perfect absorption of the incoming wave at the sink, resulting in a focal spot with sub-wavelength dimensions.

Coming back to CPA, the absorbing scatterer corresponds to the point sink in the above described scenario which fully dissipates the wave. Thus, despite the presence of a complex scattering environment, CPA eliminates all outgoing waves, resulting in an intensity peak at the absorber position with sub-wavelength dimensions. Removing the absorbing scatterer again introduces an outgoing wave at its original position, whose superposition with the incoming wave should result in a diffraction-limited focal spot which is exactly what we observe in Fig. 6.7 (bottom panels).

Die approbierte gedruckte Originalversion dieser Dissertation ist an der TU Wien Bibliothek verfügbar.
The approved original version of this doctoral thesis is available in print at TU Wien Bibliothek.
TU Bibliothek Your knowledge hub WIEN

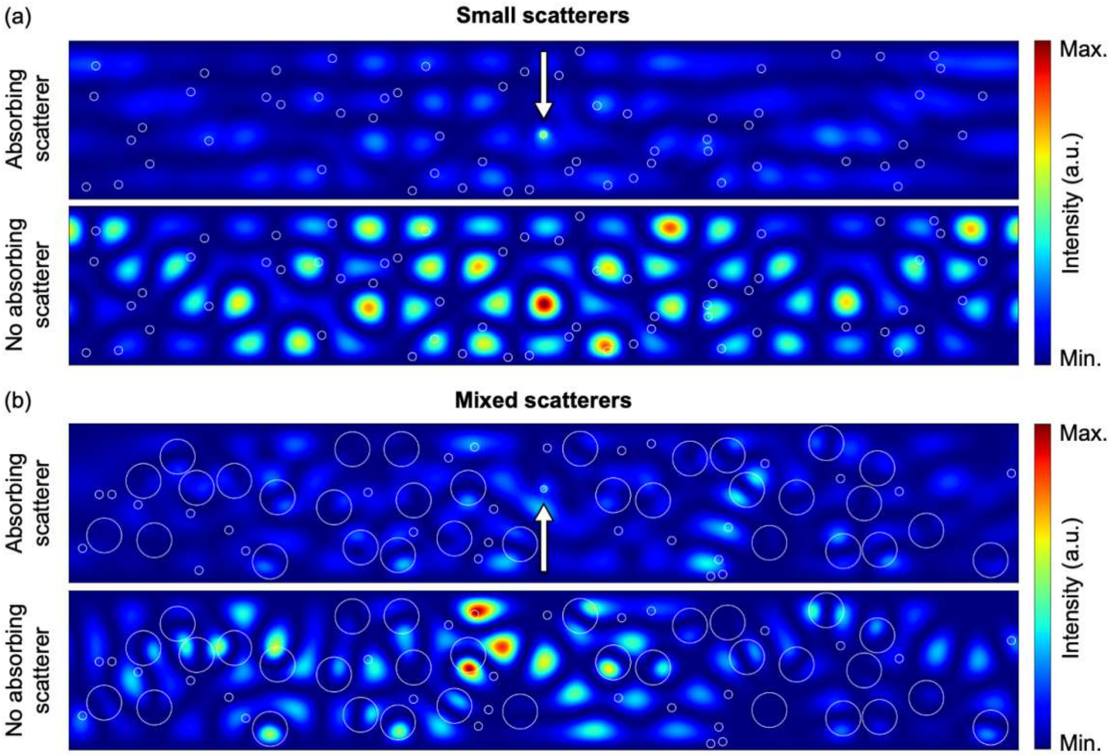

Figure 6.7: Spatial intensity distributions of the CPA states in the configuration with (a) 60 small and (b) 60 mixed scatterers in presence (top panels) and absence (bottom panels) of the absorbing scatterer (all other parameters and the color scale stay unchanged). The scatterers are indicated as white circles and the absorbing scatterer is marked by a white arrow. The presence of the absorbing scatterer causes perfect absorption resulting in an intensity peak with sub-wavelength dimensions, while its removal changes the latter to a diffraction-limited focal spot. Moreover, removing the absorbing scatterer also causes considerably higher and differently distributed intensity maxima in the waveguide, stemming from additional interference contributions of the waves that are no longer absorbed.

6.2 Conclusion

We present the first experimental realization of a random anti-laser, which provides a proof of principle that CPA can be realized in arbitrarily composed systems such as disordered media. Our approach only relies on the multi-modal scattering matrix and does not require information about the inner local structure of the medium. Moreover, it does not rely on sources like guide-stars [26] inside the medium which are typically used for focusing inside disordered structures. In this context we emphasize that the effect of CPA is highly relevant for focusing electromagnetic signals [8] or sound fields [3] in complex environments like an office space or biological tissue. Furthermore, its high sensitivity with respect to the field's degrees of freedom can be exploited for creating tunable absorbers that can in turn be used as optical switches. Beyond that, CPA can also be used for filtering specific frequencies or modes. On the other hand, a broad bandwidth might be desirable, e.g., for telecommunications-related applications and thus the search for broadband CPAs will also be subject of future research [161, 180]. Another interesting observation is the very narrow peak in the CPA state's intensity distribution at the position of the absorber which has sub-wavelength dimensions making the effect of CPA also highly relevant for sub-wavelength focusing [174, 181]. Instead of tuning the frequency and absorption strength, one can also consider the opposite scenario of keeping these quantities fixed and optimizing the medium which then makes it possible to create CPA on demand [162, 182]. However, real-world applications might not allow for tweaking a system's scattering properties and thus another interesting extension of this work could investigate the related effect of coherent *virtual* absorption [183–185] in multi-mode disordered systems. Thereby, the full suppression of outgoing fields is achieved by injecting an exponentially growing wave in time whose growth is determined by the imaginary part of an S-matrix zero in the absence of material loss making it possible to store the energy of the incoming waves for arbitrary amounts of time. Thus, the effect of CPA opens up many new exciting possibilities which will serve as a bridge between the communities of wavefront shaping and non-Hermitian physics.

Summary and outlook

As we show in this thesis, the detrimental effects caused by the presence of disorder can be overcome by means of wavefront shaping. Exploiting the information stored in the experimentally accessible scattering matrix, we extend the concept of Wigner-Smith time-delay and introduce novel classes of wave states that perform at an optimal level.

In order to test these newly introduced concepts, we develop a flexible numerical tool in the first part of this thesis, which allows us to obtain full-wave solutions in waveguide-like geometries using the finite element method. Based on the very general framework for solving partial differential equations provided by the open-source software package NGSolve, we first develop the solution strategy for the scalar Helmholtz equation in two dimensions which we then extend to the full-vectorial three-dimensional case, where we solve the vector Helmholtz equation in order to capture all the physics contained in Maxwell's equations. The obtained solutions are then used to calculate the scattering matrices of the considered systems.

The first concept we introduce is based on the Wigner-Smith time-delay operator which we generalize to a whole new class of operators by replacing the frequency derivative with a derivative with respect to an arbitrary parameter. By choosing different parameters, we demonstrate analytically, numerically and experimentally in a microwave setup that the corresponding eigenstates transfer a well-defined amount of angular, radial or linear momentum to a target enabling the optimal control of the applied torque, pressure or force. Moreover, it also enables the creation of wave states that store a well-defined amount of intensity inside a target which opens up the possibility to optimally focus inside of it. Our approach is independent of the target size and shape and even works if the target is embedded in a strongly scattering medium. Furthermore, it is based on a simple eigenvalue problem that only depends on the asymptotic information stored in the scattering matrix which makes it very attractive for real-world applications. In particular, we are confident that the presented concept will be useful in the field of optical micromanipulation, where arbitrary target shapes and a surrounding disorder are still major challenges. Moreover, its application to the cooling of a moving gas of particles, its close connection to the Fisher information as well as its extension to time-periodic systems make us confident that it will find many applications in a wide variety of research areas with one of the ultimate goals being the optimal spatio-temporal manipulation of targets in fully time-dependent systems.

The second novel class of waves we introduce in this thesis are special states of light that propagate through a scattering medium in a similar way as they propagate through a homogeneous medium yielding the same output pattern up to a global amplitude and phase. These scattering invariant modes can be obtained via a generalized eigenvalue problem that is closely related to the above-introduced generalization of the Wigner-Smith concept. We investigate their defining feature of the similarity of the output patters after propagation through air or through a dense scattering layer of zinc oxide particles experimentally in an optical setup and verify the obtained results numerically. Furthermore, we also show numerically as well as experimentally that these modes preferentially propagate through scatter-free areas in sparse scattering samples, just like ballistic light would do. Therefore, these special states of light embody the defining feature of ballistic light which can be used to improve scanning fluorescence imaging, as we show. Scattering invariant modes have already been extended to transmission matrices covering different input and output angles (rather than different materials) enabling the design of desired memories for imaging applications which – together with the presented results – makes us belief that this concept has great potential for further improving current optical and ultrasound imaging techniques. Beyond that, future applications could also exploit their property of avoiding scatterers to overcome imperfections, e.g., in optical elements.

Revisiting the concept of time-delay, we also investigate the mean time that waves dwell inside scattering media in the ballistic, diffusive and localized regime of disorder scattering. Although there exist system-specific optimal states with largest and smallest time-delays, the mean time-delay of waves is counter-intuitively invariant with respect to the scattering properties of a system and solely depends on its geometry which is a result of its intimate relation to the density of states. We show numerically as well as experimentally, that this invariance property holds in all transport regimes of disorder scattering and even applies to periodic structures that feature transmission band gaps. Moreover, we investigate the effect of absorption on the mean time-delay and find that strong absorption causes a convergence towards the most direct paths in transmission and reflection. Our results provide a comprehensive bound on the mean path length in scattering media and are thus deeply linked to the Yablonovitch limit making it relevant for the design of structures that enhance light-matter interaction or the efficiency of light harvesting complexes. Since absorption is essential for the mentioned applications and is furthermore intimately related to the dwell time, we also envision an extension of the presented results to the invariance of the mean absorption in scattering media.

In the last part of this thesis, we remain in the realm of non-Hermitian physics and search for special wave states that are perfectly absorbed at a localized loss element inside a disordered material. Utilizing the phenomenon of coherent perfect absorption, we show numerically as well as experimentally in a microwave setup that precisely adjusting the absorption strength, the frequency as well as the shape of the incident wavefront can lead to perfect dissipation as a result of the interplay between absorption and interference. As the other concepts introduced in this thesis, this approach also relies solely on the experimentally accessible scattering matrix without the need of information about the inner structure of the medium. In terms of applications, coherent perfect absorption is highly relevant for focusing electromagnetic signals or sound fields in complex environments like an office space or biological tissue. Furthermore, the observed sub-wavelength dimension of the wave's intensity peak at the absorber position makes this effect also interesting for the field of sub-wavelength focusing. The already existing extensions of these results for achieving perfect absorption on demand by optimizing the medium are very promising for real-world applications in which the absorption strength might not be tunable. Moreover, a generalization of the related effect of coherent virtual absorption to two-dimensional disordered media would also be highly beneficial as this would fully eliminate the need of tunable absorption or system parameters. Last, since light in real-world applications might not be monochromatic, the extension to broadband coherent perfect absorbers is also highly desirable.

We hope that the results presented in this thesis set the stage for exciting new developments in the rapidly evolving field of wavefront shaping. Since the scattering matrix fully characterizes a scattering process, we believe that the information stored therein has considerable potential for future innovations that expand the range of novel and optimal classes of wave states which can be used to overcome or even benefit from the effects of complex environments.

TU Bibliothek WIEN Your knowledge hub
Die approbierte gedruckte Originalversion dieser Dissertation ist an der TU Wien Bibliothek verfügbar.
The approved original version of this doctoral thesis is available in print at TU Wien Bibliothek.

Appendix

A Derivation of wave equations

In the following, we derive the equations describing stationary, time-harmonic, electromagnetic scattering problems in linear, isotropic and inhomogeneous media. We start from the macroscopic Maxwell equations (in SI units)

$$\vec{\nabla} \cdot \vec{D}(\vec{r}, t) = \rho_f(\vec{r}, t) \,, \tag{A.1}$$

$$\vec{\nabla} \cdot \vec{B}(\vec{r}, t) = 0 \,, \tag{A.2}$$

$$\vec{\nabla} \times \vec{E}(\vec{r}, t) = -\frac{\partial \vec{B}(\vec{r}, t)}{\partial t} \,, \tag{A.3}$$

$$\vec{\nabla} \times \vec{H}(\vec{r}, t) = \vec{j}_f(\vec{r}, t) + \frac{\partial \vec{D}(\vec{r}, t)}{\partial t} \,, \tag{A.4}$$

in which $\vec{D}$ is the displacement field (or electric flux density), $\vec{E}$ is the electric field strength, $\vec{B}$ is the magnetic flux density and $\vec{H}$ is the magnetic field strength. Moreover, ρ_f and $\vec{j}_f$ are the free charge and free current density, respectively, and we assume a source-free medium in the following, i.e., $\rho_f = 0$ and $\vec{j}_f = 0$. Equations (A.1)-(A.4) further give rise to the following interface conditions between two media:

$$\vec{n} \cdot (\vec{D}_2 - \vec{D}_1) = \rho_s \,, \tag{A.5}$$

$$\vec{n} \cdot (\vec{B}_2 - \vec{B}_1) = 0 \,, \tag{A.6}$$

$$\vec{n} \times (\vec{E}_2 - \vec{E}_1) = \vec{0} \,, \tag{A.7}$$

$$\vec{n} \times (\vec{H}_2 - \vec{H}_1) = \vec{j}_s \,, \tag{A.8}$$

where $\vec{n}$ is the outward normal vector of medium 1 pointing into medium 2 and ρ_s and $\vec{j}_s$ are the surface charge and surface flux density, respectively. Equations (A.6) and (A.7) imply the continuity of the normal component of $\vec{B}$ and the tangential component of $\vec{E}$, whereas Eqs. (A.5) and (A.8) imply that the normal component of $\vec{D}$ and the tangential component of $\vec{H}$ can be discontinuous.

The so-called constitutive relations connect the $\vec{D}$- with the $\vec{E}$-field and the $\vec{B}$-with the $\vec{H}$-field. For a linear medium, they are given by

$$\vec{D}(\vec{r},t) = \varepsilon_0 \boldsymbol{\varepsilon}_r(\vec{r},t)\vec{E}(\vec{r},t)\,, \tag{A.9}$$

$$\vec{B}(\vec{r},t) = \mu_0 \boldsymbol{\mu}_r(\vec{r},t)\vec{H}(\vec{r},t)\,, \tag{A.10}$$

Here, ε_0 and μ_0 are the (scalar) vacuum permittivity and permeability, respectively, whereas $\boldsymbol{\varepsilon}_r$ and $\boldsymbol{\mu}_r$ are the relative permittivity and permeability tensors. Since we only consider static and non-magnetic materials, $\boldsymbol{\varepsilon}_r(\vec{r},t) = \boldsymbol{\varepsilon}_r(\vec{r})$ and $\boldsymbol{\mu}_r(\vec{r},t) = \boldsymbol{\mu}_r(\vec{r}) = \mathbb{1}$. Depending on the permittivity tensor, one can now classify materials as follows: Materials with a permittivity tensor proportional to the unit matrix are called isotropic, whereas media with a diagonal permittivity tensor with two (three) different diagonal elements are called uniaxial (biaxial). A structure without any symmetry does not feature a special permittivity tensor and is thus called anisotropic. In the following, we only consider isotropic materials, for which the permittivity tensor can simply be replaced by a spatially-dependent scalar, i.e., $\boldsymbol{\varepsilon}_r(\vec{r}) \to \varepsilon_r(\vec{r})$. Last, we also consider non-dispersive materials for which $\varepsilon_r(\vec{r})$ is independent of the frequency ω.

We now apply the curl-operation to Eq. (A.3), use $\vec{B}(\vec{r},t) = \mu_0\vec{H}(\vec{r},t)$ and insert Eq. (A.4) to arrive at the vector wave equation

$$\vec{\nabla}\times\vec{\nabla}\times\vec{E}(\vec{r},t) + \frac{n^2(\vec{r})}{c^2}\frac{\partial^2\vec{E}(\vec{r},t)}{\partial t^2} = -\mu_0\frac{\partial\vec{j}_i(\vec{r},t)}{\partial t}\,, \tag{A.11}$$

where we introduced an impressed current density $\vec{j}_i(\vec{r},t)$ on the right-hand side of Eq. (A.4) that serves as a source. Furthermore, $c = 1/\sqrt{\varepsilon_0\mu_0}$ is the speed of light and $n(\vec{r}) = \sqrt{\varepsilon_r(\vec{r})\mu_r(\vec{r})}$ is the spatially-dependent refractive index distribution with $\mu_r(\vec{r}) = 1$. Next, we assume a time-harmonic field and current density, i.e., $\vec{E}(\vec{r},t) = \vec{E}(\vec{r})e^{-i\omega t}$ and $\vec{j}_i(\vec{r},t) = \vec{j}_i(\vec{r})e^{-i\omega t}$ at a frequency $\omega = kc$, yielding the vector Helmholtz equation

$$\vec{\nabla}\times\vec{\nabla}\times\vec{E}(\vec{r}) - n^2(\vec{r})k^2\vec{E}(\vec{r}) = \vec{f}(\vec{r}) \tag{A.12}$$

with $\vec{f}(\vec{r}) = i\omega\mu_0\vec{j}_i(\vec{r})$ whose numerical solution with the FEM is outlined in Section 2.2. To further simplify this equation, we make use of the identity $\vec{\nabla}\times\vec{\nabla}\times\vec{V} = \vec{\nabla}(\vec{\nabla}\cdot\vec{V}) - \vec{\nabla}\cdot(\vec{\nabla}\vec{V})$ and get

$$\Delta\vec{E}(\vec{r}) - \vec{\nabla}\left[\vec{\nabla}\cdot\vec{E}(\vec{r})\right] + n^2(\vec{r})k^2\vec{E}(\vec{r}) = -\vec{f}(\vec{r})\,, \tag{A.13}$$

where Δ is the Laplace operator in three dimensions. Using $\vec{D}(\vec{r}) = \varepsilon_0\varepsilon_r(\vec{r})\vec{E}(\vec{r})$, we can rewrite Eq. (A.1) as

$$\begin{aligned}\vec{\nabla}\cdot\vec{E}(\vec{r}) &= -\frac{1}{\varepsilon(\vec{r})}\vec{\nabla}\varepsilon(\vec{r})\cdot\vec{E}(\vec{r}) \\ &= -\vec{\nabla}\ln[\varepsilon(\vec{r})]\cdot\vec{E}(\vec{r})\,.\end{aligned} \tag{A.14}$$

Inserting this into Eq. (A.13) results in

$$\Delta\vec{E}(\vec{r}) + \vec{\nabla}\left\{\vec{\nabla}\ln[\varepsilon(\vec{r})]\cdot\vec{E}(\vec{r})\right\} + n^2(\vec{r})k^2\vec{E}(\vec{r}) = -\vec{f}(\vec{r})\,. \tag{A.15}$$

Next, we consider an electric field which is polarized in the z-direction, i.e., $\vec{E}(\vec{r}) = (0,0,\psi(\vec{r}))^T$. As outlined in Section 1.3, this assumption is valid in waveguides whose height is very low, since in this case only TE_{m0} modes can propagate whose electric field is only non-vanishing in the z-polarization. Last, assuming an effective 2D medium for which $\varepsilon(\vec{r}) = \varepsilon(x,y)$ yields a permittivity gradient that lies in the xy-plane. Thus, $\vec{\nabla}\ln[\varepsilon(\vec{r})]\cdot\vec{E}(\vec{r}) = 0$ results in the scalar Helmholtz equation

$$\left[\Delta + n^2(\vec{r})k^2\right]\psi(\vec{r}) = -f(\vec{r}) \tag{A.16}$$

for the z-component of the electric field $\psi(\vec{r}) \equiv E_z(\vec{r})$ and the source $f(\vec{r}) \equiv f_z(\vec{r})$ (the numerical solution of this equation with the FEM is described in Section 2.1).

B Relation between line source and excitation amplitudes

To derive the relation between the line source amplitudes and the amplitudes of the actual excitation inside the waveguide, we start by defining the wave function of the excitation $\psi(\vec{r})$ as a superposition of flux-normalized modes on the left and right side of the input line

$$\psi_L(\vec{r}) = \sum_n^{N_m} \frac{a_n}{\sqrt{k_{x,n}}}\chi_n(y)\,e^{-ik_{x,n}x}\,, \tag{B.1}$$

$$\psi_R(\vec{r}) = \sum_n^{N_m} \frac{b_n}{\sqrt{k_{x,n}}}\chi_n(y)\,e^{+ik_{x,n}x}\,, \tag{B.2}$$

respectively. Demanding the continuity of the wave function at the input line which we choose to be at $x = 0$, i.e., $\psi_L(0) = \psi_R(0)$, then yields

$$\sum_n^{N_m} \frac{a_n}{\sqrt{k_{x,n}}}\chi_n = \sum_n^{N_m} \frac{b_n}{\sqrt{k_{x,n}}}\chi_n\,. \tag{B.3}$$

Multiplying with χ_k^*, integrating over y and using the orthonormality of our transverse basis functions

$$\int dy\,\chi_k^*\chi_n = \delta_{kn} \tag{B.4}$$

then yields the equality of the amplitudes of the left- and right-traveling waves, i.e.,

$$a_n = b_n\,. \tag{B.5}$$

To relate these amplitudes with the amplitudes of a line source at $x = 0$, we use the scalar Helmholtz equation with a source term that consists of a similar superposition of waveguide modes as in Eq. (B.2), but with different amplitudes c_n, i.e.,

$$(\Delta + n^2k^2)\psi = -\left(\sum_n^{N_m} \frac{c_n}{\sqrt{k_{x,n}}}\chi_n\right)\delta(x)\,. \tag{B.6}$$

Integrating over a small distance $\pm\varepsilon$ in x then gives

$$\int_{-\varepsilon}^{\varepsilon} \frac{\partial^2\psi}{\partial x^2}\,dx + \int_{-\varepsilon}^{\varepsilon} \frac{\partial^2\psi}{\partial y^2} + n^2k^2\psi\,dx = -\sum_n^{N_m} \frac{c_n}{\sqrt{k_{x,n}}}\chi_n\,. \tag{B.7}$$

Next, taking the limit $\varepsilon \to 0$ makes the second integral on the left-hand side of Eq. (B.7) vanish (due to the continuity of the integrand) leaving us with

$$\left.\frac{\partial\psi_R}{\partial x}\right|_{x=0} - \left.\frac{\partial\psi_L}{\partial x}\right|_{x=0} = -\sum_n^{N_m} \frac{c_n}{\sqrt{k_{x,n}}}\chi_n\,. \tag{B.8}$$

Inserting the spatial derivatives of Eqs. (B.1) and (B.2) together with Eq. (B.5) gives

$$\sum_n^{N_m} 2ik_{x,n}\frac{a_n}{\sqrt{k_{x,n}}}\chi_n = -\sum_n^{N_m} \frac{c_n}{\sqrt{k_{x,n}}}\chi_n\,. \tag{B.9}$$

Multiplying with χ_k^*, integrating over y and applying Eq. (B.4) finally results in the relation between the line source amplitudes c_n and the excitation amplitudes a_n:

$$c_n = -2ik_{x,n}a_n\,. \tag{B.10}$$

This relation also holds in the three-dimensional case in which the above derivation has to be carried out with the full-vectorial modes.

C Generalized Wigner-Smith operator for non-regular matrices

The construction of the generalized Wigner-Smith operators $q_\theta^{(S)} = -iS^{-1}dS/d\theta$, $q_\theta^{(t)} = -it^{-1}dt/d\theta$ and $q_\theta^{(r)} = -ir^{-1}dr/d\theta$ involves the inversion of the scattering, transmission and reflection matrix, respectively. However, the latter might be singular as a result of strong absorption inside the system or due losses caused by scattering into channels that are not considered in the scattering matrix (e.g., scattering into steep angles that cannot be measured). In this case, zero-eigenvalues make the corresponding matrix non-invertible, whereas an ordinary inverse also does not exist if the matrices themselves are of rectangular shape. However, these problems can be solved by projecting, e.g., the transmission matrix onto the subspace of highly transmitting eigenstates which in turn allows the calculation of its so-called *pseudo-inverse*. To set up the necessary projection operators, we use the singular value decomposition of the transmission matrix $t = U\Sigma V^\dagger$ in which $U = (\vec{u}_1, \vec{u}_2, \ldots, \vec{u}_N)$ and $V = (\vec{v}_1, \vec{v}_2, \ldots, \vec{v}_N)$ are unitary matrices which contain column-wise the left and right singular vectors of t, respectively, and $\Sigma = \mathrm{diag}(\{\sigma_n\})$ is a diagonal matrix that contains the real and non-negative singular values σ_n. If t is a $M \times N$ matrix, the matrices U and V have dimensions $M \times M$ and $N \times N$, respectively, whereas Σ is a rectangular $M \times N$ matrix. The left singular vectors of t (contained in U) correspond to the orthogonal eigenvectors of $tt^\dagger$, the right singular vectors (contained in V) are the orthogonal eigenvectors of $t^\dagger t$ and the singular values σ_n are the square-roots of the common eigenvalues of $tt^\dagger$ and $t^\dagger t$. In case of a singular or rectangular transmission matrix, we proceed with transforming t into the non-singular eigenspace via $\widetilde{U}^\dagger t\widetilde{V} = \widetilde{\Sigma}$. Here, $\widetilde{U}$ and $\widetilde{V}$ correspond to the matrices U and V in which singular vectors, i.e., columns, corresponding to singular values smaller than a chosen threshold σ_{thr} are discarded, and $\widetilde{\Sigma}$ is the diagonal matrix in which the corresponding singular values have been removed. For the threshold, we typically use $\sigma_{\mathrm{thr}} = 10^{-10}$. This projection then allows a regular inversion of the matrix $\widetilde{\Sigma}$, where a subsequent back-transformation into the original vector space yields the following expression for the pseudo-inverse

$$\begin{aligned} \widetilde{t}^{-1} &= \widetilde{V}\widetilde{\Sigma}^{-1}\widetilde{U}^\dagger \\ &= \widetilde{V}(\widetilde{U}^\dagger t\widetilde{V})^{-1}\widetilde{U}^\dagger\,. \end{aligned} \tag{C.1}$$

Projecting also the derivative of the transmission matrix onto the non-singular subspace using the projection operators $P_{\widetilde{U}} = \widetilde{U}\widetilde{U}^\dagger$ and $P_{\widetilde{V}} = \widetilde{V}\widetilde{V}^\dagger$ yields the following expression for the projected generalized Wigner-Smith operator:

$$q_\theta^{(t)} = \widetilde{V}(\widetilde{U}^\dagger t\widetilde{V})^{-1}\widetilde{U}^\dagger\,\widetilde{U}\widetilde{U}^\dagger\frac{dt}{d\theta}\widetilde{V}\widetilde{V}^\dagger\,. \tag{C.2}$$

Note that exactly the same procedure can also be applied to $q_\theta^{(S)}$ and $q_\theta^{(r)}$. Denoting N_s the number of singular values below the threshold, the eigenvalues of the operator in Eq. (C.2) contain N_s zero eigenvalues which have to be discarded together with the corresponding eigenvectors since they are non-physical remnants of the projection procedure. Note that in case of a non-singular matrix, the subspace is equal to the whole eigenspace of the considered matrix, i.e., $\widetilde{U} = U$ and $\widetilde{V} = V$, in which case Eq. (C.2) reduces to the original expression $q_\theta^{(t)} = -it^{-1}dt/d\theta$ of the GWS operator since the projection operators become $P_{\widetilde{U}} = \mathbb{1}$ and $P_{\widetilde{V}} = \mathbb{1}$. However, if singular vectors are discarded, $P_{\widetilde{U}} = \widetilde{U}\widetilde{U}^\dagger \neq \mathbb{1}$ and $P_{\widetilde{V}} = \widetilde{V}\widetilde{V}^\dagger \neq \mathbb{1}$, but $\widetilde{U}^\dagger\widetilde{U} = \mathbb{1}$ and $\widetilde{V}^\dagger\widetilde{V} = \mathbb{1}$ still holds.

D Determination of mean free paths

The scattering properties of a disordered system can typically be characterized by two length scales: the transport mean free path ℓ^* and the scattering mean free path ℓ_s. The transport mean free path characterizes the macroscopic transport properties and measures the length at which the direction of an incoming photon is entirely randomized, whereas the scattering mean free path describes the average distance between two scattering events on a microscopic level. These two length scales are related via $\ell^* = \ell_s/(1-g)$, where $g = \langle \cos\Theta \rangle$ is the so-called anisotropy parameter that describes the average of the cosine of the scattering angle Θ [10]. In case of sub-wavelength obstacles, the isotropic scattering causes $g = 0$ and thus $\ell^* = \ell_s$.

To determine the transport mean free path in the numerical simulations of our disordered waveguide systems, we calculate the scattering matrices of many random configurations with the same density and size distribution of scatterers. Next, we randomly concatenate many of these scattering matrices until we reach the localized regime in which the average transmission decays exponentially, i.e.,

$$\langle \ln T \rangle \approx -\frac{L}{\xi}\,, \tag{D.1}$$

where $T = \mathrm{Tr}(t^\dagger t)/N$ is the average transmission with t being the $N \times N$ transmission matrix for N propagating modes and ξ is the localization length. Therefore, averaging the logarithm of T for each length of concatenated scattering sections over many random configurations and fitting $\langle \ln T \rangle$ to the linear decay $-L/\xi$ yields the localization length ξ which is in quasi-1D systems (like the waveguides considered in this thesis) related to the transport mean free path via $\xi \approx N\ell^*$ [10].

To estimate the scattering mean free path, we split the disordered waveguide into shorter subsections with a proportionally smaller number of included scatterers. We further choose these subsections such that waves still propagate ballistically in them (transmission is still above 90%). We then quantify how much an incoming mode is scattered into other modes by studying the decrease of the diagonal transmission elements $T_{nn} = |t_{nn}|^2$ which is linear in the ballistic regime, i.e.,

$$\langle T_{nn} \rangle \approx 1 - \frac{L}{\ell_{s,n}}\,, \tag{D.2}$$

where we average over many random configurations. Extracting the mode-specific scattering mean free paths $\ell_{s,n}$ and further averaging over all modes then yields the average scattering mean free path $\ell_s = \langle \ell_{s,n} \rangle$.

E Time-averaged Poynting vector

To determine the flux of a stationary state, we start with the general definition of the Poynting vector

$$\vec{S}(\vec{r},t) = \vec{E}(\vec{r},t) \times \vec{H}(\vec{r},t)\,. \tag{E.1}$$

Employing the harmonic time-dependence of stationary solutions, i.e., $\vec{E}(\vec{r},t) = \vec{E}(\vec{r})e^{-i\omega t}$ and $\vec{H}(\vec{r},t) = \vec{H}(\vec{r})e^{-i\omega t}$, and using the fact that only the real parts of these solution describe the physical fields, the Poynting vector can be written as

$$\begin{aligned}\vec{S}(\vec{r},t) =& \operatorname{Re}\left[\vec{E}(\vec{r})e^{-i\omega t}\right] \times \operatorname{Re}\left[\vec{H}(\vec{r})e^{-i\omega t}\right]\\ =& \vec{E}_r(\vec{r}) \times \vec{H}_r(\vec{r})\cos^2(\omega t) + \vec{E}_r(\vec{r}) \times \vec{H}_i(\vec{r})\cos(\omega t)\sin(\omega t)\\ &+ \vec{E}_i(\vec{r}) \times \vec{H}_i(\vec{r})\sin^2(\omega t) + \vec{E}_i(\vec{r}) \times \vec{H}_r(\vec{r})\sin(\omega t)\cos(\omega t)\,,\end{aligned} \tag{E.2}$$

where the subscripts r and i denote the real and imaginary part of the corresponding fields, respectively. Averaging this expression over one period in time then yields

$$\begin{aligned}\vec{S}(\vec{r}) &= \int_0^{\frac{2\pi}{\omega}} \vec{S}(\vec{r},t)\,dt\\ &= \frac{1}{2}\left[\vec{E}_r(\vec{r}) \times \vec{H}_r(\vec{r}) + \vec{E}_i(\vec{r}) \times \vec{H}_i(\vec{r})\right].\end{aligned} \tag{E.3}$$

By adding specially constructed purely imaginary terms and taking only the real part of the resulting expression, the time-averaged Poynting vector can be written in terms of the total $\vec{E}$- and $\vec{H}$-field:

$$\begin{aligned}\vec{S} &= \frac{1}{2}\operatorname{Re}\left(\vec{E}_r \times \vec{H}_r + \vec{E}_i \times \vec{H}_i + i\vec{E}_i \times \vec{H}_r - i\vec{E}_r \times \vec{H}_i\right)\\ &= \frac{1}{2}\operatorname{Re}\left[(\vec{E}_r + i\vec{E}_i) \times (\vec{H}_r - i\vec{H}_i)\right]\\ &= \frac{1}{2}\operatorname{Re}\left(\vec{E} \times \vec{H}^*\right).\end{aligned} \tag{E.4}$$

Since all involved quantities in the above expression do not depend on time anymore, we have also omitted the spatial dependence for readability. Equation (E.4) can now be used to calculate the Poynting flux in the three-dimensional vectorial case. In the two-dimensional scalar case, we can further simplify Eq. (E.4) by considering a z-polarized electric field $\vec{E} = (0,0,\psi)^T$. Using Maxwell's equation (A.3) in the time-harmonic case with $\mu_r = 1$, we can calculate the corresponding $\vec{H}$-field resulting in $\vec{H} = \frac{1}{\omega\mu_0}(-i\partial_y\psi, i\partial_x\psi, 0)^T$. Inserting everything into Eq. (E.4) then finally yields

$$\begin{aligned}\vec{S} &= \frac{1}{2\omega\mu_0}\operatorname{Re}\left[\psi(-i\vec{\nabla}\psi)^*\right]\\ &= \frac{1}{2\omega\mu_0}\operatorname{Re}\left[\psi^*(-i\vec{\nabla}\psi)\right].\end{aligned} \tag{E.5}$$

Bibliography

[1] A. Derode, A. Tourin, J. de Rosny, M. Tanter, S. Yon, and M. Fink. “Taking Advantage of Multiple Scattering to Communicate with Time-Reversal Antennas”. *Phys. Rev. Lett.* **90**, 014301 (2003).

[2] A. Aubry, A. Derode, P. Roux, and A. Tourin. “Coherent backscattering and far-field beamforming in acoustics”. *The Journal of the Acoustical Society of America* **121**, 70–77 (2007).

[3] G. Ma, X. Fan, P. Sheng, and M. Fink. “Shaping reverberating sound fields with an actively tunable metasurface”. *Proceedings of the National Academy of Sciences* **115**, 6638–6643 (2018).

[4] A. Przadka, S. Feat, P. Petitjeans, V. Pagneux, A. Maurel, and M. Fink. “Time Reversal of Water Waves”. *Phys. Rev. Lett.* **109**, 064501 (2012).

[5] A. Chabchoub and M. Fink. “Time-Reversal Generation of Rogue Waves”. *Phys. Rev. Lett.* **112**, 124101 (2014).

[6] G. Lerosey, J. de Rosny, A. Tourin, A. Derode, G. Montaldo, and M. Fink. “Time Reversal of Electromagnetic Waves”. *Phys. Rev. Lett.* **92**, 193904 (2004).

[7] O. Dietz, U. Kuhl, H.-J. Stöckmann, N. M. Makarov, and F. M. Izrailev. “Microwave realization of quasi-one-dimensional systems with correlated disorder”. *Phys. Rev. B* **83**, 134203 (2011).

[8] N. Kaina, M. Dupré, G. Lerosey, and M. Fink. “Shaping complex microwave fields in reverberating media with binary tunable metasurfaces”. *Scientific Reports* **4**, 6693 (2014).

[9] A. P. Mosk, A. Lagendijk, G. Lerosey, and M. Fink. “Controlling waves in space and time for imaging and focusing in complex media”. *Nature Photonics* **6**, 283–292 (2012).

[10] S. Rotter and S. Gigan. “Light fields in complex media: Mesoscopic scattering meets wave control”. *Rev. Mod. Phys.* **89**, 015005 (2017).

[11] S. Gigan, O. Katz, H. B. de Aguiar, E. R. Andresen, A. Aubry, J. Bertolotti, E. Bossy, D. Bouchet, J. Brake, S. Brasselet, Y. Bromberg, H. Cao, T. Chaigne, Z. Cheng, W. Choi, T. Čižmár, M. Cui, V. R. Curtis, H. Defienne, M. Hofer, R. Horisaki, R. Horstmeyer, N. Ji, A. K. LaViolette, J. Mertz, C. Moser, A. P. Mosk, N. C. Pégard, R. Piestun, S. Popoff, D. B. Phillips, D. Psaltis, B. Rahmani, H. Rigneault, S. Rotter, L. Tian, I. M. Vellekoop, L. Waller, L. Wang, T. Weber, S. Xiao, C. Xu, A. Yamilov, C. Yang, and H. Yılmaz. “Roadmap on Wavefront Shaping and deep imaging in complex media”. *arXiv*:2111.14908 [physics.optics] (2021).

[12] N. Savage. “Digital spatial light modulators”. *Nature Photonics* **3**, 170–172 (2009).

[13] C. Maurer, A. Jesacher, S. Bernet, and M. Ritsch-Marte. “What spatial light modulators can do for optical microscopy”. *Laser & Photonics Reviews* **5**, 81–101 (2011).

[14] E. G. van Putten, I. M. Vellekoop, and A. P. Mosk. “Spatial amplitude and phase modulation using commercial twisted nematic LCDs”. *Appl. Opt.* **47**, 2076–2081 (2008).

[15] D. B. Conkey, A. M. Caravaca-Aguirre, and R. Piestun. “High-speed scattering medium characterization with application to focusing light through turbid media”. *Opt. Express* **20**, 1733–1740 (2012).

[16] S. A. Goorden, J. Bertolotti, and A. P. Mosk. “Superpixel-based spatial amplitude and phase modulation using a digital micromirror device”. *Opt. Express* **22**, 17999–18009 (2014).

[17] S. M. Popoff, G. Lerosey, R. Carminati, M. Fink, A. C. Boccara, and S. Gigan. “Measuring the Transmission Matrix in Optics: An Approach to the Study and Control of Light Propagation in Disordered Media”. *Phys. Rev. Lett.* **104**, 100601 (2010).

[18] E. G. van Putten and A. P. Mosk. “The information age in optics: Measuring the transmission matrix”. *Physics* **3**, 22 (2010).

[19] H. Yu, T. R. Hillman, W. Choi, J. O. Lee, M. S. Feld, R. R. Dasari, and Y. Park. “Measuring Large Optical Transmission Matrices of Disordered Media”. *Phys. Rev. Lett.* **111**, 153902 (2013).

[20] I. M. Vellekoop and A. P. Mosk. “Focusing coherent light through opaque strongly scattering media”. *Opt. Lett.* **32**, 2309–2311 (2007).

[21] F. van Beijnum, E. G. van Putten, A. Lagendijk, and A. P. Mosk. “Frequency bandwidth of light focused through turbid media”. *Opt. Lett.* **36**, 373–375 (2011).

[22] I. M. Vellekoop and A. P. Mosk. “Universal Optimal Transmission of Light Through Disordered Materials”. *Phys. Rev. Lett.* **101**, 120601 (2008).

[23] S. Popoff, G. Lerosey, M. Fink, A. C. Boccara, and S. Gigan. “Image transmission through an opaque material”. *Nature Communications* **1**, 81 (2010).

[24] S. M. Popoff, G. Lerosey, M. Fink, A. C. Boccara, and S. Gigan. “Controlling light through optical disordered media: transmission matrix approach”. *New Journal of Physics* **13**, 123021 (2011).

[25] T. Chaigne, O. Katz, A. C. Boccara, M. Fink, E. Bossy, and S. Gigan. “Controlling light in scattering media non-invasively using the photoacoustic transmission matrix”. *Nature Photonics* **8**, 58–64 (2014).

[26] R. Horstmeyer, H. Ruan, and C. Yang. “Guidestar-assisted wavefront-shaping methods for focusing light into biological tissue”. *Nature Photonics* **9**, 563–571 (2015).

[27] J. Aulbach, B. Gjonaj, P. M. Johnson, A. P. Mosk, and A. Lagendijk. “Control of Light Transmission through Opaque Scattering Media in Space and Time”. *Phys. Rev. Lett.* **106**, 103901 (2011).

[28] O. Katz, E. Small, Y. Bromberg, and Y. Silberberg. “Focusing and compression of ultrashort pulses through scattering media”. *Nature Photonics* **5**, 372–377 (2011).

[29] D. J. McCabe, A. Tajalli, D. R. Austin, P. Bondareff, I. A. Walmsley, S. Gigan, and B. Chatel. “Spatio-temporal focusing of an ultrafast pulse through a multiply scattering medium”. *Nature Communications* **2**, 447 (2011).

[30] M. Mounaix, D. Andreoli, H. Defienne, G. Volpe, O. Katz, S. Grésillon, and S. Gigan. “Spatiotemporal Coherent Control of Light through a Multiple Scattering Medium with the Multispectral Transmission Matrix”. *Phys. Rev. Lett.* **116**, 253901 (2016).

[31] M. Mounaix, H. Defienne, and S. Gigan. “Deterministic light focusing in space and time through multiple scattering media with a time-resolved transmission matrix approach”. *Phys. Rev. A* **94**, 041802 (2016).

[32] M. Mounaix. “Matricial approaches for spatio-temporal control of light in multiple scattering media”. PhD thesis. Laboratoire Kastler Brossel, 2018.

[33] E. H. Zhou, H. Ruan, C. Yang, and B. Judkewitz. “Focusing on moving targets through scattering samples”. *Optica* **1**, 227–232 (2014).

[34] C. Ma, X. Xu, Y. Liu, and L. V. Wang. “Time-reversed adapted-perturbation (TRAP) optical focusing onto dynamic objects inside scattering media”. *Nature Photonics* **8**, 931–936 (2014).

[35] L. Eisenbud. “The Formal Properties of Nuclear Collisions.” PhD thesis. Princeton University, 1948.

[36] E. P. Wigner. “Lower Limit for the Energy Derivative of the Scattering Phase Shift”. *Phys. Rev.* **98**, 145–147 (1955).

[37] F. T. Smith. “Lifetime Matrix in Collision Theory”. *Phys. Rev.* **118**, 349–356 (1960).

[38] E. H. Hauge and J. A. Støvneng. “Tunneling times: a critical review”. *Rev. Mod. Phys.* **61**, 917–936 (1989).

[39] B. A. van Tiggelen, A. Tip, and A. Lagendijk. “Dwell times for light and electrons”. *Journal of Physics A: Mathematical and General* **26**, 1731–1748 (1993).

[40] S. Fan and J. M. Kahn. “Principal modes in multimode waveguides”. *Opt. Lett.* **30**, 135–137 (2005).

[41] J. Carpenter, B. J. Eggleton, and J. Schröder. “Observation of Eisenbud–Wigner–Smith states as principal modes in multimode fibre”. *Nature Photonics* **9**, 751–757 (2015).

[42] W. Xiong, P. Ambichl, Y. Bromberg, B. Redding, S. Rotter, and H. Cao. “Spatiotemporal Control of Light Transmission through a Multimode Fiber with Strong Mode Coupling”. *Phys. Rev. Lett.* **117**, 053901 (2016).

[43] W. Xiong, P. Ambichl, Y. Bromberg, B. Redding, S. Rotter, and H. Cao. “Principal modes in multimode fibers: exploring the crossover from weak to strong mode coupling”. *Opt. Express* **25**, 2709–2724 (2017).

[44] P. Ambichl, W. Xiong, Y. Bromberg, B. Redding, H. Cao, and S. Rotter. “Super- and Anti-Principal-Modes in Multimode Waveguides”. *Phys. Rev. X* **7**, 041053 (2017).

[45] S. Rotter, P. Ambichl, and F. Libisch. “Generating Particlelike Scattering States in Wave Transport”. *Phys. Rev. Lett.* **106**, 120602 (2011).

[46] B. Gérardin, J. Laurent, P. Ambichl, C. Prada, S. Rotter, and A. Aubry. “Particlelike wave packets in complex scattering systems”. *Phys. Rev. B* **94**, 014209 (2016).

[47] J. Böhm, A. Brandstötter, P. Ambichl, S. Rotter, and U. Kuhl. “In situ realization of particlelike scattering states in a microwave cavity”. *Phys. Rev. A* **97**, 021801 (2018).

[48] P. Ambichl. “Delay Times and Beam-Like Scattering States in Coherent Wave Transmission Through Resonators”. Master thesis. Vienna University of Technology (TU Wien), 2012.

[49] M. Durand, S. M. Popoff, R. Carminati, and A. Goetschy. “Optimizing Light Storage in Scattering Media with the Dwell-Time Operator”. *Phys. Rev. Lett.* **123**, 243901 (2019).

[50] P. del Hougne, R. Sobry, O. Legrand, F. Mortessagne, U. Kuhl, and M. Davy. "Experimental Realization of Optimal Energy Storage in Resonators Embedded in Scattering Media". *Laser & Photonics Reviews* **15**, 2000335 (2021).

[51] V. Lyuboshitz. "On collision duration in the presence of strong overlapping resonance levels". *Physics Letters B* **72**, 41–44 (1977).

[52] S. Souma and A. Suzuki. "Local density of states and scattering matrix in quasi-one-dimensional systems". *Phys. Rev. B* **65**, 115307 (2002).

[53] R. Pierrat, P. Ambichl, S. Gigan, A. Haber, R. Carminati, and S. Rotter. "Invariance property of wave scattering through disordered media". *Proceedings of the National Academy of Sciences* **111**, 17765–17770 (2014).

[54] R. Savo, R. Pierrat, U. Najar, R. Carminati, S. Rotter, and S. Gigan. "Observation of mean path length invariance in light-scattering media". *Science* **358**, 765–768 (2017).

[55] M. Horodynski, M. Kühmayer, A. Brandstötter, K. Pichler, Y. V. Fyodorov, U. Kuhl, and S. Rotter. "Optimal wave fields for micromanipulation in complex scattering environments". *Nature Photonics* **14**, 149–153 (2020).

[56] P. Ambichl, A. Brandstötter, J. Böhm, M. Kühmayer, U. Kuhl, and S. Rotter. "Focusing inside Disordered Media with the Generalized Wigner-Smith Operator". *Phys. Rev. Lett.* **119**, 033903 (2017).

[57] P. Pai, J. Bosch, M. Kühmayer, S. Rotter, and A. P. Mosk. "Scattering invariant modes of light in complex media". *Nature Photonics* **15**, 431–434 (2021).

[58] M. Davy, M. Kühmayer, S. Gigan, and S. Rotter. "Mean path length invariance in wave-scattering beyond the diffusive regime". *Communications Physics* **4**, 85 (2021).

[59] Y. D. Chong, L. Ge, H. Cao, and A. D. Stone. "Coherent Perfect Absorbers: Time-Reversed Lasers". *Phys. Rev. Lett.* **105**, 053901 (2010).

[60] K. Pichler, M. Kühmayer, J. Böhm, A. Brandstötter, P. Ambichl, U. Kuhl, and S. Rotter. "Random anti-lasing through coherent perfect absorption in a disordered medium". *Nature* **567**, 351–355 (2019).

[61] Y. D. Chong and A. D. Stone. "Hidden Black: Coherent Enhancement of Absorption in Strongly Scattering Media". *Phys. Rev. Lett.* **107**, 163901 (2011).

[62] P. Pai, J. Bosch, and A. P. Mosk. "Optical transmission matrix measurement sampled on a dense hexagonal lattice". *OSA Continuum* **3**, 637–648 (2020).

[63] J. Carpenter, B. J. Eggleton, and J. Schröder. "110x110 optical mode transfer matrix inversion". *Opt. Express* **22**, 96–101 (2014).

[64] M. Åbom. “Measurement of the scattering-matrix of acoustical two-ports”. *Mechanical Systems and Signal Processing* **5**, 89–104 (1991).

[65] W. Lambert, L. A. Cobus, M. Couade, M. Fink, and A. Aubry. “Reflection Matrix Approach for Quantitative Imaging of Scattering Media”. *Phys. Rev. X* **10**, 021048 (2020).

[66] W. Lambert, L. A. Cobus, M. Fink, and A. Aubry. “Ultrasound Matrix Imaging. I. The focused reflection matrix and the F-factor”. *arXiv*:2103.02029 [physics.app-ph] (2021).

[67] B. Gérardin, J. Laurent, A. Derode, C. Prada, and A. Aubry. “Full Transmission and Reflection of Waves Propagating through a Maze of Disorder”. *Phys. Rev. Lett.* **113**, 173901 (2014).

[68] H.-J. Stöckmann. *Quantum Chaos*. Cambridge University Press, 1999.

[69] L. E. Reichl. *Transition to Chaos*. 2nd ed. Springer, 2004.

[70] H. G. Winful. “Delay Time and the Hartman Effect in Quantum Tunneling”. *Phys. Rev. Lett.* **91**, 260401 (2003).

[71] P. Ambichl. “Coherent Wave Transport: Time-Delay and Beyond”. PhD thesis. Vienna University of Technology (TU Wien), 2016.

[72] G. Iannaccone. “General relation between density of states and dwell times in mesoscopic systems”. *Phys. Rev. B* **51**, 4727–4729 (1995).

[73] M. Bartelmann, B. Feuerbach, T. Krüger, D. Lüst, A. Rebhan, and W. Andreas. *Theoretische Physik*. Springer-Verlag Berlin, 2015.

[74] J. Schöberl. “NETGEN An advancing front 2D/3D-mesh generator based on abstract rules”. *Computing and Visualization in Science* **1**, 41–52 (1997).

[75] J. Schöberl. *C++11 Implementation of Finite Elements in NGSolve*. ASC Report, Institute for Analysis and Scientific Computing, Vienna University of Technology. 2014.

[76] D. B. Davidson. *Computational Electromagnetics for RF and Microwave Engineering*. 2nd ed. Cambridge University Press, 2010.

[77] J.-M. Jin. *The Finite Element Method in Electromagnetics*. 3rd ed. John Wiley and Sons, 2014.

[78] F.-J. Sayas. *A gentle introduction to the Finite Element Method*. 2015.

[79] J. Schöberl. *Numerical Methods for Maxwell Equations*. 2009.

[80] S. G. Johnson. “Notes on Perfectly Matched Layers (PMLs)”. *arXiv*:2108.05348 [cs.CE] (2021).

[81] D. S. Fisher and P. A. Lee. “Relation between conductivity and transmission matrix”. *Phys. Rev. B* **23**, 6851–6854 (1981).

[82] S. Datta. *Electronic Transport in Mesoscopic Systems*. Cambridge University Press, 1995.

[83] T. Rylander, P. Ingelström, and A. Bondeson. *Computational Electromagnetics*. 2nd ed. Springer, 2013.

[84] J. C. Nedelec. "Mixed finite elements in ℝ3". *Numerische Mathematik* **35**, 315–341 (1980).

[85] J. Webb. "Edge elements and what they can do for you". *IEEE Transactions on Magnetics* **29**, 1460–1465 (1993).

[86] G. Mur. "Edge elements, their advantages and their disadvantages". *IEEE Transactions on Magnetics* **30**, 3552–3557 (1994).

[87] M. Kühmayer. "Particlelike states in D-shaped fibers". Master thesis. Vienna University of Technology (TU Wien), 2016.

[88] X. Cheng and A. Z. Genack. "Focusing and energy deposition inside random media". *Opt. Lett.* **39**, 6324–6327 (2014).

[89] G. Thalhammer, R. Steiger, S. Bernet, and M. Ritsch-Marte. "Optical macro-tweezers: trapping of highly motile micro-organisms". *J. Opt.* **13**, 044024 (2011).

[90] R. Bowman, A. Jesacher, G. Thalhammer, G. Gibson, M. Ritsch-Marte, and M. Padgett. "Position clamping in a holographic counterpropagating optical trap". *Opt. Express* **19**, 9908–9914 (2011).

[91] A. Jannasch, M. Mahamdeh, and E. Schäffer. "Inertial Effects of a Small Brownian Particle Cause a Colored Power Spectral Density of Thermal Noise". *Phys. Rev. Lett.* **107**, 228301 (2011).

[92] D. Palima and J. Glückstad. "Gearing up for optical microrobotics: micromanipulation and actuation of synthetic microstructures by optical forces". *Laser & Photonics Reviews* **7**, 478–494 (2013).

[93] D. B. Phillips, J. A. Grieve, S. N. Olof, S. J. Kocher, R. Bowman, M. J. Padgett, M. J. Miles, and D. M. Carberry. "Surface imaging using holographic optical tweezers". *Nanotechnology* **22**, 285503 (2011).

[94] U. G. Būtaitė, G. M. Gibson, Y.-L. D. Ho, M. Taverne, J. M. Taylor, and D. B. Phillips. "Indirect optical trapping using light driven micro-rotors for reconfigurable hydrodynamic manipulation". *Nature Communications* **10**, 1215 (2019).

[95] F. Strasser, S. Moser, M. Ritsch-Marte, and G. Thalhammer. "Direct measurement of individual optical forces in ensembles of trapped particles". *Optica* **8**, 79–87 (2021).

[96] S. Kheifets, A. Simha, K. Melin, T. Li, and M. G. Raizen. “Observation of Brownian Motion in Liquids at Short Times: Instantaneous Velocity and Memory Loss”. *Science* **343**, 1493–1496 (2014).

[97] T. Li. *Fundamental Tests of Physics with Optically Trapped Microspheres.* Springer, 2013.

[98] A. Ashkin, J. M. Dziedzic, J. E. Bjorkholm, and S. Chu. “Observation of a single-beam gradient force optical trap for dielectric particles”. *Opt. Lett.* **11**, 288–290 (1986).

[99] P. H. Jones, O. M. Maragò, and G. Volpe. *Optical Tweezers: Principles and Applications.* Cambridge University Press, 2015.

[100] K. Dholakia, P. Reece, and M. Gu. “Optical micromanipulation”. *Chem. Soc. Rev.* **37**, 42–55 (2008).

[101] C. J. Bustamante, Y. R. Chemla, S. Liu, and M. D. Wang. “Optical tweezers in single-molecule biophysics”. *Nature Reviews Methods Primers* **1**, 25 (2021).

[102] A. Jesacher, C. Maurer, A. Schwaighofer, S. Bernet, and M. Ritsch-Marte. “Full phase and amplitude control of holographic optical tweezers with high efficiency”. *Opt. Express* **16**, 4479–4486 (2008).

[103] K. Dholakia and T. Čižmár. “Shaping the future of manipulation”. *Nature Photonics* **5**, 335–342 (2011).

[104] H. Rubinsztein-Dunlop, A. Forbes, M. V. Berry, M. R. Dennis, D. L. Andrews, M. Mansuripur, C. Denz, C. Alpmann, P. Banzer, T. Bauer, E. Karimi, L. Marrucci, M. Padgett, M. Ritsch-Marte, N. M. Litchinitser, N. P. Bigelow, C. Rosales-Guzmán, A. Belmonte, J. P. Torres, T. W. Neely, M. Baker, R. Gordon, A. B. Stilgoe, J. Romero, A. G. White, R. Fickler, A. E. Willner, G. Xie, B. McMorran, and A. M. Weiner. “Roadmap on structured light”. *Journal of Optics* **19**, 013001 (2016).

[105] Y. Yang, Y. Ren, M. Chen, Y. Arita, and C. Rosales-Guzmán. “Optical trapping with structured light: a review”. *Advanced Photonics* **3**, (2021).

[106] T. Čižmár, M. Mazilu, and K. Dholakia. “In situ wavefront correction and its application to micromanipulation”. *Nature Photonics* **4**, 388–394 (2010).

[107] M. Polin, K. Ladavac, S.-H. Lee, Y. Roichman, and D. G. Grier. “Optimized holographic optical traps”. *Opt. Express* **13**, 5831–5845 (2005).

[108] M. A. Taylor, M. Waleed, A. B. Stilgoe, H. Rubinsztein-Dunlop, and W. P. Bowen. “Enhanced optical trapping via structured scattering”. *Nature Photonics* **9**, 669–673 (2015).

[109] Y. E. Lee, O. D. Miller, M. T. H. Reid, S. G. Johnson, and N. X. Fang. "Computational inverse design of non-intuitive illumination patterns to maximize optical force or torque". *Opt. Express* **25**, 6757–6766 (2017).

[110] M. W. Matthès, Y. Bromberg, J. de Rosny, and S. M. Popoff. "Learning and Avoiding Disorder in Multimode Fibers". *Phys. Rev. X* **11**, 021060 (2021).

[111] M. Kaczvinszki, N. Bachelard, J. Hüpfl, M. Horodynski, M. Kühmayer, and S. Rotter. "Optimal Cooling of Multiple Levitated Particles through Far-Field Wavefront-Shaping". *arXiv*:2103.12592 [physics.optics] (2021).

[112] D. Bouchet, S. Rotter, and A. P. Mosk. "Maximum information states for coherent scattering measurements". *Nature Physics* **17**, 564–568 (2021).

[113] M. Horodynski, D. Bouchet, M. Kühmayer, and S. Rotter. "Invariance Property of the Fisher Information in Scattering Media". *Phys. Rev. Lett.* **127**, 233201 (2021).

[114] D. Globosits. "The Floquet Wigner-Smith Operator for Time-Periodic Systems". Master thesis. Vienna University of Technology (TU Wien), 2021.

[115] P. J. Forrester and T. Nagao. "Eigenvalue Statistics of the Real Ginibre Ensemble". *Phys. Rev. Lett.* **99**, 050603 (2007).

[116] A. Goetschy and A. D. Stone. "Filtering Random Matrices: The Effect of Incomplete Channel Control in Multiple Scattering". *Phys. Rev. Lett.* **111**, 063901 (2013).

[117] L. V. Wang and H. Wu. *Biomedical Optics: Principles and Imaging*. Wiley, 2007.

[118] V. Ntziachristos. "Going deeper than microscopy: the optical imaging frontier in biology". *Nature Methods* **7**, 603–614 (2010).

[119] W. Drexler and J. Fujimoto, eds. *Optical Coherence Tomography: Technology and Applications*. Springer International Publishing, 2015.

[120] M. Kim, Y. Choi, C. Yoon, W. Choi, J. Kim, Q.-H. Park, and W. Choi. "Maximal energy transport through disordered media with the implementation of transmission eigenchannels". *Nature Photonics* **6**, 581–585 (2012).

[121] A. Peña, A. Girschik, F. Libisch, S. Rotter, and A. A. Chabanov. "The single-channel regime of transport through random media". *Nature Communications* **5**, 3488 (2014).

[122] M. Davy, Z. Shi, J. Wang, X. Cheng, and A. Z. Genack. "Transmission Eigenchannels and the Densities of States of Random Media". *Phys. Rev. Lett.* **114**, 033901 (2015).

[123] M. Davy, J. Shi Zhou and Park, C. Tian, and A. Z. Genack. "Universal structure of transmission eigenchannels inside opaque media". *Nature Communications* **6**, 6893 (2015).

[124] H. Yılmaz, C. W. Hsu, A. Yamilov, and H. Cao. “Transverse localization of transmission eigenchannels”. *Nature Photonics* **13**, 352–358 (2019).

[125] H. Yılmaz, C. W. Hsu, A. Goetschy, S. Bittner, S. Rotter, A. Yamilov, and H. Cao. “Angular Memory Effect of Transmission Eigenchannels”. *Phys. Rev. Lett.* **123**, 203901 (2019).

[126] P. Mello, P. Pereyra, and N. Kumar. “Macroscopic approach to multichannel disordered conductors”. *Annals of Physics* **181**, 290–317 (1988).

[127] C. W. J. Beenakker. “Random-matrix theory of quantum transport”. *Rev. Mod. Phys.* **69**, 731–808 (1997).

[128] M. Davy, Z. Shi, J. Wang, and A. Z. Genack. “Transmission statistics and focusing in single disordered samples”. *Opt. Express* **21**, 10367–10375 (2013).

[129] S. Yoon, M. Kim, M. Jang, Y. Choi, W. Choi, S. Kang, and W. Choi. “Deep optical imaging within complex scattering media”. *Nature Reviews Physics* **2**, 141–158 (2020).

[130] J. Kubby, S. Gigan, and M. Cui, eds. *Wavefront Shaping for Biomedical Imaging*. Cambridge University Press, 2019.

[131] J. Bertolotti, E. G. van Putten, C. Blum, A. Lagendijk, W. L. Vos, and A. P. Mosk. “Non-invasive imaging through opaque scattering layers”. *Nature* **491**, 232–234 (2012).

[132] O. Katz, P. Heidmann, M. Fink, and S. Gigan. “Non-invasive single-shot imaging through scattering layers and around corners via speckle correlations”. *Nature Photonics* **8**, 784–790 (2014).

[133] S. Kang, P. Kang, S. Jeong, Y. Kwon, T. D. Yang, J. H. Hong, M. Kim, K.-D. Song, J. H. Park, J. H. Lee, M. J. Kim, K. H. Kim, and W. Choi. “High-resolution adaptive optical imaging within thick scattering media using closed-loop accumulation of single scattering”. *Nature Communications* **8**, 2157 (2017).

[134] M. Jang, Y. Horie, A. Shibukawa, J. Brake, Y. Liu, S. M. Kamali, A. Arbabi, H. Ruan, A. Faraon, and C. Yang. “Wavefront shaping with disorder-engineered metasurfaces”. *Nature Photonics* **12**, 84–90 (2018).

[135] R. Horisaki, Y. Mori, and J. Tanida. “Incoherent light control through scattering media based on machine learning and its application to multiview stereo displays”. *Optical Review* **26**, 709–712 (2019).

[136] A. Badon, V. Barolle, K. Irsch, A. C. Boccara, M. Fink, and A. Aubry. “Distortion matrix concept for deep optical imaging in scattering media”. *Science Advances* **6**, eaay7170 (2020).

[137] H. Yılmaz, M. Kühmayer, C. W. Hsu, S. Rotter, and H. Cao. “Customizing the Angular Memory Effect for Scattering Media”. *Phys. Rev. X* **11**, 031010 (2021).

[138] S. Blanco and R. Fournier. “An invariance property of diffusive random walks”. *Europhysics Letters* **61**, 168–173 (2003).

[139] K. Case and P. Zweifel. *Linear Transport Theory*. Addison-Wesley, 1967.

[140] A. Mazzolo. “Properties of diffusive random walks in bounded domains”. *Europhysics Letters* **68**, 350–355 (2004).

[141] O. Bénichou, M. Coppey, M. Moreau, P. H. Suet, and R. Voituriez. “Averaged residence times of stochastic motions in bounded domains”. *Europhysics Letters* **70**, 42–48 (2005).

[142] P. Dirac. *Approximate Rate of Neutron Multiplication for a Solid of Arbitrary Shape and Uniform Density*. Declassified British Report MS-D-5, Part I. 1943.

[143] M. Vasiliev, M. Nur-E-Alam, and K. Alameh. “Recent Developments in Solar Energy-Harvesting Technologies for Building Integration and Distributed Energy Generation”. *Energies* **12**, (2019).

[144] G. Frangipane, G. Vizsnyiczai, C. Maggi, R. Savo, A. Sciortino, S. Gigan, and R. Di Leonardo. “Invariance properties of bacterial random walks in complex structures”. *Nature Communications* **10**, 2442 (2019).

[145] P. W. Anderson. “Absence of Diffusion in Certain Random Lattices”. *Phys. Rev.* **109**, 1492–1505 (1958).

[146] A. Lagendijk, B. v. Tiggelen, and D. S. Wiersma. “Fifty years of Anderson localization”. *Physics Today* **62**, 24–29 (2009).

[147] E. Abrahams, ed. *50 Years of Anderson Localization*. 1st ed. World Scientific Publishing Company, 2010.

[148] E. Yablonovitch. “Photonic band-gap structures”. *J. Opt. Soc. Am. B* **10**, 283–295 (1993).

[149] H. Weyl. “Ueber die asymptotische Verteilung der Eigenwerte”. *Nachrichten von der Gesellschaft der Wissenschaften zu Göttingen, Mathematisch-Physikalische Klasse* **1911**, 110–117 (1911).

[150] W. Arendt, R. Nittka, W. Peter, F. Steiner, and W. Schleich. *Mathematical Analysis of Evolution, Information, and Complexity, Weyl's Law*. Wiley-VCH, Weinheim, Germany, 2009, 1–71.

[151] H. Weyl. “Über die Randwertaufgabe der Strahlungstheorie und asymptotische Spektralgesetzes”. *J. Reine Angew. Math.* **1913**, 177–202 (1913).

[152] S. M. Barnett and R. Loudon. “Sum Rule for Modified Spontaneous Emission Rates”. *Phys. Rev. Lett.* **77**, 2444–2446 (1996).

[153] J. Melchard. “Dwell Time and Intensity Enhancement: On the Connection Between Universal Time and the Yablonovitch Limit”. Bachelor thesis. Vienna University of Technology (TU Wien), 2015.

[154] R. Carminati and J. J. Sáenz. “Density of States and Extinction Mean Free Path of Waves in Random Media: Dispersion Relations and Sum Rules”. *Phys. Rev. Lett.* **102**, 093902 (2009).

[155] S. F. Liew, S. M. Popoff, A. P. Mosk, W. L. Vos, and H. Cao. “Transmission channels for light in absorbing random media: From diffusive to ballistic-like transport”. *Phys. Rev. B* **89**, 224202 (2014).

[156] E. Yablonovitch and G. D. Cody. “Intensity Enhancement in Textured Optical Sheets for Solar-Cells”. *IEEE Transactions on Electron Devices* **29**, 300–305 (1982).

[157] K. Vynck, M. Burresi, F. Riboli, and D. S. Wiersma. “Photon management in two-dimensional disordered media”. *Nature Materials* **11**, 1017–1022 (2012).

[158] D. V. Savin and H.-J. Sommers. “Delay times and reflection in chaotic cavities with absorption”. *Phys. Rev. E* **68**, 036211 (2003).

[159] S. Longhi. “$\mathcal{PT}$-symmetric laser absorber”. *Phys. Rev. A* **82**, 031801 (2010).

[160] W. Wan, Y. Chong, L. Ge, H. Noh, A. D. Stone, and H. Cao. “Time-Reversed Lasing and Interferometric Control of Absorption”. *Science* **331**, 889–892 (2011).

[161] D. G. Baranov, A. Krasnok, T. Shegai, A. Alù, and Y. Chong. “Coherent perfect absorbers: linear control of light with light”. *Nature Reviews Materials* **2**, 17064 (2017).

[162] P. del Hougne, K. B. Yeo, P. Besnier, and M. Davy. “On-Demand Coherent Perfect Absorption in Complex Scattering Systems: Time Delay Divergence and Enhanced Sensitivity to Perturbations”. *Laser & Photonics Reviews* **15**, 2000471 (2021).

[163] L. Chen, S. M. Anlage, and Y. V. Fyodorov. “Generalization of Wigner time delay to subunitary scattering systems”. *Phys. Rev. E* **103**, L050203 (2021).

[164] M. Pu, Q. Feng, M. Wang, C. Hu, C. Huang, X. Ma, Z. Zhao, C. Wang, and X. Luo. “Ultrathin broadband nearly perfect absorber with symmetrical coherent illumination”. *Opt. Express* **20**, 2246–2254 (2012).

[165] R. Bruck and O. L. Muskens. “Plasmonic nanoantennas as integrated coherent perfect absorbers on SOI waveguides for modulators and all-optical switches”. *Opt. Express* **21**, 27652–27661 (2013).

[166] Y. Sun, W. Tan, H.-q. Li, J. Li, and H. Chen. "Experimental Demonstration of a Coherent Perfect Absorber with PT Phase Transition". *Phys. Rev. Lett.* **112**, 143903 (2014).

[167] T. Roger, S. Vezzoli, E. Bolduc, J. Valente, J. J. F. Heitz, J. Jeffers, C. Soci, J. Leach, C. Couteau, N. I. Zheludev, and D. Faccio. "Coherent perfect absorption in deeply subwavelength films in the single-photon regime". *Nature Communications* **6**, 7031 (2015).

[168] Z. J. Wong, J. Xu Ye-Longand Kim, K. O'Brien, Y. Wang, L. Feng, and X. Zhang. "Lasing and anti-lasing in a single cavity". *Nature Photonics* **10**, 796–801 (2016).

[169] C. Meng, X. Zhang, S. T. Tang, M. Yang, and Z. Yang. "Acoustic Coherent Perfect Absorbers as Sensitive Null Detectors". *Scientific Reports* **7**, 43574 (2017).

[170] O. Richoux, V. Achilleos, G. Theocharis, and I. Brouzos. "Subwavelength Interferometric Control of Absorption in Three-port Acoustic Network". *Scientific Reports* **8**, 12328 (2018).

[171] H. Cao. "Lasing in random media". *Waves in Random Media* **13**, R1–R39 (2003).

[172] D. S. Wiersma. "The physics and applications of random lasers". *Nature Physics* **4**, 359–367 (2008).

[173] Y. V. Fyodorov, D. V. Savin, and H.-J. Sommers. "Scattering, reflection and impedance of waves in chaotic and disordered systems with absorption". *Journal of Physics A: Mathematical and General* **38**, 10731–10760 (2005).

[174] G. Lerosey, J. de Rosny, A. Tourin, and M. Fink. "Focusing Beyond the Diffraction Limit with Far-Field Time Reversal". *Science* **315**, 1120–1122 (2007).

[175] D. Gerlach and A. Paulraj. "Base station transmitter antenna arrays with mobile to base feedback". In: *Proceedings of 27th Asilomar Conference on Signals, Systems and Computers*. 1993, 1432–1436 vol.2.

[176] M. Cai, O. Painter, and K. J. Vahala. "Observation of Critical Coupling in a Fiber Taper to a Silica-Microsphere Whispering-Gallery Mode System". *Phys. Rev. Lett.* **85**, 74–77 (2000).

[177] J. R. Tischler, M. S. Bradley, and V. Bulović. "Critically coupled resonators in vertical geometry using a planar mirror and a 5 nm thick absorbing film". *Opt. Lett.* **31**, 2045–2047 (2006).

[178] J. D. Jackson. *Classical Electrodynamics*. 3rd ed. Wiley, 1998.

[179] G. Ma, X. Fan, F. Ma, J. de Rosny, P. Sheng, and M. Fink. “Towards anti-causal Green’s function for three-dimensional sub-diffraction focusing”. *Nature Physics* **14**, 608–612 (2018).

[180] S. Suwunnarat, Y. Tang, M. Reisner, F. Mortessagne, U. Kuhl, and T. Kottos. “Towards a Broad-Band Coherent Perfect Absorption in systems without Scale-Invariance”. *arXiv*:2103.03668 [physics.app-ph] (2021).

[181] J. de Rosny and M. Fink. “Overcoming the Diffraction Limit in Wave Physics Using a Time-Reversal Mirror and a Novel Acoustic Sink”. *Phys. Rev. Lett.* **89**, 124301 (2002).

[182] F. Russo. “Coherent perfect absorption in a disordered medium on demand”. Bachelor thesis. Vienna University of Technology (TU Wien), 2019.

[183] D. G. Baranov, A. Krasnok, and A. Alù. “Coherent virtual absorption based on complex zero excitation for ideal light capturing”. *Optica* **4**, 1457–1461 (2017).

[184] G. Trainiti, Y. Ra’di, M. Ruzzene, and A. Alù. “Coherent virtual absorption of elastodynamic waves”. *Science Advances* **5**, eaaw3255 (2019).

[185] Q. Zhong, L. Simonson, T. Kottos, and R. El-Ganainy. “Coherent virtual absorption of light in microring resonators”. *Phys. Rev. Research* **2**, 013362 (2020).

Acknowledgments

I acknowledge the Austrian Science Fund (FWF) for the financial support through the Project No. F49-P10 (SFB-NextLite) during the first year of my PhD. I am also grateful for the support from the European Commission under Project No. MSCA-RISE 691209 (NHQWAVE), which enabled my scientific stay at Yale University. Furthermore, I would like to thank the team around the Vienna Scientific Cluster (VSC) for granting me access which was essential for many results presented in this thesis.

Finally, I would like to thank all the people who have helped, encouraged and inspired me on this very exciting journey and without which this work would not have been possible:

- First and foremost I am sincerely grateful to Stefan Rotter who enabled me to work on all the very interesting topics covered in this thesis and who was always available, even in very stressful times. His enthusiasm for physics and his tireless efforts for excellent research were truly contagious, and his constant quest of understanding and explaining complex topics was inspiring and really shaped me as a scientist.

- I am also truly grateful for the excellent support of the NGSolve team around Joachim Schöberl from the Institute of Analysis and Scientific Computing at TU Wien. In particular, I would like to thank Michael Neunteufel and Lukas Kogler who always replied to my emails within a few hours and answered the many questions I had.

- Only experimental measurements can verify the predictions of theoretical physicists and thus I want to thank all our experimental collaborators for their contributions to our joint publications. Especially, I thank (in alphabetical order) Julian Böhm, Jeroen Bosch, Dorian Bouchet, Hui Cao, Matthieu Davy, Louisiane Devaud, Sylvain Gigan, Ulrich Kuhl, Allard Mosk, Pritam Pai, Bernhard Rauer and Hasan Yılmaz from Nice, Utrecht, Grenoble, Yale, Rennes, Paris and Ankara, respectively.

- My sincere thanks also goes to Hui Cao for inviting and welcoming me for an extended research stay at the Department of Applied Physics at Yale University. Especially, I would also like to thank Hasan Yılmaz for his warm hospitality and many stimulating discussions.

- I am deeply grateful to my long-term colleague Matthias Zens who accompanied me since the beginning of our studies. He was always up for discussions even though we worked on very different topics and listened to my problems, no matter how complex or trivial they were. Apart from his scientific skills, I also greatly value his sense of humor that often made my day and helped me through some difficult times.

- Work will always be much less cumbersome in a warm and amusing office atmosphere and thus I want to sincerely thank my long-term office colleagues Andre Brandstötter and Michael Horodynski. In particular, I want to express my deepest gratitude to Andre Brandstötter who always had an open ear for my questions and problems, no matter if they were scientific or private in nature. His kind personality together with his sense of humor and his willingness to help me whenever I was stuck were the foundation of a very pleasant and constructive working atmosphere.

- I also want to thank all my other colleagues in the working group for countless interesting conversations that enriched long office hours. I would especially like to thank my long-term colleague Kevin Pichler for also being a great experimental physicist. Moreover, his talent for keeping me from work will be unforgotten. I'm also grateful for many interesting conversations and stimulating discussions with Lukas Rachbauer, who also thoroughly tested my code and reported many small unrecognized bugs.

- I would like to thank my project, bachelor and diploma students (in alphabetical order) David Fürlinger, David Globosits, Michael Horodynski, Jakob Hüpfl, Markus Kaczvinszki, Jakob Melchard and Thomas Ranner whose supervision was very rewarding and whose efforts led to many new and exciting results.

- Complex wave scattering is a very complex topic and thus I would like to thank my former colleague Philipp Ambichl for introducing me to many of the underlying physical concepts. Furthermore, I also want to thank my former colleague Matthias Liertzer for introducing me to NGSolve which laid the groundwork for the developed code, parts of which are presented in this thesis.

- Administrative tasks can take lots of time, but these were always taken care of by our kind secretaries Heike Höller, Sylvia Riedler and Ingrid Unger which I would like to thank for their professional support.

Last but not least, I want to thank my entire family, all my friends and my girlfriend for their encouragement and motivation. I especially owe my deepest gratitude to my parents for their unwavering support and belief in me.

List of Publications

1. P. Ambichl, A. Brandstötter, J. Böhm, M. Kühmayer, U. Kuhl und S. Rotter, “Focusing inside Disordered Media with the Generalized Wigner-Smith Operator”, *Phys. Rev. Lett.* **119**, 033903 (2017).

2. K. Pichler, M. Kühmayer, J. Böhm, A. Brandstötter, P. Ambichl, U. Kuhl, and S. Rotter, “Random anti-lasing through coherent perfect absorption in a disordered medium”, *Nature* **567**, 351 (2019).

3. M. Horodynski, M. Kühmayer, A. Brandstötter, K. Pichler, Y. V. Fyodorov, U. Kuhl, and S. Rotter, “Optimal wave fields for micro-manipulation in complex scattering environments”, *Nature Photonics* **14**, 149 (2020).

4. P. Pai, J. Bosch, M. Kühmayer, S. Rotter, and A. P. Mosk, “Scattering invariant modes of light in complex media”, *Nature Photonics* **15**, 431 (2021).

5. M. Davy, M. Kühmayer, S. Gigan, and S. Rotter, “Mean path length invariance in wave-scattering beyond the diffusive regime”, *Communications Physics* **4**, 85 (2021).

6. H. Yılmaz, M. Kühmayer, C. W. Hsu, S. Rotter, and H. Cao, “Customizing the Angular Memory Effect for Scattering Media”, *Phys. Rev. X* **11**, 031010 (2021).

7. L. Devaud, B. Rauer, J. Melchard, M. Kühmayer, S. Rotter, and S. Gigan, “Speckle Engineering through Singular Value Decomposition of the Transmission Matrix”, *Phys. Rev. Lett.* **127**, 093903 (2021).

8. M. Horodynski, D. Bouchet, M. Kühmayer, S. Rotter, “Invariance Property of the Fisher Information in Scattering Media”, *Phys. Rev. Lett.* **127**, 233201 (2021).

9. M. Kaczvinszki, N. Bachelard, J. Hüpfl, M. Horodynski, M. Kühmayer, and S. Rotter, “Optimal cooling of multiple levitated particles through far-field wavefront-shaping”, *arXiv*:2103.12592 [physics.optics] (2021), submitted for joint-publication in *Phys. Rev. Lett.* and *Phys. Rev. A*.

10. M. Horodynski, M. Kühmayer, Clément Ferise, S. Rotter, M. Davy, "Customized anti-reflection structure for perfect transmission through complex media", under review at *Nature*.

11. L. Devaud, B. Rauer, M. Kühmayer, J. Melchard, S. Rotter, S. Gigan, "Temporal light control with the time-gated transmission matrix", in preparation.

12. M. Kühmayer, J. Melchard, S. Rotter, "Mean Absorption Invariance of Wave Scattering through Disordered Media", in preparation.

Curriculum vitae

Personal data

Name: Dipl.-Ing. Matthias Kühmayer
Address: Klein-Mariazell 78, 2571 Altenmarkt
Date of birth: 29.06.1988
Place of birth: Mödling, Austria
Nationality: Austrian
Mobile number: +43 676 7136048
E-mail-address: matthias.kuehmayer@gmail.com

Education

since June 2016 **Vienna University of Technology (TU Wien), Institute for Theoretical Physics**
Doctoral studies in Engineering Sciences: Technical Physics
Advisor: Stefan Rotter (Vienna University of Technology)
Web: https://rottergroup.itp.tuwien.ac.at
PhD thesis: Optimal Wave Fields in Complex Scattering Environments

2012 – 2016 **Vienna University of Technology (TU Wien)**
Master of Science (Dipl.-Ing.) in Technical Physics
Graduated with highest distinction (20.04.2016)
Advisor: Stefan Rotter (Vienna University of Technology)
Collaborator: Hui Cao (Yale University)
Diploma thesis: Particle-Like States in D-Shaped Fibers

2008 – 2012 **Vienna University of Technology (TU Wien)**
Bachelor of Science in Technical Physics
Graduated (21.03.2012)
Advisor: Andreas Ipp (Vienna University of Technology)
Bachelor thesis: Induced Photopion Decay

2002 – 2007 **High school, HTBLuVA Mödling**
Higher Department of Electronics and Computer Engineering
Graduated with highest distinction (02.06.2007)

Work experience

since Sept. 2017 **University assistant (Pre-Doc.)**, Institute for Theoretical Physics, TU Wien, Lecturer in the exercise class Quantum Mechanics II

May – June 2019 **Guest researcher**, Hui Cao Research Laboratory, Department of Applied Physics, Yale University, Connecticut, USA

2016 – 2017	**Project assistant (FWF, project SFB NextLite)**, Institute for Theoretical Physics, TU Wien
2012 – 2014	**Teaching assistant**, Institute for Theoretical Physics, TU Wien, Tutor in Electrodynamics I, Quantum Mechanics I & II, Statistical Physics I
Oct. 2007 – June 2008	**Community service** as paramedic, Red Cross, Berndorf
August 2007	**Summer job**, Wasserleitungsverband, Bad Vöslau
July 2005, July 2006	**Summer job**, Wasserleitungsverband, Berndorf
July 2004	**Summer job**, Starlinger, Weissenbach an der Triesting
July 2003	**Summer job**, Wasserleitungsverband, Bad Vöslau

Awards and additional information

Journal cover image of *Nature Photonics* (June 2021, Vol. 15, No. 6) on “Scattering invariant modes of light in complex media”

Homepage header image of *Nature Photonics* (March 2020) on “Optimal wave fields for micromanipulation in complex scattering environments”

Award of excellence of the Faculty of Physics of the Vienna University of Technology ("Leistungsstipendium") in the year 2011

Scientific contributions

8 scientific publications in peer-reviewed journals including *Nature*, *Nature Photonics*, *Communication Physics*, *Physical Review X* and *Physical Review Letters* – see List of Publications

4 contributed talks at national and international conferences (USA, Israel, Austria)

Scientific stay at Yale University in Connecticut, USA during the Master (3 weeks) and PhD studies (7 weeks)

Conferences and summer schools

Feb. 17 – 20, 2020	**Conference** on *“Control of Quantum and Classical Waves in Complex Media (CWCM)”*, Ein Gedi, Israel **Contributed talk** on *“Random Anti-Lasing through Coherent Perfect Absorption in a Disordered Medium”*

Aug. 25 – 30, 2019	**Conference** on *“Mathematical and Numerical Aspects of Wave Propagation (WAVES)”*, Vienna, Austria **Contributed talk** on *“Optimal Wave Fields for Micromanipulation in Complex Scattering Environments”*
May 16, 2019	**Seminar**, Hui Cao Research Laboratory, Yale University, Connecticut, USA **Seminar talk** on *“Controlling Waves in Complex Scattering Environments”*
May 5 – 10, 2019	**Conference** on *“Lasers and Electro-Optics (CLEO USA)”*, California, USA **Contributed talks** on *“Implementing Optimal Field Configurations for Micromanipulation”* and *“A Random Anti-Laser Implemented by Coherent Perfect Absorption in a Disordered Medium”*
Sept. 12 – 16, 2016	**Summer school** on *“Complex Quantum Systems (CoQuS)”*, Vienna, Austria

Programming skills

Python: advanced
Matlab: advanced
Fortran: basic knowledge
C/C++: basic knowledge
Mathematica: basic knowledge

NGSolve: advanced
FEniCS: basic knowledge
COMSOL: basic knowledge

Languages

German: native speaker
English: fluent

Interests and abilities

Training as paramedic
Voluntary work: paramedic for the Red Cross Berndorf (2008 – 2009)
Music: guitar (acoustic & electric), band (guitar & vocals), choir (baritone)
Photography: landscapes, architecture, macro, abstract
Sports: running, hiking
Reading: scientific literature